DESIGN AND VALIDATION OF AN AIR CONDITIONING SYSTEM FOR AN INDUSTRIAL SYSTEM

A THESIS SUBMITTED TO
THE GRADUATE SCHOOL OF NATURAL AND APPLIED SCIENCES
OF
MIDDLE EAST TECHNICAL UNIVERSITY

BY

BERKAY FİLİZ

IN PARTIAL FULFILLMENT OF THE REQUIREMENTS
FOR
THE DEGREE OF MASTER OF SCIENCE
IN
MECHANICAL ENGINEERING

AUGUST 2022

Approval of the thesis:

DESIGN AND VALIDATION OF AN AIR CONDITIONING SYSTEM FOR THE INDUSTRIAL SYSTEM

submitted by **BERKAY FİLİZ** in partial fulfillment of the requirements for the degree of **Master of Science in Mechanical Engineering, Middle East Technical University** by,

Prof. Dr. Halil Kalıpçılar
Dean, Graduate School of **Natural and Applied Sciences** _______________

Prof. Dr. M. A. Sahir Arıkan
Head of the Department, **Mechanical Engineering** _______________

Prof. Dr. Abdullah Ulaş
Supervisor, **Mechanical Engineering, METU** _______________

Assoc. Prof. Dr. Özgür Bayer
Co-Supervisor, **Mechanical Engineering, METU** _______________

Examining Committee Members:

Prof. Dr. Cüneyt Sert
Mechanical Engineering, METU _______________

Prof. Dr. Abdullah Ulaş
Mechanical Engineering, METU _______________

Assoc. Prof. Dr. Özgür Bayer
Mechanical Engineering, METU _______________

Assist. Prof. Dr. Altuğ Özçelikkale
Mechanical Engineering, METU _______________

Assoc. Prof. Dr. Özgür Ekici
Mechanical Engineering, Hacettepe University _______________

Date: 31.08.2018

I hereby declare that all information in this document has been obtained and presented in accordance with academic rules and ethical conduct. I also declare that, as required by these rules and conduct, I have fully cited and referenced all material and results that are not original to this work.

Name Last name : Berkay Filiz

Signature :

ABSTRACT

DESIGN AND VALIDATION OF AN AIR CONDITIONING SYSTEM FOR AN INDUSTRIAL SYSTEM

Filiz, Berkay
Master of Science, Mechanical Engineering
Supervisor: Prof. Dr. Abdullah Ulaş
Co-Supervisor: Assoc. Prof. Dr. Özgür Bayer

August 2022, 148 pages

In this thesis, the air conditioning system for an industrial application was designed. The effect of different supply and return register configurations on the cooling of the multi-purpose box and the air inside was examined. There are some difficulties in transporting products that are sensitive to temperature change and temperature distribution. The main source of these diffuculties is environmental conditions. Especially in regions with hot climatic conditions, products must be cooled while being transported. Within the scope of this study, there is an AC unit designed to operate at maximum performance according to the specified volume and weight limitations, for cooling a multi-purpose box and the air inside. The multi-purpose box is located in a chamber. The circulation of the air between the channels and the chamber is provided by supply and return registers. The position and cross sectional area of these supply and return registers affect cooling time and temperature distribution. In order to plan analyses and evaluate these effects, Design of Experiment (DOE) methods were used. All possible configurations were modelled in Computational Fluid Dynamics (CFD) environment by applying Full Factorial

Design Method. Star CCM+ was used for all CFD analyses. Firstly, CFD analyses of 54 different configurations were completed, and results were evaluated with statistical approach in Minitab Software. Then, one of the best configurations was validated by experimental studies. The effect of the supply register position and area has also been investigated by experimental studies. After that a baffle was placed in the first supply register for the selected configuration to make more homogeneous temperature distribution on the multi-purpose box. To examine the effects of different angles and lengths of the baffle, 9 different configurations were analysed. Validation studies have also been completed for a selected baffle configuration. Finally, regression equations for each response were created according to the CFD results in Minitab software. According to these equations, two responses were optimized. Then, the angle and length of the baffle were found. CFD analysis was repeated according to the specified configuration, and results were evaluated.

Keywords: Computational Fluid Dynamics (CFD), Conjugate Heat Transfer, Optimization, Design of Experiment, Numerical Simulation

ÖZ

ENDÜSTRİYEL SİSTEM İÇİN KLİMA SİSTEMİ DİZAYNI VE DOĞRULAMASI

Filiz, Berkay
Yüksek Lisans, Makina Mühendisliği
Tez Yöneticisi: Prof. Dr. Abdullah Ulaş
Ortak Tez Yöneticisi: Doç. Dr. Özgür Bayer

Ağustos 2022, 148 sayfa

Bu tezde endüstriyel bir sistem için iklimlendirme sistemi tasarlanmıştır. Farklı konfigürasyonlara sahip besleme ve dönüş menfezlerinin endüstriyel sistemin soğutulması üzerindeki etkisi incelenmiştir. Sıcaklık değişimlerine ve sıcaklık dağılımına karşı hassas olan ürünlerin taşınmasında bazı zorluklar vardır. Bu zorlukların temel sebebi ise çevresel şartlardır. Özellikle sıcak iklim koşullarına sahip bölgelerdeki ürünlerin iklimlendirilmesi veya soğutulması gerekmektedir. Bu çalışma kapsamında çok amaçlı bir kutu ve içerisindeki havayı soğutabilmek için, belirtilen hacim ve ağırlık sınırlamalarına göre maksimum performansta çalışması için tasarlanmış bir adet iklimlendirme ünitesi bulunmaktadır. Çok amaçlı kutu ise bir hazne içerisinde bulunmaktadır. İklimlendirme ünitesi ile hazne arasındaki havanın sirkülasyonu besleme ve dönüş menfezleri ile sağlanmaktadır. Bu menfezlerin konumu ve kesit alanı (diğer bir deyişle üfleme ağız açıklığı) sistemin soğutulma süresini ve sıcaklık dağılımını etkilemektedir. Analizleri planlamak ve sonuçları değerlendirmek için “Design of Experiment” (DOE) yöntemleri kullanılmıştır. Tüm olası konfigürasyonlar “Full Factorial Design” yöntemi uygulanarak hesaplamalı akışkanlar dinamiği (HAD) ortamında modellenmiştir. Tüm HAD analizleri için Star CCM+ programı kullanılmıştır. Bu süreçte ilk olarak

54 farklı konfigürasyonun HAD analizleri tamamlanmış ve sonuçlar Minitab yazılımında istatistiksel yaklaşımla değerlendirilmiştir. Ardından en iyi konfigürasyonlardan biri deneysel olarak doğrulanmıştır. Besleme ve dönüş menfezlerinin konumu ve alanlarının sıcaklıklar üzerindeki etkisi de deneysel çalışmalarla ortaya konmuştur. Ardından çok amaçlı kutu üzerinde daha homojen bir sıcaklık dağılımı elde etmek için seçili konfigürasyonun ilk menfezine bir adet yönlendirici yerleştirilmiştir. Yönlendiricinin farklı açı ve uzunluklarının sistem üzerindeki etkilerini incelemek için 9 farklı konfigürasyon analiz edilmiştir. Bu konfigürasyonlar arasından seçilen bir analiz de deneysel çalışmalarla doğrulanmıştır. Son olarak Minitab yazılımı kullanılarak HAD sonuçlarına göre bir regresyon denklemi oluşturulmuştur. Bu denkleme göre iki değerlendirme kriteri optimize edilmiştir. Daha sonra yerleştirilen yönlendiricinin açısı ve uzunluğu optimize edilmiştir. Optimize edilen değerler ile HAD analizi tekrar edilmiş ve sonuçlar değerlendirilmiştir.

Anahtar Kelimeler: Hesaplamalı Akışkanlar Dinamiği (HAD), Eşlenik Isı Transferi, Optimizasyon, Deney Dizayn Teknikleri, Sayısal Benzeşim

To my family…

ACKNOWLEDGMENTS

I would like to express my sincere gratitude to my supervisor Prof. Dr. Abdullah ULAŞ and my co-supervisor Assoc. Prof. Dr. Özgür BAYER for their guidance, advice and recommendations throughout this thesis.

I would also like to thank my friends Dünya Berrak KUTLUTÜRK and Çetin AKÇAY for encouraging me all the time.

Special thanks to my colleagues for their understanding during this study.

A special thank you to my dear, Didem GEZGEN who has always supported and stood by me in this time period.

Finally, I would like to express my deepest love to my parents Nurhan and Gürsel FİLİZ, my siblings Neriman Anıl and İsmail EĞİLMEZ and my nephew Uzay EĞİLMEZ for their endless support and understanding. Their presence always gives me strength.

TABLE OF CONTENTS

LIST OF TABLES

TABLES

LIST OF FIGURES

FIGURES

LIST OF ABBREVIATIONS

ABBREVIATIONS

AC	:	Air Conditioning
CFD	:	Computational Fluid Dynamics
DOE	:	Design of Experiment
“M”	:	Mono
“D”	:	Dual
“T”	:	Triplum
VR	:	Volume Ratio

LIST OF SYMBOLS

SYMBOLS

A	:	Surface area of the control volume
a_f	:	Surface area vector of face f
b_0	:	Constant
b_k	:	Coefficients
D	:	Strain rate tensor
da	:	Surface vector
d_i	:	Individual desirability for ith response
E	:	Total energy per unit mass
$\bar{E}$	:	Mean total energy per unit mass
f_b	:	Body forces per unit volume acting on the control volume
h	:	Heat transfer coefficient
I	:	Identity tensor
J^{ϕ}	:	Convective or diffusive flux of the fluid property ϕ
k	:	Thermal conductivity
L_i	:	Lowest acceptable value for ith response
n	:	Number of data points, or predicted points
P_D	:	Dynamic Pressure
P_S	:	Static Pressure
P_T	:	Total Pressure

$\bar{p}$	:	Mean pressure
q	:	Heat Flux
$\bar{q}$	:	Mean heat flux
$\dot{q}''$	:	Local heat flux vector
r_i	:	Weight of desirability function ith response
S	:	Source term
S_E	:	Energy source per unite volume
S_ϕ	:	Source term
$\vec{s}$	:	The displacement vector from cell centroid to face centroid
T	:	Temperature
$\bar{T}$	:	Mean viscous stress tensor
T_i	:	Target value of ith response
T_s	:	Surface temperature
T_{ref}	:	Temperature of the fluid moving over the surface
U_i	:	Highest acceptable value for ith response
$\vec{V}$	:	Velocity vector
$\bar{v}$	:	Mean velocity
x_k	:	Fit values
y_i	:	Observed data
$\hat{y}_i$	:	Predicted value
$\bar{y}_i$	:	Mean response
μ	:	Dynamic viscosity

ρ	:	Density, the mass per unit volume
ϕ	:	Transport of the scalar quantitiy
σ	:	Stress tensor
Γ	:	Diffusion coefficient
Σ_f	:	Summation over all cell faces of the cell
ϕ	:	Cell centered value

CHAPTER 1

INTRODUCTION

With the development of technology and the needs of the modern world, almost all consumable goods for human such as foods, medicines and technological devices are getting more and more accessible nearly for all regions on the world. However, variable climatic conditions result in some difficulties while these goods are transported. Especially, many different problems are encountered when temperature sensitive products are transported to remote areas. So that, it is very important to consider reducing these compulsory climatic conditions such as high temperature, low temperature, humidity requirements, etc, for transportation of the products. The source of the problems that need to be solved on the subject can generally be listed as follows.

- Conditioning of a product to reach target temperature range, in a certain time
- Sensitivity of the products to temperature gradients
- Variable climatic conditions
- Difficulty of integration of air conditioning systems on mobile platforms due to volume and weight constraints

For the cooling process, a mechanical vapour compression refrigeration system that is integrated on the mobile platform, was used. This type of refrigeration systems is widely used for commercial and industrial applications [1]. From a general point of view and engineering perspective, the requirements of an ideal cooling system are listed as follows [2]:

- Efficient by converting input power to cooling capacity
- Capable of relatively large cooling loads per unit area
- Compact design due to volume and mass constraints

- Environmentally safe and not toxic
- Composed of as few moving parts as possible for maintenance and repair
- Inexpensive

A cooling process, or refrigeration, can be described as removing heat from an enclosed space or a product, and rejecting it to elsewhere to lower the temperature, or maintain a low temperature. These thermodynamic systems operate in a cycle called refrigeration cycle, and schematically shown in Figure 1-1.

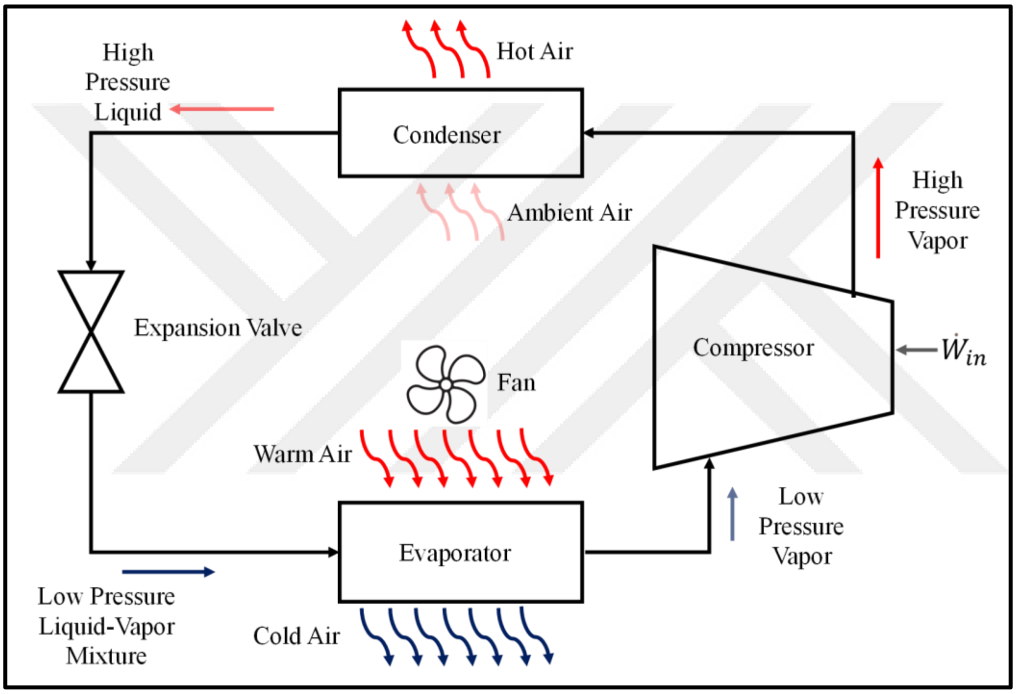

Figure 1-1. Basic Vapour Compression Refrigeration Cycle

1.1 Problem Statement

The air conditioning system, within the scope of this thesis, consists of a multi-purpose box with an outer chamber, an inlet channel, an outlet channel, supply registers, return registers, ducting and an AC unit. This system, together with a mobile platform, a superstructure and energy sources, which are not within the scope of the thesis, constitute the industrial system. A representative image for the air conditioning system is shown in Figure 1-2. Supply registers and return registers will be located between the channels and the chamber. Their positions and areas (cross sectional blowing areas) will be determined by the studies carried out within the scope of this thesis. Ducting design is out of the scope, and the configuration of the AC will be done. More detailed images about the system are given in Chapter 4 and Chapter 5.

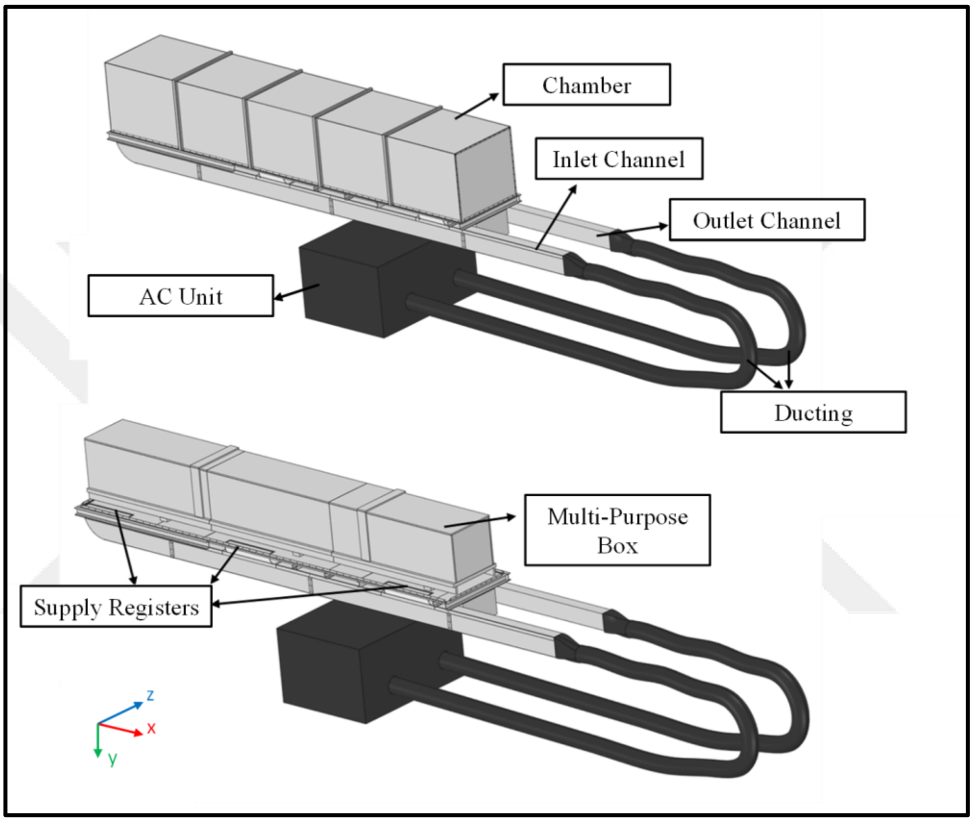

Figure 1-2. The representative image of the air conditioning system

Within the scope of this thesis, it is aimed to cool an enclosed space inside the multi-purpose box in the chamber from the initial temperature (25˚C) to the target temperature (15˚C) in a certain time (4 hours) to have high durability in the transportation of the foods and medicines. In addition, the temperature of the multi-purpose box should be decreased to the target temperature.

It is generally desired that temperature distribution of a product or region should be as homogeneous as possible during the cooling processes. Homogeneous fluid flow over a surface, or in a region, is directly depends on the boundary conditions of inlet and outlet. Some examples to explain importance of the homogeneous fluid flow in the industry are that some products work efficiently only at certain temperatures, to avoid the deterioration of the metal parts due to thermal stress, to prevent food from spoiling during transportation etc. For these reasons, cooling the multi-purpose box and the air inside as homogeneously as possible is among the studies carried out within the scope of this thesis.

In this thesis, many different supply and return registers' position and area of the air conditioning system were investigated with CFD studies to bring temperature values of the multi-purpose box and the air inside from initial temperature to the target temperature. The sample size of these registers was determined by 4 factors, and the samples were created in a systematic way. According to the selected one of the best configurations, improvement studies with a baffle were carried out with 2 factors. The effect of factors on the results (responses) and optimization studies were evaluated with statistical studies. The results obtained from the numerical studies were evaluated and validated with experimental studies.

1.2 Thesis Objective and Design Constraints

The objectives of this thesis are listed below.

- The temperature of the air in the multi-purpose box should be decreased from the initial temperature (25ºC) to the target temperature (15ºC) within 4 hours.
- The temperature of the multi-purpose box should be decreased from the initial temperature (25ºC) to the target temperature (15ºC) within 4 hours.
- Temperature distribution of the multi-purpose box should be as homogeneous as possible at the end of 4 hours.

The design constraints are as follows:

- Due to the other sub-systems around the chamber and the mechanical interfaces of it, supply and return registers can only be positioned at the bottom of the chamber.
- The AC unit, integrated on the platform has a limited volume. Dimensions of the limited volume are 0.85 m x 1.2 m and 1.9 m, that are height, width and depth, respectively. Due to the limited volume on the mobile platform, the equipment in the unit have been selected to give the maximum cooling load. As an example, the flow rate, created by the radial fan (with the highest capacity for the specified volume) that can be used in the AC unit is limited to approximately 1500 m^3/hr.
- There are different sub-systems under the chamber on the platform. Since these systems intersect with the area where the return registers located, return registers with 3 outlets (that will be named "Triplum" in the thesis) cannot be positioned. For this reason, a maximum of "Dual" return register position is available for the return register configurations. Detailed information about the configurations is given in Chapter 4.1.

1.3 Methods of Approach

CFD techniques were used in the numerical studies conducted within the scope of the thesis. In this context, the studies were carried out using STAR CCM+ 2020.2.1 software which is full licensed. Governing equations of fluid mechanics were discretized by using finite volume method. Equations were solved with segregated solver, and SIMPLE algorithm was used to solve pressure-velocity coupling problem. To model turbulence effects, k-ε turbulence model was used.

To examine the effects of supply and return registers on temperature values of the multi-purpose box and air inside, 54 different configurations were modelled in CFD environment. After the first results were obtained, baffle optimization studies were carried out at the first supply register of the selected configuration to make improvements. Moreover, experimental studies were conducted to validate the numerical studies.

In the evaluation of numerical results, statistical analysis was used. Minitab (software program for statistical studies) was used for these studies. To manipulate the controllable factors at different levels and make systematic evaluations, CFD models are conducted with DOE methodology. Full Factorial Design method was used as the DOE method, and all possible configurations were studied. The factors, affecting the design, were evaluated with the pareto chart and their effects on the results were shown with main effect graphs. Finally, optimization studies for baffle configurations were carried out on the fit model.

1.4 Thesis Outline

In this thesis, the problem was introduced, and the aim of the study was given in Chapter 1 along with the design constraints. This chapter also summarizes the methods used to solve the problem.

In Chapter 2, studies in the literature related to the problem were explained. The effects of different inlet and outlet configurations, boundary conditions and the methods on the results were presented.

In Chapter 3, the methods used in the numerical analysis were explained in detail. Then, DOE method used in the statistical evaluation of the results, and the method of optimization studies were mentioned. Finally, the experimental methodology was presented.

In Chapter 4, one of the 54 different configurations that were modelled in CFD environment, was chosen to carry out mesh and time step independence analysis. Then, the CFD models were run, and the results were evaluated. The effect of the factors on the results was also presented with statistical approach.

In Chapter 5, the experimental setup, and the configurations to be tested were presented. CFD results have been validated by experimental results. Moreover, effect of the supply register position and area on temperature values of the multi-purpose box and air inside were presented with experimental results.

In Chapter 6, a baffle was positioned for the specified configuration. The effect of different angles and lengths of the baffle on the temperature values of the multi-purpose box and air inside was investigated with CFD analyses. The randomly selected configuration was validated with experimental results. Finally, the location of the baffle was optimized with specified conditions. Flowchart of the thesis is given in Figure 1-3.

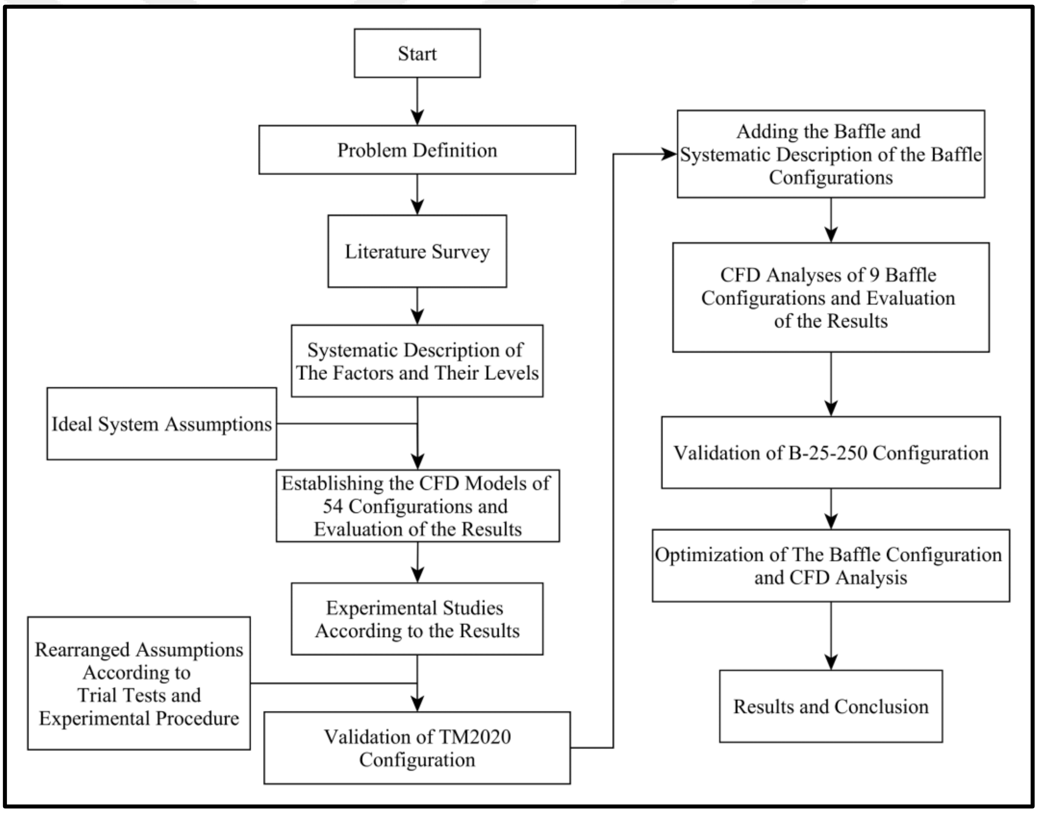

Figure 1-3. Flowchart of the thesis

CHAPTER 2

LITERATURE REVIEW

2.1 Introduction

In this chapter, literature research was conducted about the topic. The methods and results used in these studies were explained. The effect of different inlet/outlet boundary conditions on the temperature distribution and airflow pattern for the systems were also investigated. At the end of this chapter, general results are evaluated. Moreover, achievements of the studies are explained.

2.2 Literature Survey

2.2.1 Applications for Space Ventilation

A CFD simulation model for a ventilated space that is generally carried out under the guidance of ASHRAE standards [3], was established by Gebremedhin and Wu (2004). In their study, flow field for the space, that contains randomly placed twenty virtual cows, was characterized under four different inlet and outlet conditions. In the model, k-ε turbulence model was used. In the study, results were presented in two ways. The first one was in qualitative form, presented in streamline plots, and visually show the air distribution in the space with obstacles. The second one was in the quantitative form, presented in velocity contours. After that, skin temperature and sensible heat fluxes were investigated on randomly selected 3 cows with two different ambient temperature, but with the same relative humidity. Results show that inlet and outlet configurations provided significant variation in air distribution for the ventilated space. Especially cases with two inlet and two outlets (case 3) and one inlet and two outlet (case 4) configurations, shown in Figure 2-1, provided more uniform air flow as with heat transfer [4].

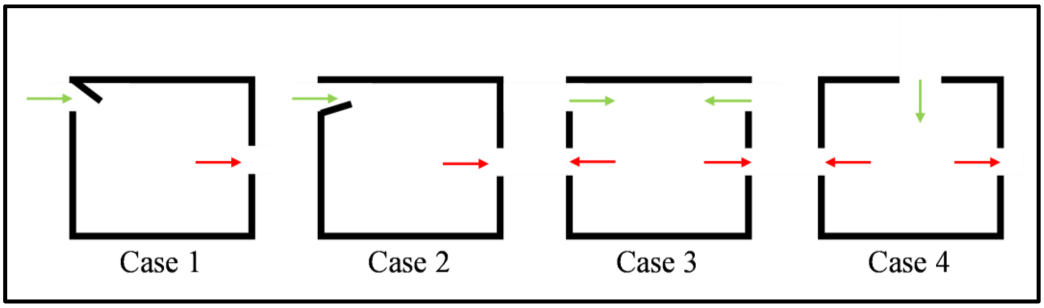

Figure 2-1. Four different inlet and outlet configuration, adapted from [4]

Maher et al. studied the effect of location and openings of windows for a ventilation room building. Air flow pattern and temperature distribution with respect to different conditions were examined numerically with the help of a commercial CFD code. To examine these effects mentioned above, four different configurations were constructed in the programme. These configurations are shown in Figure 2-2. The computational results showed that location of the inlet and outlet openings affects the results. According to the study, results of case (d) represent the worst scenario, while case (c) shows the best temperature distribution according to ASHRE standards [5].

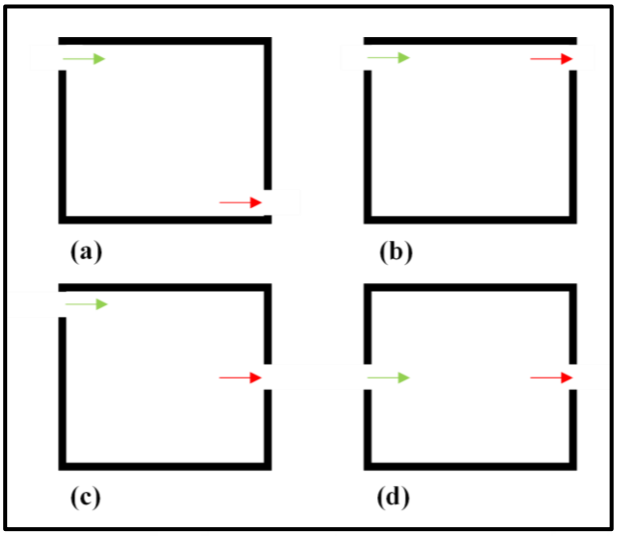

Figure 2-2. Cases constructed for numerical simulations, adapted from [5]

Lim and Kim (2014) analysed the air flow characteristics in a plant factory with different inlet and outlet locations. In the study, CFD methods were used, and k-ε turbulence model was applied. In this study, five different inlet and outlet locations were simulated as shown in Figure 2-3 and Figure 2-4. Simulations were run for an enclosed volume with multilayer cultivation shelves. Results were presented with velocity contours, and quantitative results were taken from the specified shelves. Experimental and simulation results were compared. According to Lim and Kim, for the cases where inlets are located at the side walls, average air current speed in the plant factory is increased, but uniformity is lowered. However, for the cases where inlets are on the ceiling, the average air current speed is lowered, but uniformity is increased. Based on the study, these result show that airflow pattern in the plant factory, or in an enclosed volume, is significantly affected by the locations of the inlet and outlet locations [6].

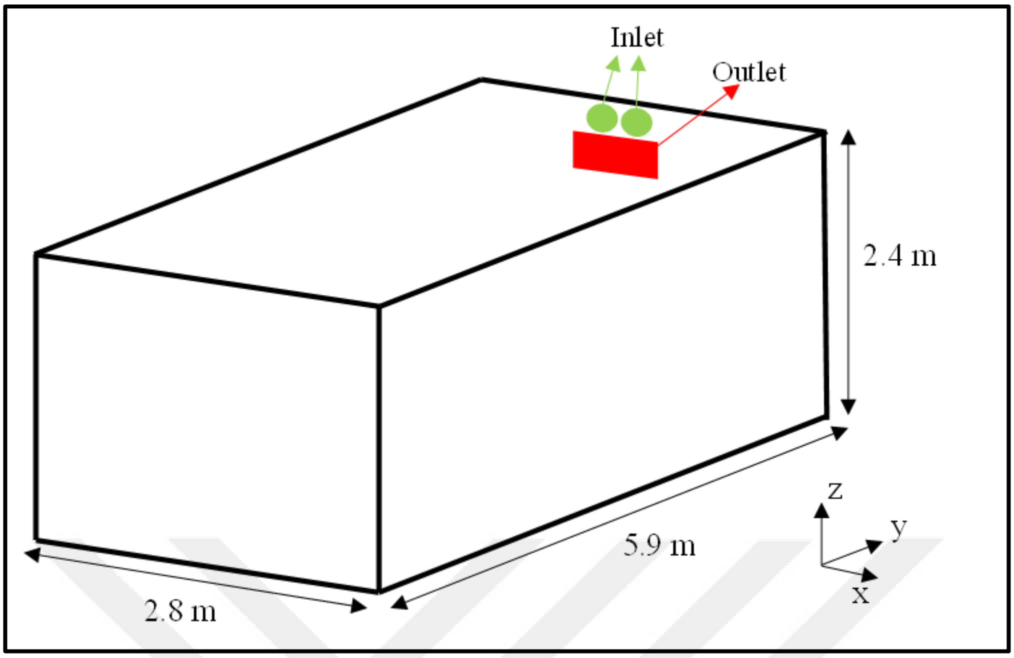

Figure 2-3. Computational domain of the case 1, adapted from [6]

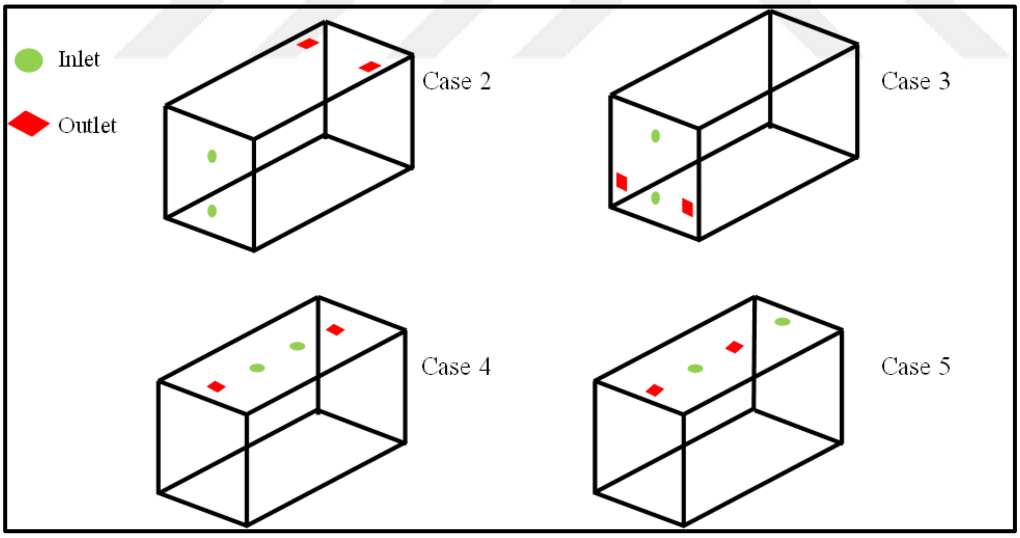

Figure 2-4. Other 4 different cases with different inlet and outlet configurations, adapted from [6]

The position of the blower was investigated in 4 different sections in another study to ventilate an office in the most efficient way. Velocity distribution and temperature over various planes in the office for different locations of the air conditioner blower were analysed and compared with each other. In addition, two different turbulence models, Reynolds stress model and k-ε model, were compared with each other. It is found that k-ε model takes less time, if the grid independency is achieved, since Reynolds stress model seemed to be grid independent than k-ε model [7].

In another study, single-sided ventilation based natural ventilation parameters, such as top ventilation width, top ventilation height, the location of top ventilation, the number of top ventilations and window types, were optimized using DOE technique. The aim of this study is to minimize the indoor air temperature and to maximize the mass flow out. A commercial CFD tool was used to simulate and predict the airflow motion. The schematic diagram for each experimental case model shown in Figure 2-5 and Figure 2-6, respectively. Numerical results were used in DOE studies that aims finding the percentage contribution of each factor on responses. According to the study, number of ventilations contributes three times more in lowering indoor air temperature than ventilation width and ventilation height parameters. Other parameters, position of top ventilation and windows type are less significant, when they are compared with other factors [8].

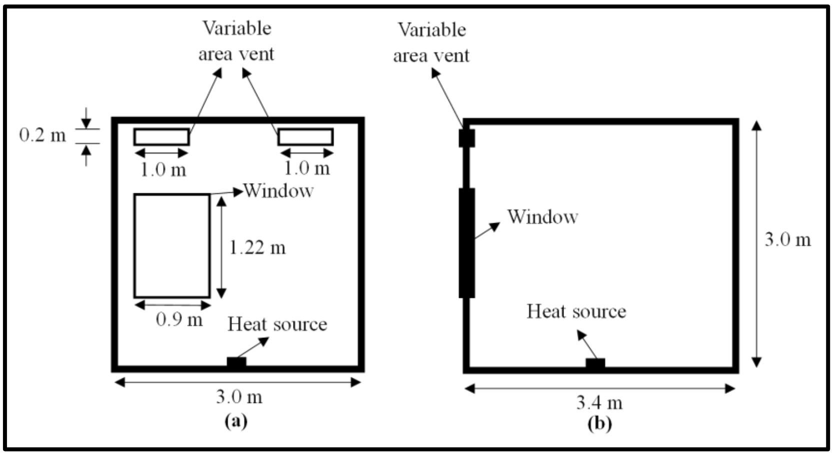

Figure 2-5. Schematic diagram of the experimental setup a) Front view b) Side view, adapted from [8]

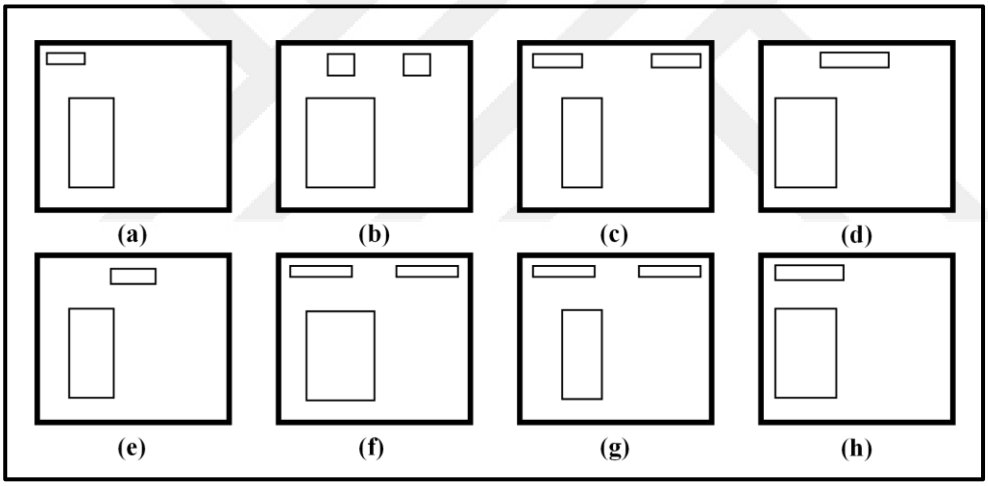

Figure 2-6. Schematic diagram of experiment models. (a) Case 1, (b) Case 2, (c) Case 3, (d) Case 4, (e) Case 5, (f) Case 6, (g) Case 7, (h) Case 8, adapted from [8]

Koufi et al. investigated heat transfer by mixed convection inside ventilated cavities with four different supply and exhaust slots. 2D CFD models were conducted under steady state and turbulent flow regime. Four configurations, rated as A, B, C and D are shown in Figure 2-7. According to the analysis made for the examination of thermal comfort, it was observed that configuration D has much higher efficiency than other configurations with the lowest average temperatures. It was also found that the same configuration provides a higher average Nusselt number than the other configurations through the heat transfer analysis. As a result of that, configuration D was found to be more favourable for evacuating internal heat in the summer [9].

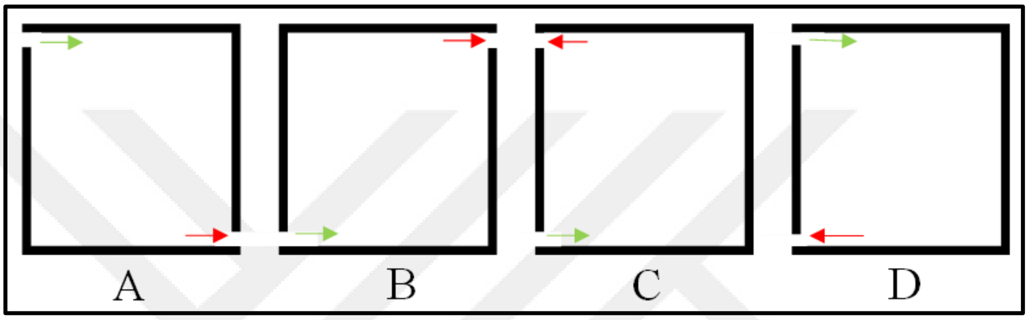

Figure 2-7. Configurations that are modelled in the scope, adapted from [9]

In another paper, a CFD analysis was presented to study the influence of roof inclination angle at the inlet, inlet position, vertical position of the outlet opening and its position on the airflow pattern in a cross ventilated low-rise building. It was shown in the study that air flow rate highly depended on the inclination angle of the inlet and its position. When the roof angle was 45˚, the flow rate was 22% higher than for the reference case at which other parameters were kept constant. Moreover, like other studies, the exit position and opening of the outlet were found to have a small effect (4% and 2% respectively) on the air flow [10].

Another study that analyses the air flow pattern and how it is affected by the distance between supply air diffusers and return air grilles, was made by Khaled et. al (2006). These analyses were constructed by CFD models. The density of the recirculation air was assumed to be constant, since pressure drop, and velocities were low in the domain. To model turbulence effects, k- ε turbulence model was used. The inlet and the outlet were placed at the center of ceiling of an empty place (representing a small office space) without any obstacles. These inlets and outlets were placed 12, 24, 36, 48 and 60 inches away from each other, and each configuration were modelled with three different flow rates 200, 350 and 500 cfm. According to analysis, when the distance between inlet and the outlet was decreased, the rate of air by-pass was increased. It was also concluded by qualitative and quantitative results that when the flow rate was decreased at the inlets, rate of air by-pass almost decreased. In the study, energy losses due to the rate of air by-pass were also evaluated from an economic point of view [11].

Influence of the width of the inlet on airflow characteristic was studied by Susin et. al. In this study, three different airflow features were investigated by means of three eddy viscosity turbulence models, standard k-ε, RNG K-ε and k-ω. According to the study, the best performance was achieved by standard k-ε model, which provided minimum errors and computation time [12].

Murakami and Kato compared 3D numerical studies with experimental studies by changing the outlet parameters and room dimensions. They assumed fully turbulent airflow in the room and used k-ε turbulence model. According to the study, numerical simulations that are modelled with k- ε turbulence model corresponds well with the experimental results [13].

Another CFD study for ventilating enclosed volume was conducted by Harral and Boon. In the study, airflow was modelled with Reynolds-Averaged Navier-Stokes equations, and k-ε turbulence model was used. Primary and secondary flows were discussed. It was observed that CFD model predictions perfectly matched with experimental results [14].

Bjerg (2002) modelled different air inlets for ventilated animal houses with different inlet positions and areas. In the study, five different configurations were set up in a CFD software, and velocity results were investigated along the room length. In the study, measurement devices were also tested. To calculate approximate velocity values, another 2D dimensional work was discussed [15].

Another area where different inlet and outlet positions of the flow are examined for ventilated spaces in terms of airflow pattern and thermal comfort within the system, is the building design processes. The distribution of indoor air may be uncomfortable considering thermal comfort issues, because of its volume flow rate and temperature, and it does not matter whether the AC unit, (or ventilation system) is working efficiently, or not. In the study conducted in 2020, it was aimed to improve indoor air quality in an office. Four different CFD models that have different inlet and outlet configurations were constructed. According to the configurations shown in Figure 2-8, better airflow pattern and temperature distribution were achieved when the location of the inlet is on a side and outlet is on another side of the office (case 2 and case 3). In this way short-circuit of the air is avoided [16].

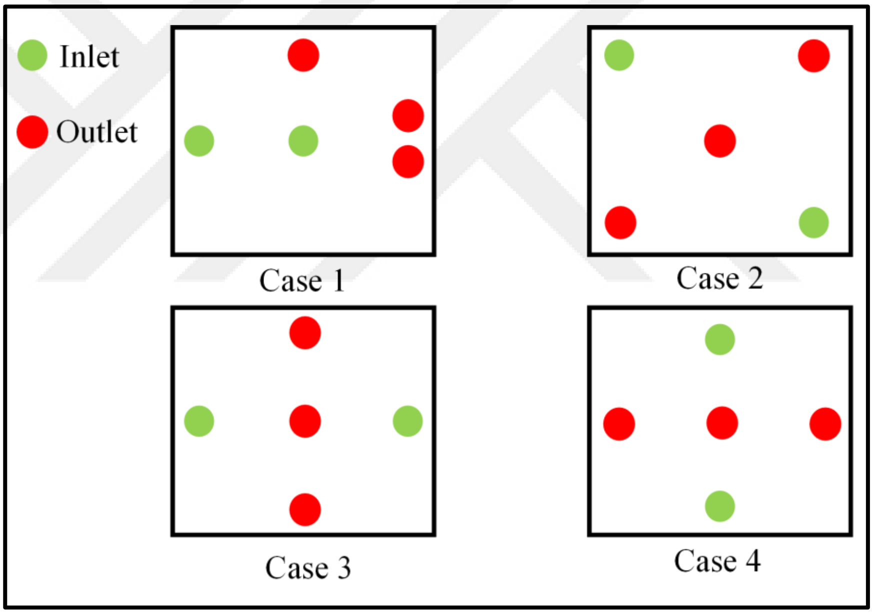

Figure 2-8. Locations of the inlet and outlet for each case study, adapted from [16]

Similar to mentioned studies, detailed evaluation of the impact of the inlet and outlet openings on cross ventilated buildings were presented by H. Montazeri and F. Montazeri (2017). 3D isothermal CFD simulations with RANS equations and the realizable k-ε turbulence model were performed to characterize airflow in the building for 23 different inlet and outlet configurations. As a result of the study, the size of the window at the inlet significantly affected the airflow rate into the building. By increasing the size of the outlet window, while the area of the inlet window was constant, the induced airflow rate increased monotonically. However, this increase was pronounced for situations until the outlet area became equal to inlet area. Therefore, increasing the outlet window size larger than the inlet windows size is not a beneficial way to increase induced airflow rate in the cross ventilated buildings. It was also shown that, when the windows' outlet size was larger than the inlet size, the induced airflow was almost insensitive to the type of outlet openings [17].

2.2.2 Applications for Air Quality Improvement

Chen et al. (2019) investigated the effect of aspect ratios of ventilation inlets and their locations on indoor air quality. The aim of this study is to operate the ventilation system in the most efficient way to remove carbon dioxide from the environment. These studies are important to see the effect of inlet and outlet configurations on the airflow patterns in the specified geometries. The physical model is shown in Figure 2-9 and Figure 2-10. Both numerical simulation and experimental works were processed. The air flow pattern was simulated by solving Reynolds Averaged Navier Stokes (RANS) with RNG k-ε turbulence model. Moreover, SIMPLE algorithm was used to solve the pressure-velocity coupling problem. Series of different simulations were carried out with different locations as symmetric and asymmetric, 4 different inlet aspect ratios (2, 4, 6 and 8) and four different flow rates. According to the paper, when the inlet and outlet positions are symmetric and aspect ratio is 4, carbon dioxide concentration in the ventilated room is lower than the other conditions. It is also interpreted that when the effect of aspect ratio (l/w) is 8, and velocity is increased at the inlet, overall indoor carbon dioxide concentration becomes relatively higher [18].

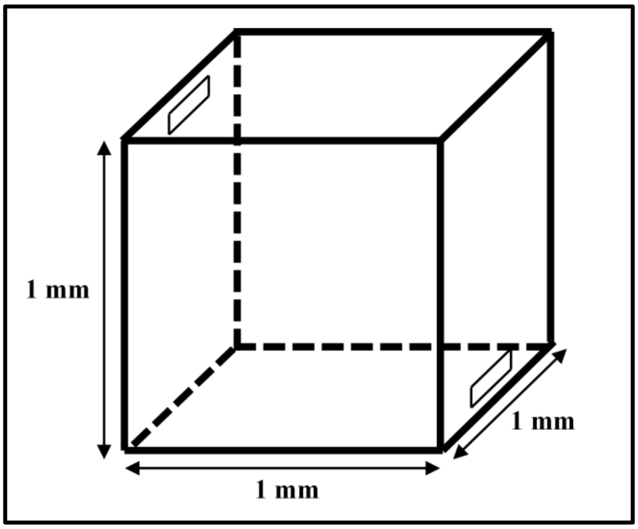

Figure 2-9. Schematic diagram of the modelling domain, adapted from [18]

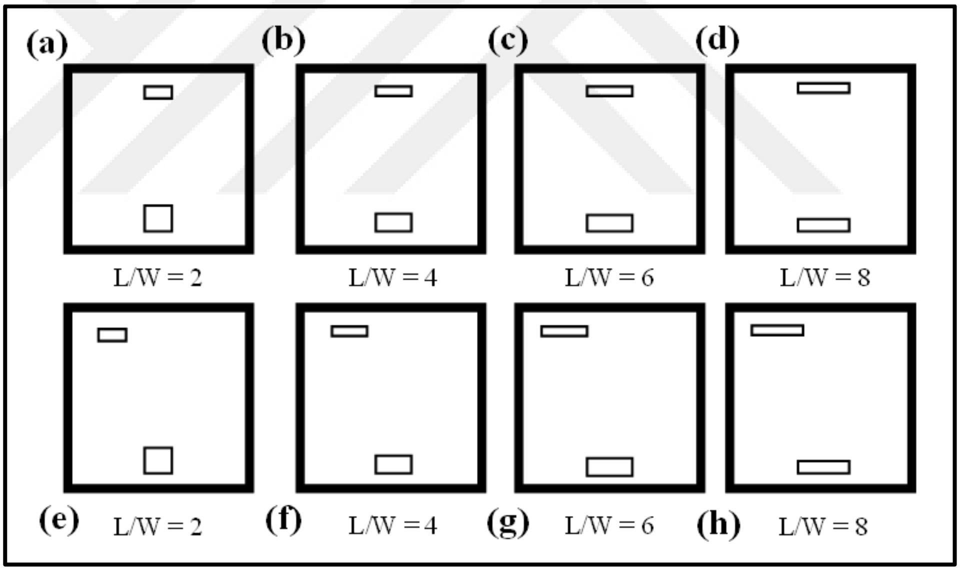

Figure 2-10. Side view of the cases with a top inlet and bottom outlet for simulated cases (L/W is length over width), adapted from [18]

As a similar study with the same purpose, Cao et al. conducted a study in 2018. Unlike the other study, the inlet and outlet positions were at the center of opposite walls in the farthest away from each other and have not been changed during the analyses. The physical model is shown in Figure 2-11. According to the study, under the same flow rate, the smaller inlet area regulated the airflow pattern to remove carbon dioxide more homogenously [19].

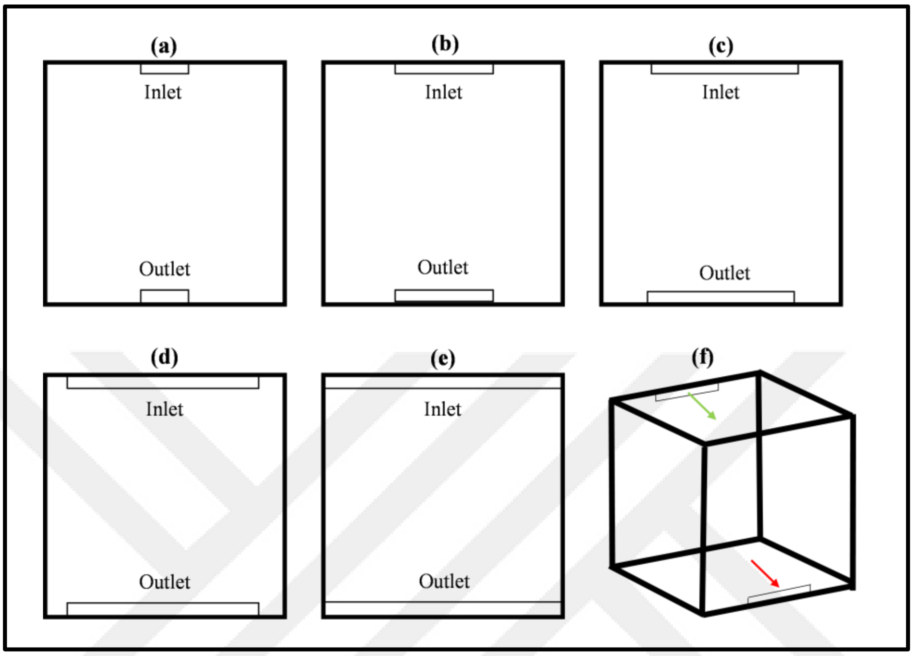

Figure 2-11. Side and isometric view of cases with a top inlet and bottom outlet for simulated cases, adapted from [19]

Distribution of contaminant concentrations that is a function of several factors, in a room (or a ventilated space) was examined by Khan et al. Several inlet and outlet locations were also investigated to determine optimum inlet and outlet positions with CFD analyses. The numerical results were validated with experimental results. It was concluded that outlet locations that is near the ceiling, resulted in lower concentration (better airflow characterization) than the corresponding outlet near the floor, while inlet is located at the side wall. The reason is that when inlet-outlet configuration is set up face to face each other, air bypass is inevitable. It is understood that by increasing the airflow rate in the system, the effect of the outlet position on the airflow pattern becomes negligible [20].

In another article, that aims to reach optimum air quality in the specified region, three different positions were investigated under the different flow rates. Analysis showed that placing inlets and outlets as far as possible resulted in a more homogeneous air flow pattern and energy saving [21].

2.2.3 Other Applications

Another study about heat transfer enhancement in a rectangular channel with different inlet conditions is published by Kurtbaş (2008). In the study, the flow regime is turbulent and ratio of the height of the entry channel to the height of test section (h_c/H) is a variable parameter. He also investigated the effect of 45˚ and 90˚ turned flow for the experimental setup. According to the study, when the height ratio is higher than 1, averaged Nusselt number is higher at the entrance of the test section due to impinging jet, however mean averaged Nusselt number is higher for the case that height ratio is lower than 1 for the entire test setup [22].

Moureh and Flick (2004) used ANSYS FLUENT CFD package to characterize velocities, airflow patterns and temperature levels within a typical loaded vehicle with and without inlet duct system. In this study, Reynold's Stress Model (RSM) was used. Results were compared with 1:3 scaled experimental setup, and temperature distributions in the truck. Numerical and experimental results show that local separation points were accurately predicted by the model. Moreover, using air ducts systems improved the overall homogeneity of the temperature distribution of air in the ventilation duct. Since using air ducts increased velocities from 0.1 m/s to 1 m/s for rear regions, homogeneous air flow was provided, and low temperature gradients were occurred [23].

Data centers, where air-conditioning is performed in very narrow spaces, are another example where CFD analyses are presented. Numerical experiments were conducted to study the effects of perforated tiles opening ratio, air flow rates and locations of supply/return air on the data center performance. According to Nada et al. increasing the opening ratio at a constant flow rate decreases the bypass of the cold air from the cold aisle to the hot aisle. It was also shown that, hot air recirculation at the middle region of the data center is decreased. At high flow rates, air was moved up with a high momentum, and it provided cold air bypass from the cold aisle to the hot aisle. In this study, the distribution and uniformity of air flow pattern was investigated by changing the location of racks, obstacles, cables and CRAC (Computer Room Air Conditioning) units [24].

Another study to investigate effect of different inlet conditions on cooling was conducted by Roh et al. Although the study was about the air quenching equipment, it showed that inlet configurations significantly affected cooling processes. In the study, 4 different inlet conditions were established in a CFD software. The results indicated that the cooling effect of the inlet designs were different from that of the reference model. Furthermore, two important points can be interpreted from the paper. The first one is that cooling effect is directly depends on the distance between inlet positions and cooled products. When the inlets are close to the conveyor, cooling effects are increased. The second one is that the cooling rate is higher when the air inlet is smaller, and so the velocity of fluid is higher at inlet conditions. It is noted in the study that these conditions can be varied with respect to model's geometry [25].

Assari et. al. worked on the influence of varying inlet and outlet locations of the water for a horizontal cylindrical tank. They changed inlet positions while outlet positions and the area of the inlets were constant, and vice versa. Their study showed that the position for hot water coming from the highest position and cold-water outflow from the lower position is ideal for temperature distribution for the horizontal cylindrical tank. In other words, for a fluid, it is better to obtain homogenous waterflow and temperature distribution when inlet and outlets are located far away from each other. In this study, numerical results were also compared with experimental results [26].

2.3 Assessment of the Literature Survey

The effects of different inlet and outlet configurations on the airflow pattern have been evaluated in the literature. It has been observed that different configurations have significant effects on airflow pattern and consequently heat transfer phenomenon. In the literature, results are generally presented in qualitative and quantitative forms. In the conclusion part of many journals, it was mentioned that more configurations should be evaluated, and the results should be more comprehensive.

The method used in the evaluation of different configurations in this thesis includes many methods used in the literature. Unlike other studies, not only CFD results but also statistical results were evaluated in this thesis. Full Factorial Design Method was used as the DOE method. In other words, almost all configurations for the air conditioning system have been analysed in CFD environment. Thus, the main and interaction effects of the factors on the results were presented in detail. In addition, the configurations, selected from the analyses, were validated with the experimental studies, and an optimization study was carried out after these validations.

CHAPTER 3

METHODOLOGY

3.1 Numerical Methodology

3.1.1 Introduction

Although CFD modeling may not represent the physical experiments completely, it can reduce the amount of experimental work, significantly. In this chapter, the governing equations and solution methods for CFD models, used in the scope of this thesis, are provided. Moreover, information about the Star CCM+ software is given.

3.1.2 Method of Numerical Solutions

Fundamental laws such as conservation of mass, conservation of linear momentum and conservation of energy are used in order to derive governing differential equations for fluid mechanics which are solved in CFD studies [27].

The conservation of mass through a control volume is expressed with the continuity equation 3.1:

$$\frac{\partial \rho}{\partial t} + \nabla \cdot \left(\rho \vec{V}\right) = 0 \tag{3.1}$$

Equation of conservation of linear momentum is written as:

$$\frac{\partial \left(\rho \vec{V}\right)}{\partial t} + \nabla \cdot \left(\rho \vec{V} \otimes \vec{V}\right) = \nabla \cdot \sigma + f_b \tag{3.2}$$

where, $\otimes$ denotes the outer product.

Stress tensor is written as the sum of normal stresses and shear stresses for the fluid, and it can be shown as [28]:

$$\sigma = -pI + 2\mu D - \frac{2}{3}\mu I \cdot \nabla \cdot \vec{V} \tag{3.3}$$

The conservation of energy can be written, when the first law of thermodynamics is applied to the control volume, as:

$$\frac{\partial(\rho E)}{\partial t} + \nabla \cdot (\rho E \vec{V}) = f_b . \vec{V} + \nabla \cdot (\vec{V} \cdot \sigma) - \nabla \cdot q + S_E \tag{3.4}$$

In this study, density of the recirculation air is assumed as constant. For incompressible flows equation 3.1 simplifies to as follows:

$$\nabla \cdot \vec{V} = 0 \tag{3.5}$$

For incompressible flows the last term on the right hand side of the equation 3.3, the last term of viscous stress tensor, is zero due to incompressibility constraint [28]. With simplifications and constant viscosity assumption, equation 3.2 can be written as:

$$\frac{\partial \vec{V}}{\partial t} + (\vec{V} \cdot \nabla)\vec{V} = -\frac{1}{\rho}\nabla p + v\nabla^2 \vec{V} + \vec{f} \tag{3.6}$$

where, v is the kinematic viscosity.

Equation 3.4 can be simplified by using the definition of enthalpy and fundamental equations of thermodynamics as follows:

$$\rho c_p \left[\frac{\partial T}{\partial t} + (\vec{V} \cdot \nabla)T\right] = k\nabla^2 T + S \tag{3.7}$$

Numerical methods that includes finite volume method, generally transform the mathematical models into a system of algebraic equations. This transformation is done by discretizing the governing equations in space and time.

When the proper constitutive relations are adopted into the conservation equations, closed set of equations are obtained [29]. A generic transport equation can be fit for all conservation equations. When the generic transport equation is integrated over a finite control volume V and Gauss's divergence theorem is applied, the following integral form of the transport equation can be obtained:

$$\underbrace{\frac{d}{dt}\int_V \rho\phi\, dV}_{\boxed{\text{Transient Term}}} + \underbrace{\int_A \rho\vec{V}\phi\cdot d\mathrm{a}}_{\boxed{\text{Convective Flux}}} = \underbrace{\int_A \Gamma\nabla\phi d\mathrm{a}}_{\boxed{\text{Diffusive Flux}}} + \underbrace{\int_V S_\phi\, dV}_{\boxed{\text{Source Term}}} \tag{3.8}$$

ϕ is a scalar quantitiy. By setting the ϕ, for example, as *u, v, w,* that are velocity components of a 3 dimensional space, or *E*, and selecting the appropriate values for the diffusion coefficient Γ and source terms, integral forms of partial differential equations for mass, momentum and energy conservations can be obtained.

Equation 3.8 has four distinct terms, and they can be explained, respectively, such as:

- Transient Term : Time rate of change of fluid property ϕ inside the control volume.
- Convective Flux : The net rate of decrease of fluid property ϕ across the finite control volume boundaries due to convection.

- Diffusive Flux : The net rate of increase of fluid property ϕ across the control volume boundaries due to diffusion.
- Source Term : Generation or destruction of fluid property ϕ inside the control volume

In equation 3.8, there are two types of integrals, surface integrals and volume integrals.

STAR CCM+ uses second-order midpoint rule to discretise surface integrals. To do that, integrals are evaluated as the product of the value at the center of the cell face and cell face area.

$$\int_A J^{\phi} \cdot d\mathrm{a} \approx \Sigma_f (J_f^{\phi} \cdot \mathrm{a}_f) \tag{3.9}$$

In Star-CCM+, values of the scalar fluid properties are stored at the cell centers, while applying finite volume method. However, the values at the center of the cell face are not known, and they are approximated by interpolation in terms of the values at the cell centers. To accomplish this, second order upwind scheme was used. Interpolation scheme for the convection flux term can be written as:

$$\rho\phi(\vec{V}.\mathrm{a}) = (\dot{m}\phi)_f \tag{3.10}$$

where, $\dot{m}_f$ is the mass flow rate at the cell face. According to the second order upwind scheme, face values ϕ_f are computed using the following expression [32]:

$$\phi_f = \phi + \vec{s} \cdot (\nabla\phi) \tag{3.11}$$

where $\nabla\phi$ is gradient of cell centered value [32].

Volume integral manifests itself as a source term in equation 3.8, and it is integrated over the volume of the cell. In the software, volume integral is approximated by the product of the mean value of the source term at the center of the cell and the volume of the cell.

$$\int_V S_\Phi \, dV \approx S_{\Phi 0} V_0 \tag{3.12}$$

After applying the integration approximation, equation 3.8 yields the following semi-discrete transport equation:

$$\frac{d}{dt}(\rho\phi V)_0 + \Sigma_f\left[\rho\phi\left(\vec{V}.\mathrm{a}\right)\right] = \Sigma_f[\Gamma\nabla\phi.\mathrm{a}] + S_{\phi 0}V_0 \tag{3.13}$$

For transient simulations, time is an additional dimension for space. In simulations, the Euler implicit scheme, a first-order temporal scheme was used to discretize transient term such as:

$$\frac{d}{dt}(\rho\phi V)_0 = [(\rho\phi V)_0^{n+1} - (\rho\phi V)_0^{n}]/\Delta t \tag{3.14}$$

The segregated flow solver of the software is used in the numerical studies carried out within the scope of thesis. In this solver, conservation equations are solved in a sequential manner. The non-linear governing equations are solved iteratively for the solution variables such as *u, v, w, p.* With segregated solver, a pressure-velocity coupling algorithm, where the velocity field is determined with mass conservation, is applied by solving a pressure-correction equation. The pressure-correction equation is derived from the continuity equation and the momentum equation, and it is an iterative solution that starts with predicted velocity and pressure values. The method can also be defined as predictor-corrector approach. In this thesis, SIMPLE (Semi implicit method for pressure linked equations) algorithm is used. The working principle of the SIMPLE algorithm can be summarized as follows [28, 29]:

- Start an iteration with predicted pressure $p^\star$
- Solve discretized momentum equations with predicted pressure to get intermediate velocity ($u^\star$, $v^\star$, $w^\star$)
- Solve pressure correction equation to get pressure correction p'
- Update the pressure field such as:

$$p^{\star\star} = p^\star + \omega p' \tag{3.15}$$

where, ω is the under-relaxation factor for pressure.

- Correct velocities with their starred values, and using the velocity correction equations
- Solve discretization equation for temperature and turbulence quantities
- Check the imbalance for convergence
- Either stop or do one more iteration with respect to tolerance

In most of the fluid flow problems, engineers always face with irregularities at fluctuating flow quantities, called turbulence. Turbulence modelling was needed due to the complex shape of the geometry to be examined within the scope of the thesis, and Reynolds numbers, obtained (~7x10^6) in the turbulent flow regime in CFD models. Since they are at small scales and have high frequencies most of the time, resolving them in time and space comes at excessive computational costs. Instead of solving exact governing equations with turbulence effects (Direct Numerical Solution), they are generally solved with averaged flow quantities. One of the most used models in the field to do that is the Reynolds Averaged Navier-Stokes (RANS) turbulence model that is also used in this thesis. In this method, governing equations for fluid mechanics can be written with averaged flow values [28, 29]. To obtain RANS equations, each variable ϕ in the Navier Stokes equations are decomposed into their mean, or averaged value $\bar{\phi}$ and its fluctuating component ϕ'.

$$\phi = \bar{\phi} + \phi' \tag{3.16}$$

RANS equations are identical to the Navier Stokes equations, except that an additional term that appears in the momentum and energy equations. The mean mass, momentum, and energy transport equations can be written as:

$$\frac{\partial \rho}{\partial t} + \nabla \cdot (\rho \bar{v}) = 0 \tag{3.17}$$

$$\frac{\partial (\rho \bar{v})}{\partial t} + \nabla \cdot (\rho \bar{v} \otimes \bar{v}) = -\nabla \cdot \bar{p} I + \nabla \cdot (\bar{T} + T_{RANS}) + f_b \tag{3.18}$$

$$\frac{\partial (\rho \bar{E})}{\partial t} + \nabla \cdot (\rho \bar{E} \bar{v}) = -\nabla \cdot \bar{p} \bar{v} + \nabla \cdot (\bar{T} + T_{RANS}) \bar{v} - \nabla \cdot \bar{q} + f_b \bar{v} \tag{3.19}$$

The additional term, T_{RANS}, consists of mean fluctuating flow quantities and turbulent kinetic energy [30]. To model these terms, one of the Eddy Viscosity Model, k-ε turbulence model was used. The k-ε turbulence model is a two-equation model which solves RANS equations for the turbulent kinetic energy k and turbulent dissipation rate ε to determine the turbulent eddy viscosity. For a number of decades, various number of forms are constructed and used for k-ε turbulence model, and it has become the most widely used model for industrial applications. In this thesis, realizable k-ε turbulence model is used [31]. Walls are a source of vorticity in most flow problems of practical importance. In this thesis, "All y+ Wall Treatment" was applied across the wall boundary layer in STARCCM+ software. It uses blended wall functions that emulate the low y+ wall treatment for fine meshes, and the high y+ wall treatment for coarse mesh. The main advantages of these models can be listed as follows [32]:

- Mesh flexibility which provides good results for coarse meshes
- Suitable for industrial applications

- Good predictions for high dimensionless wall distance (y+)
- The least inaccuracies for $1<y^+<30$

Conduction heat transfer through the walls of the chamber and convection heat transfer between the surfaces and the air flow are taken into account in this thesis, however, radiation effects are excluded.

The law of heat conduction, or Fourier's law, can be written as:

$$\dot{q}'' = -k\nabla T \tag{3.20}$$

Convection is described as being natural, where natural buoyancy forces drive the bulk fluid motion, or forced, where external driving force (as a source of fan, propeller, etc) moves the fluid.

Convection heat transfer at a surface is governed by Newton's law of cooling.

$$\dot{q}_s'' = h\left(T_s - T_{ref}\right) \tag{3.21}$$

In STAR-CCM+ heat transfer can be calculated within the fluid, between different fluids, between the fluid and the solid and within solids. When the coupled heat transfer is modelled and solved in a fluid and an adjoining solid, it is called conjugate heat transfer. For a conjugate heat transfer analysis, the energy equation is solved throughout the fluid and solid domains with created fluid/solid interface.

In the CFD studies conducted within the scope of the thesis, mapped contact interface is applied at the boundaries of the domains. These interfaces are set between recirculation air domain (fluid domain) and the multi-purpose box domain (solid domain), and the multi-purpose box domain (solid domain) and the air inside (fluid domain). Numerical domains solved for the recirculation air, the multi-purpose box and air inside, and mapped contact interfaces are shown in Figure 3-1 and Figure 3-2, respectively.

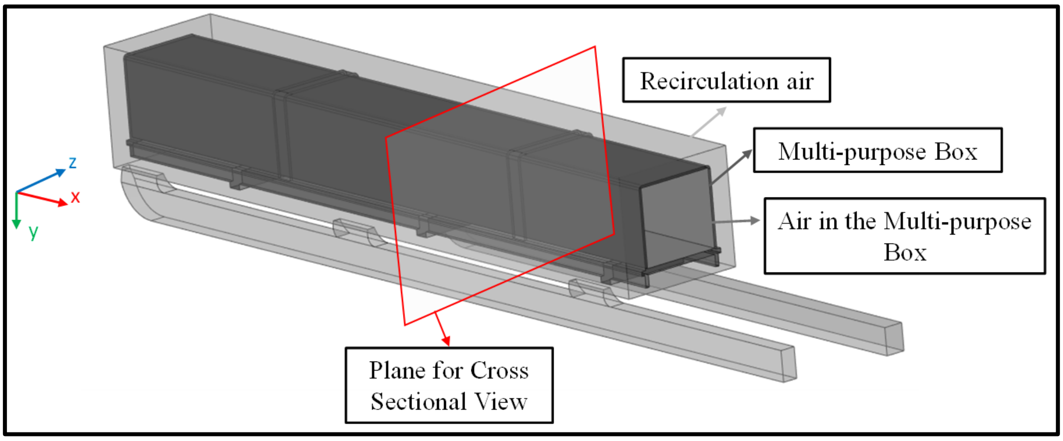

Figure 3-1. Numerical domains

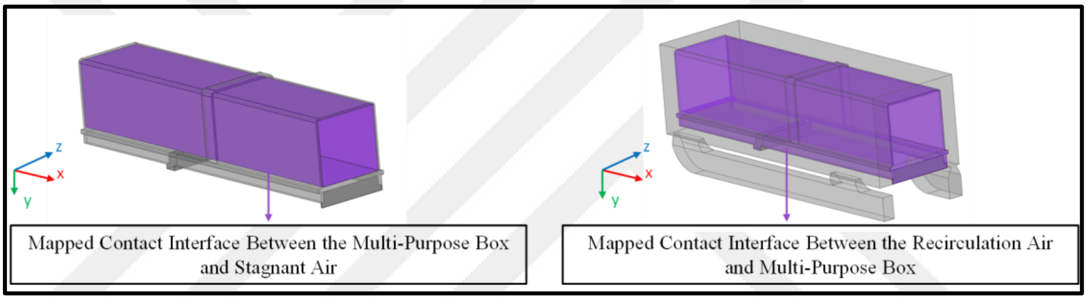

Figure 3-2. Mapped contact interfaces

The mapped contact interface is indirect interface type between a fluid and a solid. It depends on the indirect association between faces of interfacing boundaries between the domains. The main advantage of this type of interface is that it allows non-conformal mesh. It is desirable when domains in cases have different mesh resolutions like in the studies of this thesis. In other words, heat conduction in the multi-purpose box requires coarser mesh, when it is compared to resolving the boundary layer in the fluid domain. In this way, it is possible to conduct CFD model with different cell sizes and the time required for the solution is reduced to the optimum level.

Within the scope of this thesis, in Chapter 6, the air conditioning system has been improved by adding a baffle to the first supply register. To see the effects of the baffle, and to carry out optimization studies, it was modelled in the CFD environment. For this, “the baffle contact” feature of STAR CCM+ software is used. A baffle contact is described as a zero-thickness surface.

3.2 Design of Experiment and Optimization

Basic ideas of the Design of Experiment (DOE) and statistical experimental design was mentioned in the 1920s by Sir Ronald Aylmer Fisher [33]. In his works, he created the foundations for modern statistics. In 1951, Box and Wilson applied the idea to industrial experiments [34]. Although having been controversial, the work of Taguchi, in the 1980s, made statistical experimental design very popular, and he made great contributions to modern statistics [35].

DOE is an efficient and a systematic method which offers engineers and scientists to study the relation between input variables (defined as factors in terminology) and output variables (defined as responses) of the work. To perform a DOE study, the first, it is necessary to acquire a full understanding of the factors and the responses. These factors can be qualitative or quantitative. Some considerations should be avoided in the selection of evaluation criteria (response). These can be listed as follows [36, 37]:

- Attribute responses (such as true/false)
- Values close to each other in terms of their physical orders
- Repeated theoretical maximum and theoretical minimum values

According to the number of experiments that can be afforded, the DOE technique and number of levels are selected. What is meant by the “level” expressed here is the definitions (for qualitative factors), or values (for quantitative) that each factor has.

Experimental design techniques that are applied in early stages of the process development can result in:

- Improving process yields
- Reducing variability and getting close to target requirements
- Reducing development time
- Reducing overall costs

In engineering design activities, it is very important to use experimental design methods, when new products are developed, or existing ones are improved. Some applications of statistical design experiments in engineering design include:

- Comparison and evaluation of basic design configurations
- Examination of material alternatives
- Selection of proper design parameters
- Finding key product design parameters that affect product performance

Thanks to the development of computers and advances in numerical computing, designers frequently use computer models to assist them in carrying out their studies. These examples include finite volume and finite element methods for many aspects of mechanical, thermal and structural designs [36]. DOE applications can be applied to these models just as easily and properly as they can to actual systems. In this way, these applications will result in reduced development time and better designs.

There are many methods in DOE, and they are selected for the purpose. It is important to specify number of experiments with respect to number of factors and levels of each factor to determine DOE method to be used. Some of the DOE designs are summarized as [37]:

<u>Full Factorial Designs:</u> Almost all possible combinations of factors are run in experiments. The sample size is found by product of the number of levels for each factor. Typically, they are used when there are not many factors and levels in DOE. In this method, main and interaction effects of the factors on the response can be presented with high prediction rates. 2^k Full Factorial Design is one of the most used Full Factorial Designs, when all factors have 2 levels.

Fractional Factorial Designs: It is one of the most popular design methods in the industry. The method is used at the initial stages of experiments to narrow important factors that will be used in DOE. These types of designs usually require fewer sample sizes, or experimental runs, than other designs. Plackett-Burman, Cotter and mixed level designs are examples of Fractional Factorial Designs.

Response Surface Designs: This method is used at the latter stages of the experimentations when factors, that affect response, have been identified. It involves small number of continuous factors (generally 2 to 8). The design requires at least 3 levels for each factor to model curvature relationship between factors and response. So that, it is an expensive method unless the number of factors is limited.

Mixture Designs: These kinds of methods are used when the factors are interdependent on each other, in other words, when each component in a mixture is dependent on other component. Factors' values in this method are set between zero and one. The aim of this method can be summarized as optimizing recipe for a mixture with several ingredients.

Split Plot Designs: Typically, Split Plot Design is used when factors in the experiment are hard to change, for example, changing the climate conditions of the test region, changing the material of huge samples, etc. In this method, factors are applied to more than one experimental unit, because they are with batch processing, hard or costly to change.

Taguchi Array Designs: This design method is used to control factors and minimize the effect of noise factors (uncontrollable factors) that are usually difficult or expensive to control. The method is carried out based on Taguchi's inner and outer array approach. Experimental designs are reduced with respect to selection of proper Taguchi Orthogonal Array type.

As it is examined in the scope of this thesis, many experiments involve two or more factors with levels to investigate. In general, Full Factorial Design is the most efficient for this type of experiments. Since it is important to understand relationships between factors and responses, Full Factorial Design is used in this thesis, so that all possible levels of the factors are investigated. The main advantage of Full Factorial Design is that it allows the effects of a factor to be estimated at different levels of other factors.

For DOE studies, Minitab software is used. To complete Full Factorial Design process, steps, summarized in Figure 3-3, must be followed [33].

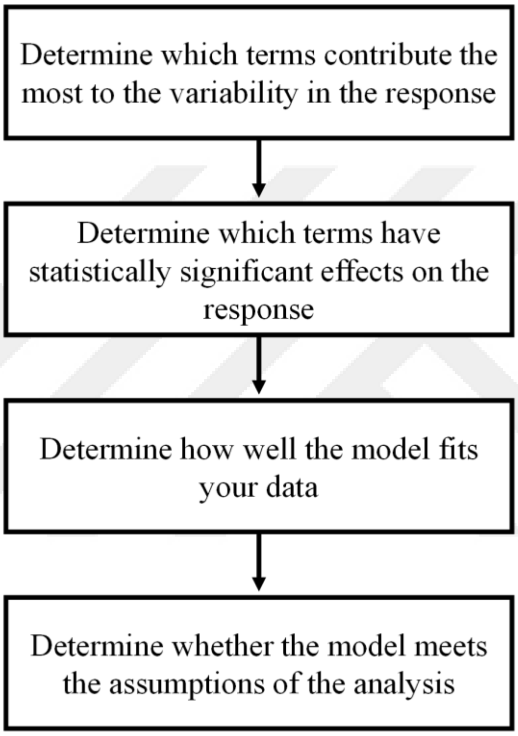

Figure 3-3. Algorithm for full factorial design

<u>Step 1</u>: The first evaluation, or discussion, to be made according to the results decides which factor affects more the responses. In the scope of this thesis, Pareto charts are used to display standardized effects. Thanks to the Pareto charts, relative magnitude and statistical significance of both main and interaction effects are presented with decreasing order. In this study, significance level of 0.05 is used to draw the reference line. In main and interaction effects plot, values are calculated as average

for corresponding factors. In other words, while calculating the mean value of a factor that is kept constant, the arithmetic average of the values is taken [35].

Step 2: In the second step, it is determined whether the relation between the response and factors in the model is statistically significant, or not. To do that, p-values for the factors are compared. A Significance level (shown with α) 0.05 means that there is a %5 risk of concluding that an association exists when there is no association between factors and response.

If p-value is less than or equal to the specified significance level, it can be concluded that there is a statistically significant relation between the factor and the response.

If p-value is higher than the significance, it cannot be concluded that there is a statistically significant association between the factor and response. For that model, factor can be corrected or subtracted from the Design of Experiment.

Step 3: After Full Factorial Design model is constructed, how well the model fits observed data must be determined. To do that, the goodness of fit statistics is examined. There are 2 important values S (standard deviation) and R-sq (R^2).

Standard deviation (S) is measured in the units of the response and represents how far the observed data fall from the fitted values. When S value is lower, it means that model describes the response well. Standard deviation formula can be written as:

$$S = \sqrt{\frac{1}{n}\sum(y_i - \hat{y}_i)^2} \tag{3.22}$$

R-sq, also called "Coefficient of Determination", is the percentage of the variation in response which is explained by the model. R-sq values are always between %0 and %100, and higher R-sq means that model fits well. Formulation can be shown as:

$$R^2 = 1 - \frac{\sum(y_i - \hat{y}_i)^2}{\sum(y_i - \bar{y}_i)^2} \tag{3.23}$$

Step 4: At the last step, residual plots are used to verify model, and it is controlled whether it meets the assumptions of the analysis, or not. If the model is not adequate and not fit the data, model must be modified [33]. It must be noted that this step is completed at low R-sq or high standard deviation values.

After performing the analysis, data is collected to predict the response with new observations, plot the relationships between the variables and find values which optimize one or more responses.

In order to describe the relationship between the predicted value and the response, regression equations, using the ordinary least square method [33] with observed data, are presented. The form of the regression equation can be written as:

$$y = b_0 + b_1 x_1 + b_2 x_2 + \cdots + b_k x_k \tag{3.24}$$

where y is the response variable in this equation.

In the thesis, the values obtained as a result of the numerical studies were examined, and optimization for fit values are done by Minitab Response Optimizer package. Optimization study for the baffle study is done to identify the combination of input variables which optimize response or a set of responses. The general steps followed for optimization studies is summarized in Figure 3-4.

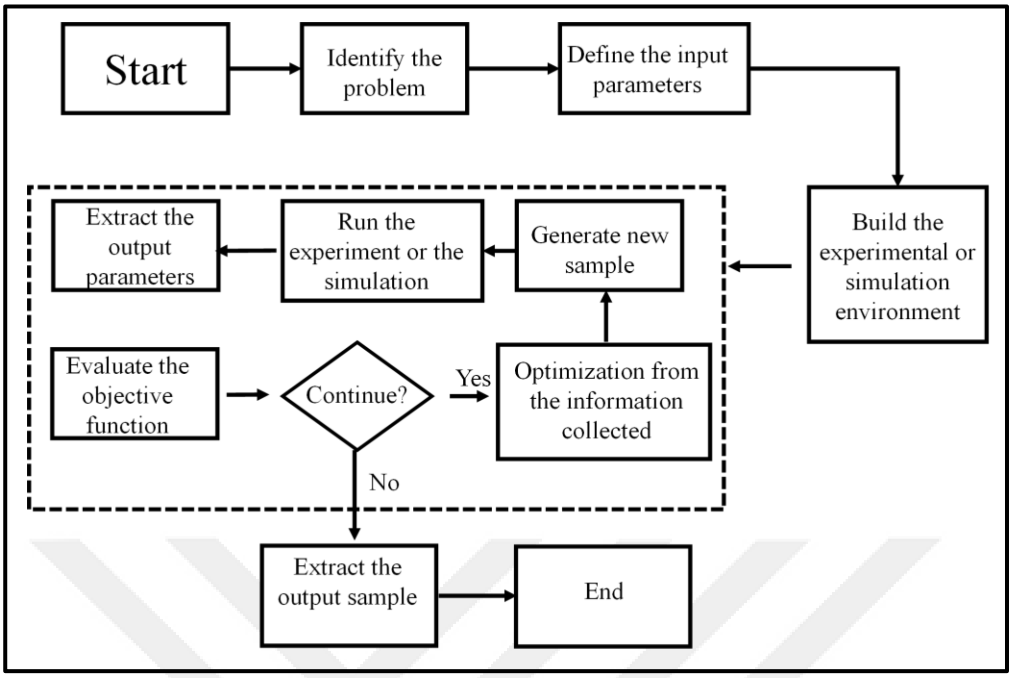

Figure 3-4. Optimization flowchart [36]

The most important parameter of an optimization study is desirability. It is simply a value between 0 and 1, and a measure of how close to optimum values are reached [36].

In order to calculate the composite desirability value, first the individual desirability values are calculated. When the value is 1, it means that the optimum result has been reached. These calculations are related to how the results will be optimized.

To illustrate, if a response is aimed to reach the maximum value at the end of optimization studies, the individual desirability is calculated as:

$$d_i = 0 \qquad \hat{y}_i < L_i \tag{3.25}$$

$$d_i = \left((\hat{y}_i - L_i) \,/\, (T_i - L_i)\right)^{r_i} \qquad L_i \leq \hat{y}_i \leq T_i \tag{3.26}$$

$$d_i = 1 \qquad \hat{y}_i > L_i \tag{3.27}$$

If a response is aimed to reach the minimum value;

$$d_i = 0 \qquad \hat{y}_i > U_i \tag{3.28}$$

$$d_i = \left((U_i - \hat{y}_i) \ / \ (U_i - T_i) \right)^{r_i} \qquad T_i \leq \hat{y}_i \leq U_i \tag{3.29}$$

$$d_i = 1 \qquad \hat{y}_i < T_i \tag{3.30}$$

After calculating individual desirability values, composite desirability value, D, is calculated as:

$$D = (d_1 \cdot d_{2\cdot} \ldots d_n)^{\frac{1}{n}} \tag{3.31}$$

3.3 Experimental Methodology

In order to validate numerical analysis conducted within the scope of the thesis, an experimental setup was designed, and an experimental procedure is prepared. The air conditioning system is located in a control room. The control room air temperature is set to 50˚C, the worst ambient condition indicated in the related standard [38]. Experimental setup in the control room and multi-purpose box with the outer chamber and the inlet channel are shown in Figure 3-5.

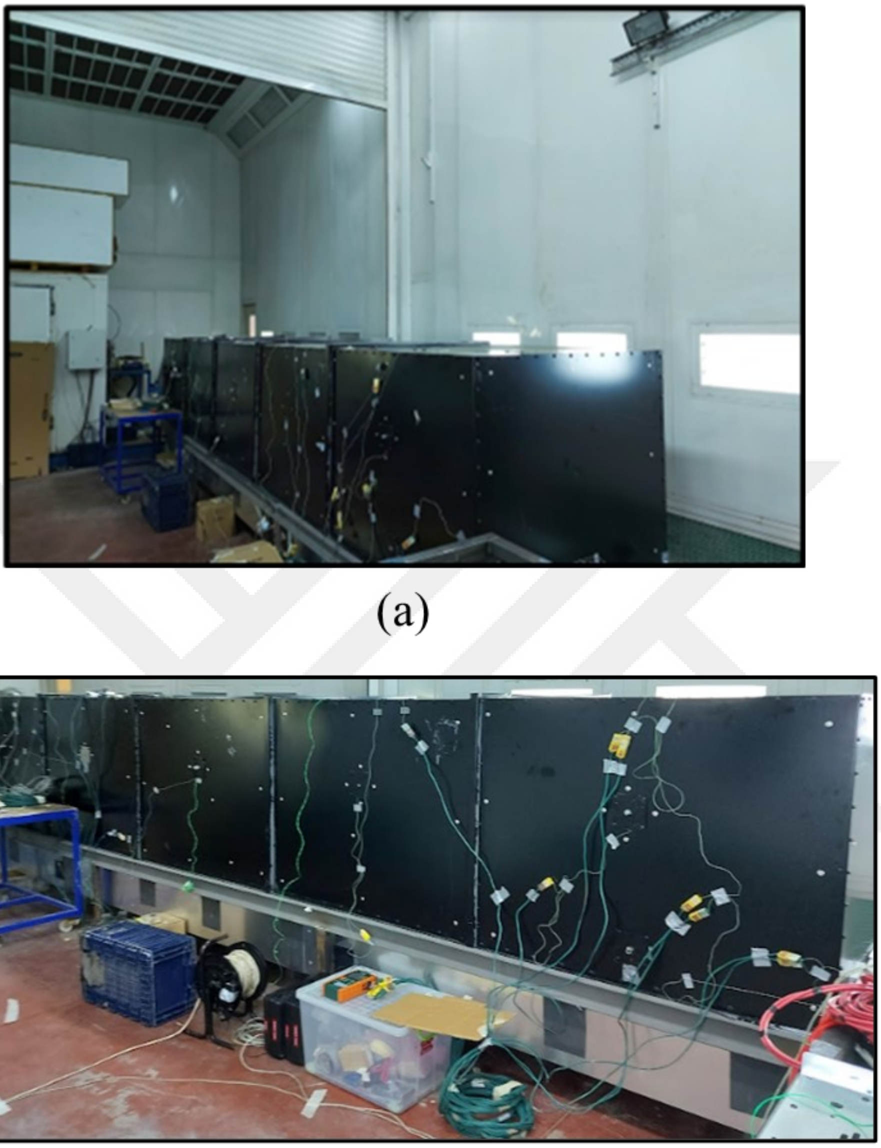

(a)

(b)

Figure 3-5. a) Experimental setup in the control room, b) multi-purpose box with the outer chamber and the inlet channel

The experimental setup was designed and integrated in parts due to its large volume. 10 mm insulation material, whose thermal conductivity is 0.036 W/(m.K), was used on the inlet channel, outlet channel, registers and inner surface of the chamber. Multi-purpose box, supply register and insulation material are shown in Figure 3-6. Detailed explanations will be given in Chapter 5.

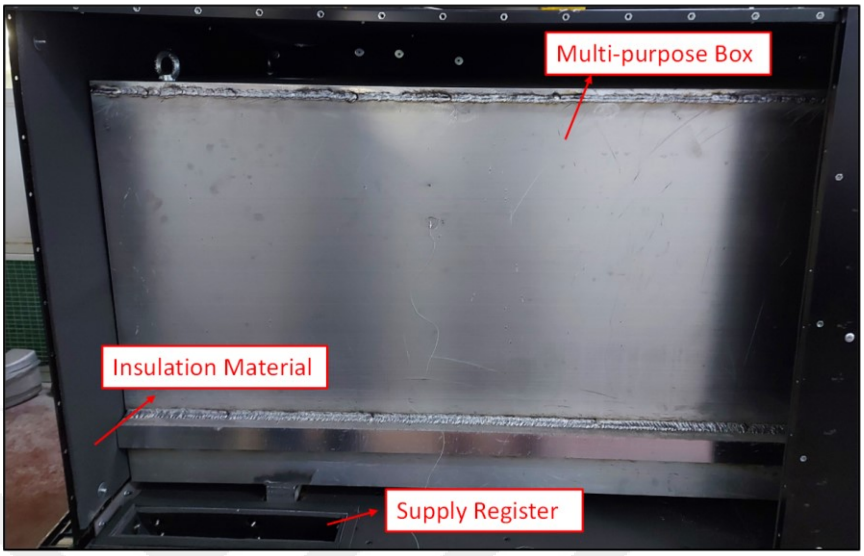

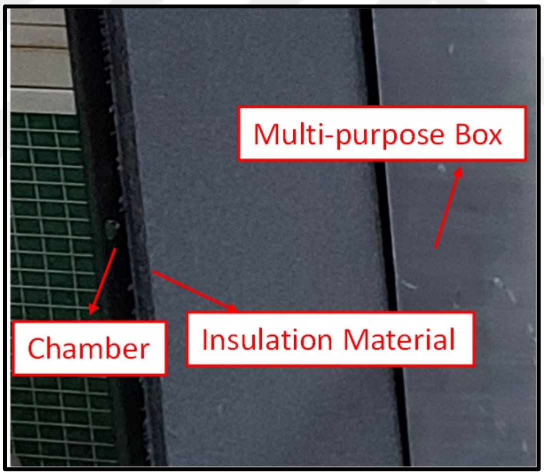

Figure 3-6. Multi-purpose box, supply register and insulation material

Totally, 22 TC-Direct K type welded tip PFA thermocouples with -75˚C to +250˚C operating range were used to make temperature measurements [39, 40].

17 of thermocouples are on the surface of the multi-purpose box, 3 of them are inside the multi-purpose box and 2 of them are at the inlet and outlet channels. The locations

of the thermocouples are given in Chapter 4, in detail. The image of K-type thermocouples used in the experimental studies is shown in Figure 3-7.

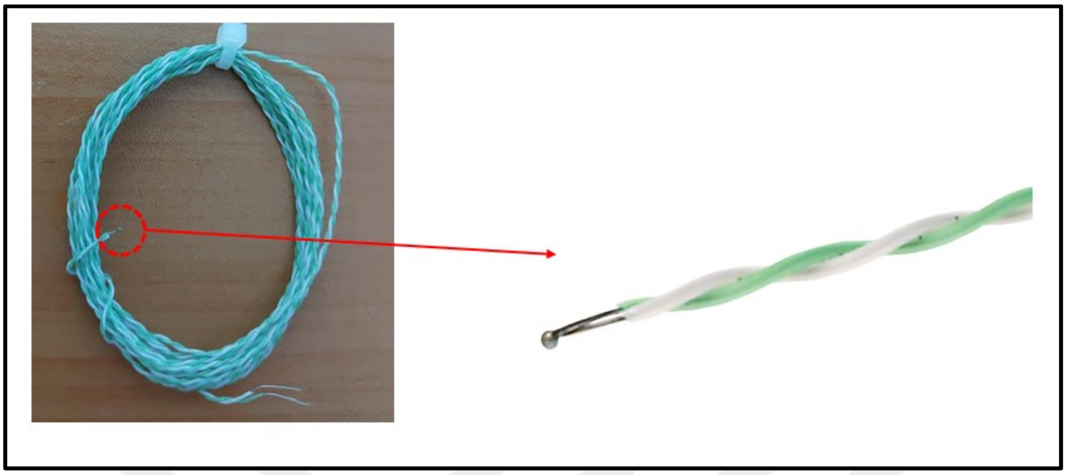

Figure 3-7. K-type thermocouple

In order to measure the temperatures, 2 different handheld instruments, OMEGA RDXL12SD and EXTECH TM500 are used. Both devices have 12 channels each. The image of the measuring devices used in the experimental setup is given in Figure 3-8.

Figure 3-8. 12-Channel temperature measurement devices [41, 42]

Within the scope of the studies, pressure sensors and pressure transmitters were used to calculate volumetric flow rate passing through the supply registers. Since it is difficult to measure the pressure inside the channels, a sensor working with the averaged pitot tube principle was used [43].

The sensors, which are placed at the inlet channel as "+" shape, from the side and top, enable to calculate the average air velocity to be determined by scanning the entire cross section by connecting their outputs parallel to each other. The arranged holes are placed against the flow direction to measure total pressure, and parallel to flow to measure static pressure of the air in the duct. The difference between them gives dynamic pressure, and velocity is calculated.

$$P_T = P_S + P_D \tag{3.32}$$

$$P_D = \frac{1}{2} p V^2 \tag{3.33}$$

Schematic view of the in-channel averaged pitot tube pressure sensor is given in Figure 3-9.

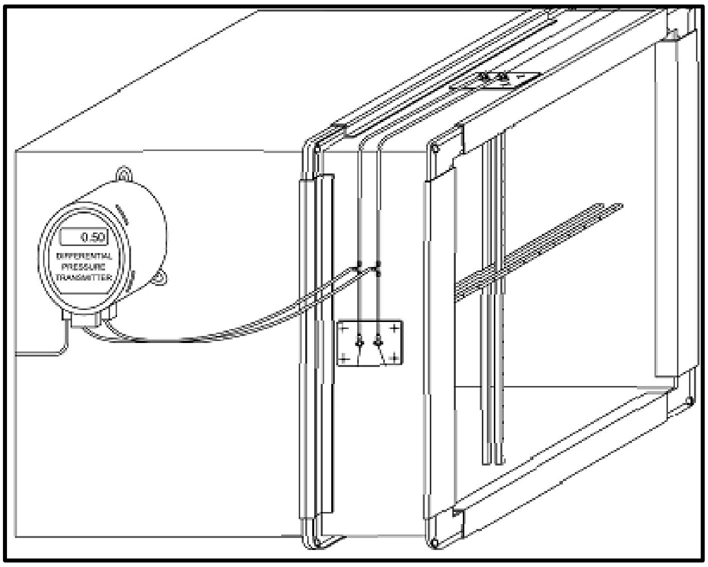

Figure 3-9. In-channel averaged pitot tube pressure sensor [43]

Dwyer model pressure transmitter was used for pitot tubes. The electrical source of these transmitters is 7-30 V DC. The image of the pitot tube and the sensor assembly is given in Figure 3-10 and Figure 3-11, respectively. A total of 3 sensors were used. More detailed information about the locations of the sensors will be given in Chapter 5.

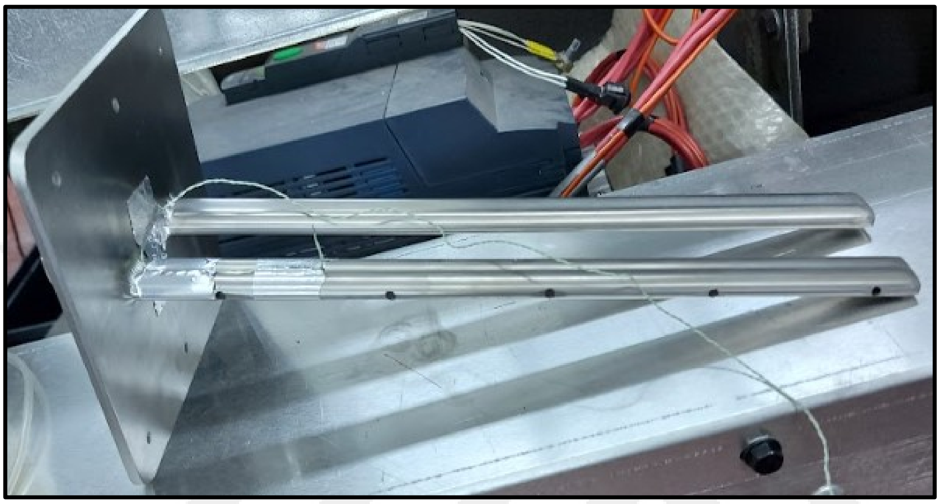

Figure 3-10. The pitot tube

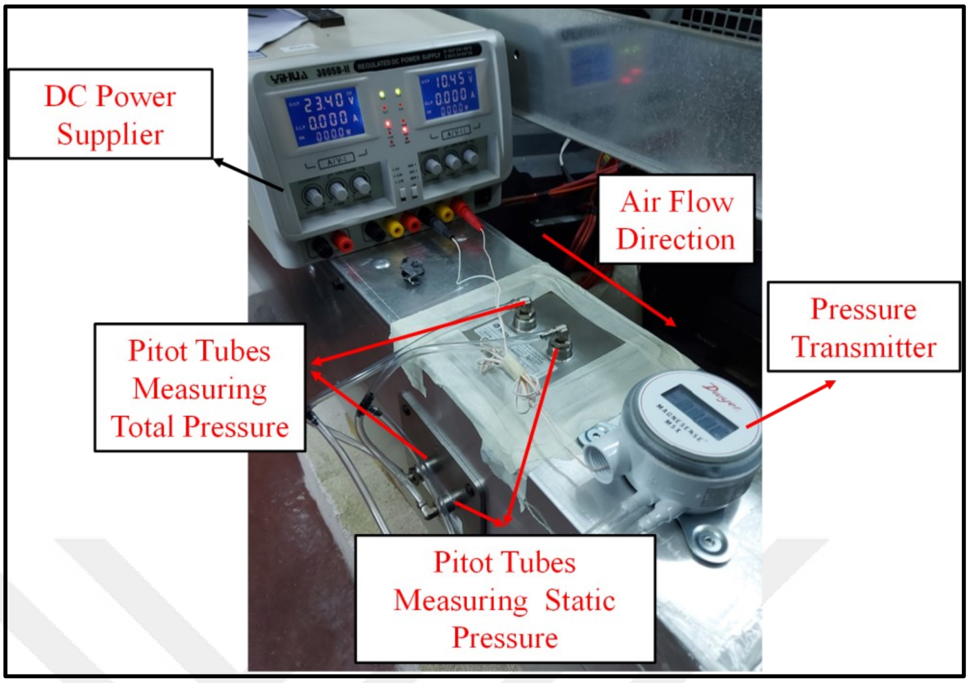

Figure 3-11. In-channel averaged pitot tube pressure sensor

An experimental procedure was determined for all the experimental studies carried out within the scope of the thesis. This procedure was repeated in the same way before each experiment. The procedure consists of two steps. First, the control room is set to 50˚C and waited for 1 hour. Then, the blower of the AC unit is operated at the ambient temperature for 15 minutes, in this way the conditioning of the multi-purpose box and the air inside to initial temperature (25˚C) is accelerated. The times specified in this procedure (1 hr + 15 min) have been determined by obtaining the lowest temperature (25˚C) on the surface of the multi-purpose box. It should be noted that an ambient temperature of 50˚C was applied by the control room through the entire experimental studies. In other words, it is set to give constant temperature of 50˚C for a total of 5 hours and 15 minutes, including the preconditioning and experiment time.

After the experiment starts, the ambient temperature, or the air suction temperature of the condenser, is shown in Figure 3-12.

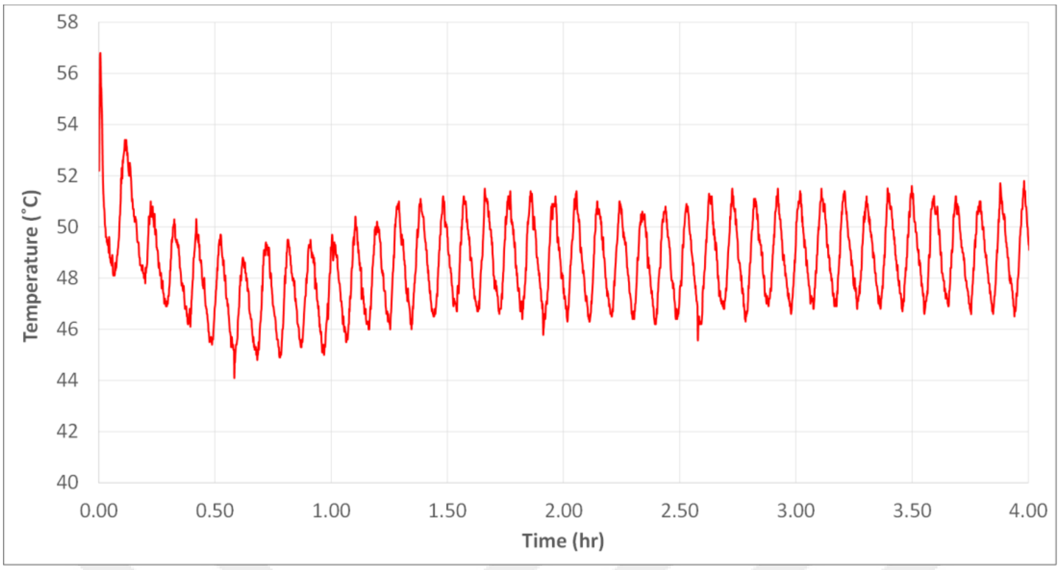

Figure 3-12. Condenser air suction temperature

The fluctuation in the suction temperature is because of the control room. This fluctuation also causes fluctuations in the temperature of air in the inlet channel, leaving the evaporator. Evaluations on the subject are explained in Chapter 5, in detail.

As it will be explained in Chapter 5, the duration of some experimental studies is approximately 2.75 hours, while others are 4 hours. It varies due to the limited usage time of the control room. For this reason, the experiments performed to validate the analysis studies were carried out for 4 hours. In addition, the experimental studies, carried out to experimentally see the effect of two factors (supply register position and supply register area percentage) on the temperatures, continued for 2.75 hours. It is observed that the results obtained in the experiments lasting 2.75 hours were sufficient to see the effect of the factors.

CHAPTER 4

NUMERICAL STUDIES

4.1 Introduction

STAR CCM+ is a software that is widely used in CFD applications. It simulates flows across a wide range of flow regimes. It solves conservation equations for mass, momentum and energy for compressible and incompressible fluids.

CFD models were constructed in Star CCM+ environment to find the best supply and return register configuration for the defined problem. As it is mentioned in Chapter 1 and Chapter 2, position of the registers and their sizes change the cooling characteristic due to change in boundary conditions for registers. The numerically analyzed domains are shown in Figure 4-1.

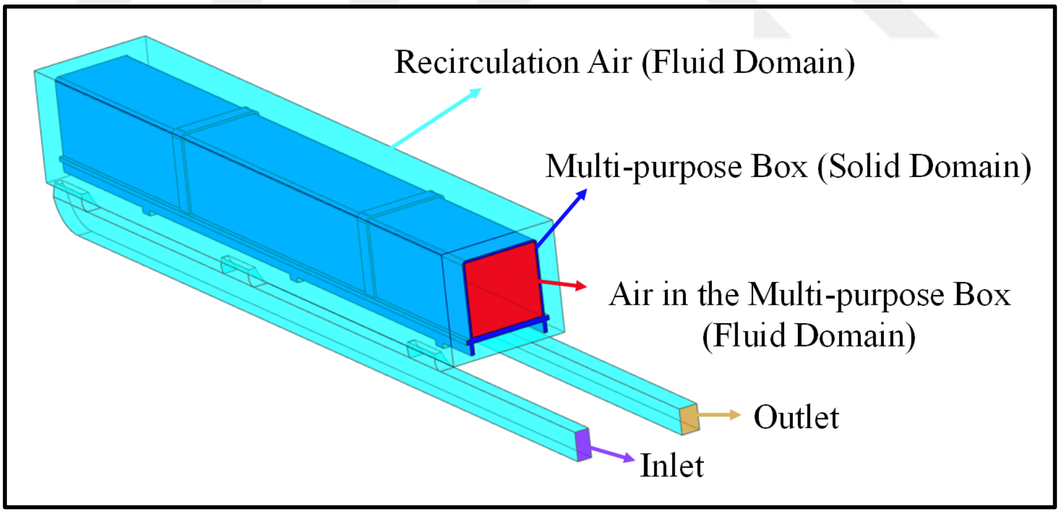

Figure 4-1. The numerically analyzed domains

Material of the multi-purpose box is aluminium. The values assigned for the materials in the CFD model are given in Table 4-1.

Table 4-1. Thermo-physical properties and parameters for the materials

Domains	Properties	Values
Recirculation Air (@ 101.3 kPa and 5˚C)	Density [kg/m^3]	1.26
	Viscosity [Pa.s]	1.74E-05
	Specific Heat [J/kg.K]	1006.6
	Conductivity [W/m.K]	0.02454
The Multi-Purpose Box	Density [kg/m^3]	2702
	Specific Heat [J/kg.K]	903
	Conductivity [W/m.K]	237
	Thickness [mm]	4
The Air in the Multi-purpose Box (@ 101.3 kPa and 15˚C)	Density [kg/m^3]	1.26
	Viscosity [Pa.s]	1.86E-05
	Specific Heat [J/kg.K]	1003.6
	Conductivity [W/m.K]	0.02603

The recirculation air fills the space between the chamber and the multi-purpose box and causes convectional heat transfer on the multi-purpose box. The wall boundary condition of the recirculation air region is set as adiabatic, since chamber is assumed well insulated. The multi-purpose box was placed inside the chamber with wedges. The air in the multi-purpose box fills inside the multi-purpose box. The boundary and initial conditions were applied for the unsteady analyses. Inlet boundary condition was set as “Velocity Inlet”, and outlet boundary condition was set as “Pressure Outlet”. Wall boundary condition of the recirculation air region was set as “Wall” with no heat flux. The interfaces between the recirculation air and the multi-purpose-box, and the multi-purpose box and the air inside were set as “Mapped Contact Interface”. Initial temperature for all regions was set as 25˚C. The boundary conditions are shown in Figure 4-2.

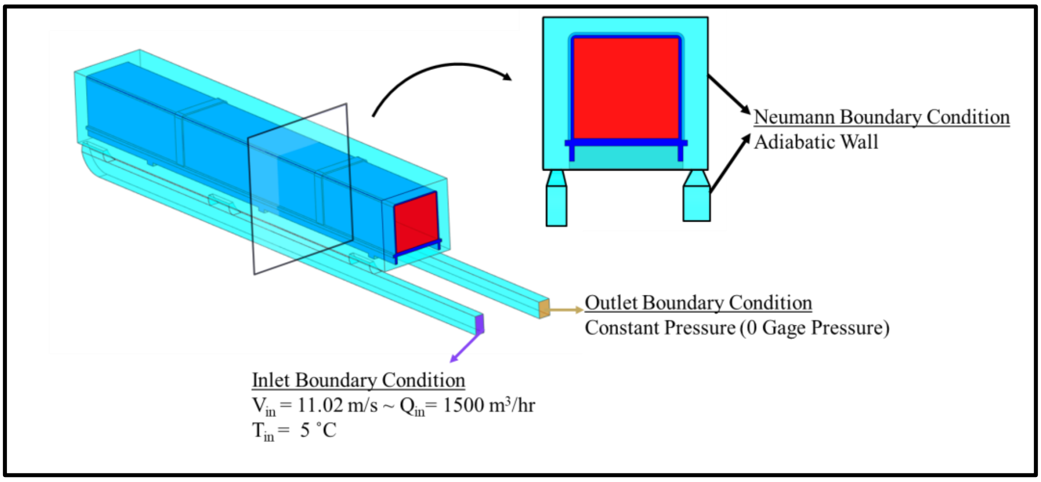

Figure 4-2. Boundary conditions

To find the best supply and return register configuration, 4 factors were examined, and CFD models were installed with respect to these factors. They are as follows:

- Supply Register Position
- Return Register Position
- Supply Register Area Percentage
- Return Register Area Percentage

Representative image for a configuration can be shown in Figure 4-3.

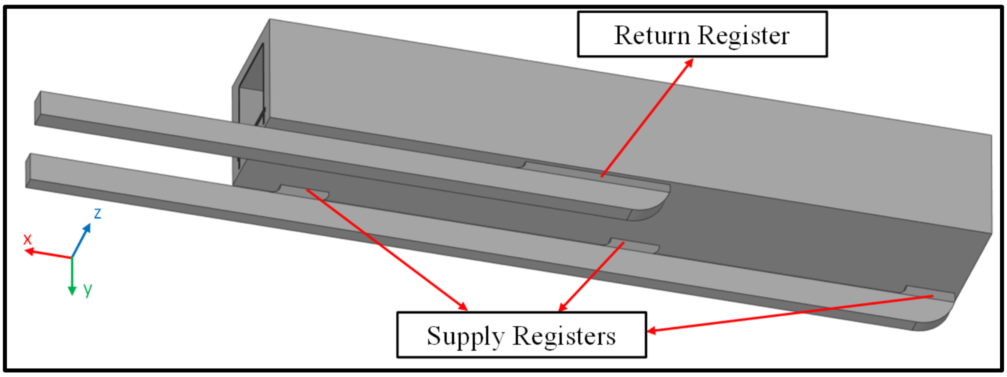

Figure 4-3. Representative image for supply and return registers

The levels of these factors are tabulated in Table 4-2.

Table 4-2. Levels of factors

Factors	**Number of Levels**	**Levels**
Supply Register Position	3	M, D and T
Return Register Position	2	M, D
Supply Register Area to Total Area Ratio	3	20%, 35% and 50%
Return Register Area to Total Area Ratio	3	20%, 35% and 50%

As it is mentioned before, there are 2 factors in letter type levels (supply register position and return register position) that show position and number of the registers, and 2 factors in numeric type levels (supply register area percentage and return register area percentage) that show size of the registers. Considering the levels and factors, there are 54 different configurations.

Configurations were coded with two letters and two numerical values for systematic evaluation of results of CFD models and DOE studies. The first two letters indicate the position of the supply and return registers in sequence. Here, “M”, “D” and “T” are abbreviations of “Mono”, “Dual” and “Triplum”. Some configurations are shown in Figure 4-4 as an example.

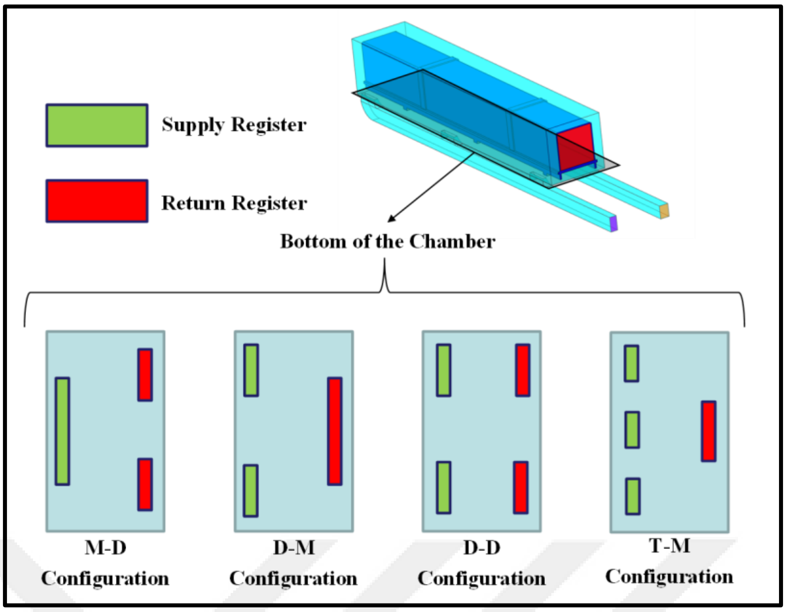

Figure 4-4. Illustration of register position configurations

The 2 numeric values, used to name the configurations, show area ratios. As it is shown in Table 4-2, there are 3 levels (20%, 35% and 50%) of 2 numeric factors. Area ratios are shown as percentages, and they represent the ratio of the totally used area to the available usable area for each configuration. The representative image is given in Figure 4-5.

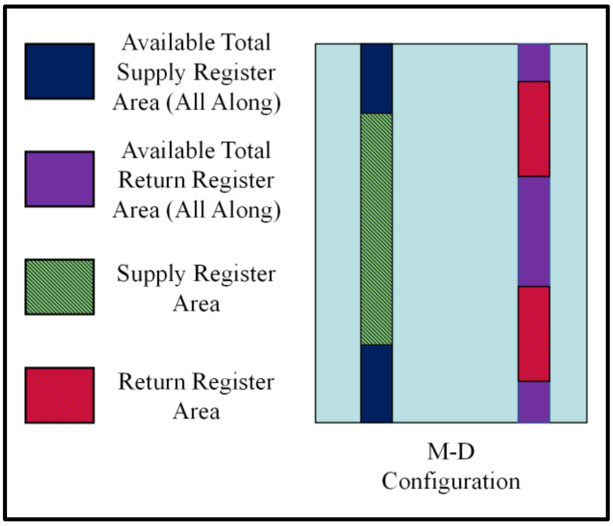

Figure 4-5. Representation of numeric factors and their levels

The solution domain of the area percentages for the supply and return registers was examined between 20% and 50%. As mentioned before, there are many subsystems around the chamber. This limits the area percentage of the registers to 56%, thus the maximum area percentage was determined as 50%. The minimum area percentage 20% for the registers was determined by considering the pressure loss. Pressure loss in the ducting increases due to the increase in the velocity of the recirculation air in the chamber, and it affects the operating conditions of the blower in AC unit. Therefore, the lower limit of the solution domain was determined as 20%.

The positions of the registers in the configurations were determined according to the construction of the chamber structure.

Finally, some configurations created for the systematic naming of the samples are given in Figure 4-6. For example, D-M-35-50 represents binary supply register and single return register configuration. At the same time, “20” represents the ratio of the total green area (total supply register area) to the available area, and “50” represents the ratio of the total red area (total return register area) to available area as a percentage. It should be noted that width of the supply and return registers are constant and 70 mm, and the long side of the available areas is 6600 mm. Some configurations are shown in Figure 4-6.

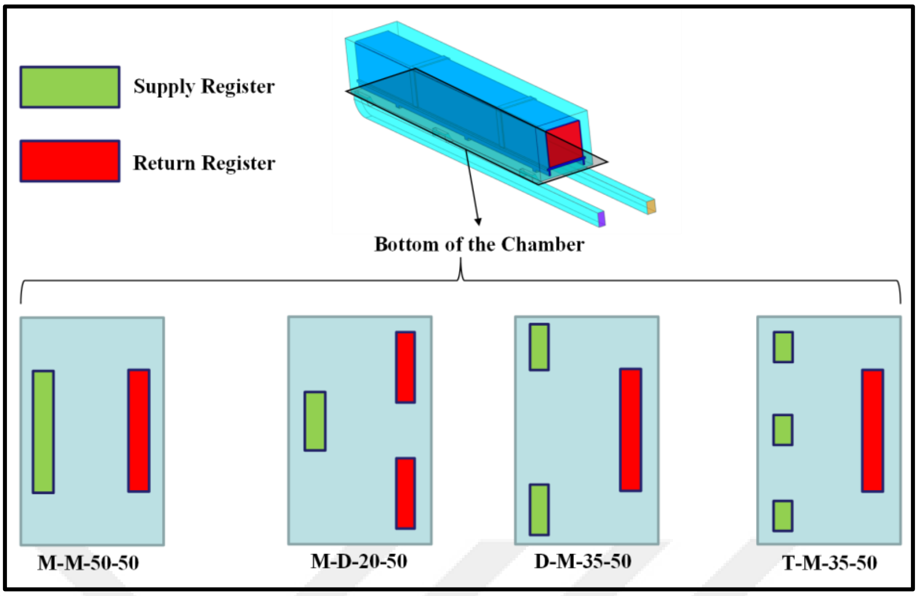

Figure 4-6. Systematic naming of configurations

To sum up, a total of 54 CFD models were analysed, considering the factors and their levels.

4.2 Mesh Independence Study

Mesh independence studies are performed to show that results in numerical solutions do not change with respect to number of cells in the whole solution domain. One of the most important factors for a good mesh is that they should be fine enough, having good quality and relatively good distribution. However, it should be noted that, there is an important trade-off between the accuracy of simulation and the computation time. As mentioned before, 54 analyses were carried out to examine the effects of position and area of the supply and return registers. 3 numeric domains, the recirculation air, the multi-purpose box and the air inside, were discretized into cells, separately. Since, there is no need for a fine mesh for numerical solutions in the solid domain, the same mesh configuration, in resolution manner, is not used in the fluid and solid domain.

Trimmed cell mesher, included in the CFD software STAR CCM+, was used to generate meshes for solution domains. According to mesh independence analysis, TM2020 configuration was chosen for the studies to be carried out. 4 different mesh sizes coarse, medium, fine and very fine with 770 K, 1.8 M, 2.95 M and 12.6 M cells were used, respectively. In these mesh sizes, 1-hour analyses were run with 0.1 s time steps. In these studies, the methods and directions in the "Guide of AIAA" [44] were applied.

In Figure 4-7, change in outlet temperature, taken as surface average temperature on the outlet boundary, in 1 hour for different mesh sizes are shown. In addition, the section with the highest relative approximate error (maximum %3 for the coarse mesh), according to the mesh sizes was shown in the specified time interval (100 s - 1200 s) in Figure 4-8. It is observed that solution is insensitive for further mesh refinements.

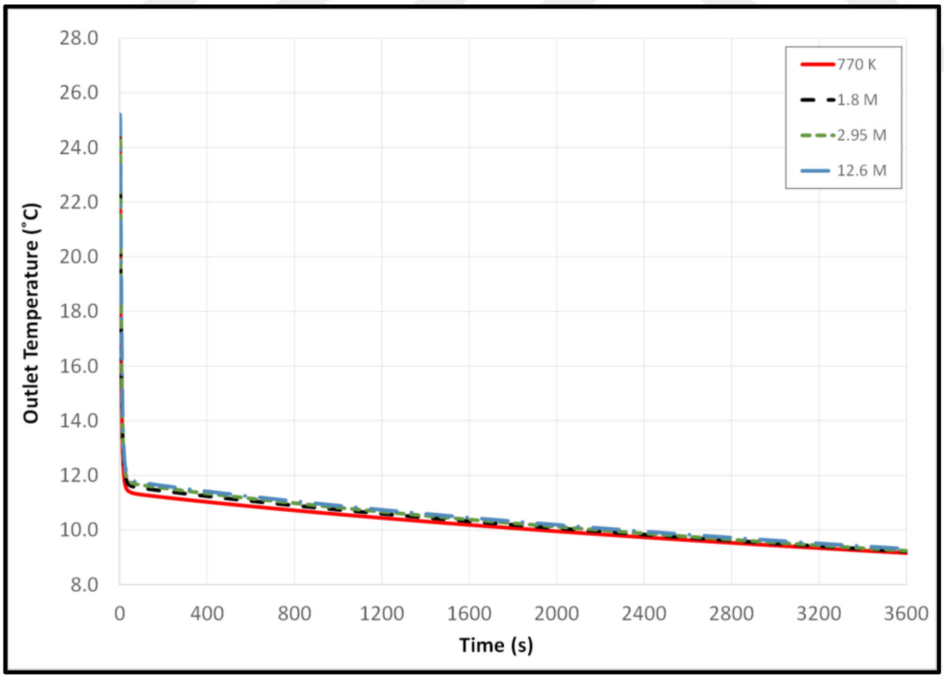

Figure 4-7. Change in outlet temperature for different mesh sizes

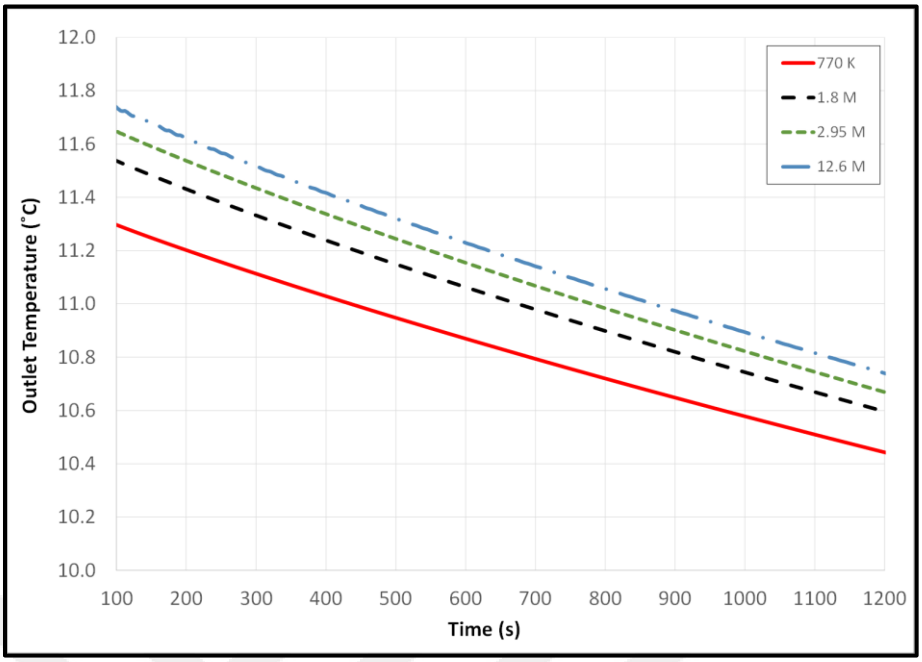

Figure 4-8. Change in outlet temperature for different mesh sizes in the specified time interval

According to Freitas (2006), systematic grid refinement is very important for the verification processes for either codes or solutions. To do that Grid Convergence Index (GCI) method is used. The method can be summarized with 5 simple steps as follows [45]:

Step 1: For non-structured meshes, a new value, or grid size *h* can be defined as [46]:

$$h = \left(\left(\sum_{i=1}^{N} \Delta V_i\right) / N\right)^{1/3} \tag{4.1}$$

where ΔV_i and N are volume of the ith cell and total number of cell used for the computations, respectively.

Step 2: Three mesh sizes are selected as coarse (770 K), fine (2.95 M) and very fine (12.6 M). The grid refinement factor, which should be greater than 1.3, can be defined as:

$$r = h_{coarser} / h_{finer} \tag{4.2}$$

Step 3: Let $h_1 < h_2 < h_3$, and $r_{21} = h_2 / h_1$, $r_{32} = h_3 / h_2$. Observed, or apparent order, p, can be found as:

$$s = 1 \cdot sign(\varepsilon_{32} \,/\, \varepsilon_{21}) \tag{4.3}$$

$$q(p) = \text{In}\left(\frac{r_{21}^{p} - s}{r_{32}^{p} - s}\right) \tag{4.4}$$

$$p = (1/\ln\,(r_{21}))[\ln\left|\frac{\varepsilon_{32}}{\varepsilon_{21}}\right| + q(p)] \tag{4.5}$$

And observed order p is found with iteratively, where;

$\varepsilon_{32} = \Phi_3 - \Phi_2$ and $\varepsilon_{21} = \Phi_2 - \Phi_1$, and Φ_i denoting the simulation value. In this case it is outlet temperature.

Step 4: Extrapolated simulation value (outlet temperature) can be found as:

$$\Phi_{ext}^{21} = \left(r_{21}^{p}\Phi_1 - \Phi_2\right) / \left(r_{21}^{p} - 1\right) \tag{4.6}$$

And Φ_{ext}^{32} can be found with similar way.

Step 5: Estimated extrapolated relative error and Grid Convergence Index can be found as:

$$e_{ext}^{21} = \left|\frac{\Phi_{ext}^{21} - \Phi_1}{\phi_{ext}^{21}}\right| \tag{4.7}$$

$$GCI_{fine}^{21} = \frac{F_s . e_{ext}^{21}}{r_{21}^{p} - 1} \tag{4.8}$$

F_s is the safety factor and assigned 3 according to experimental studies by Roache [47]. It is also suggested that using a value of 1.25 gives considerably good results [48]. In this thesis, factor of safety is used as 3, and according to calculations, extrapolated outlet temperature, at the end of 1 hour, is found as 9.23˚C ± 0.002 % of the nominal value, which means mesh independent results are almost achieved.

In Table 4-3, pressure drop, calculated as mass flow averaged absolute total pressure difference between the inlet and outlet boundaries, is also tabulated, and approximate relative errors are shown.

Table 4-3. Pressure drops between the inlet and outlet with respect to different mesh sizes

Total Cell Number	**770 K**	**1.8 M**	**2.95 M**	**12.6 M**
Pressure Drop Btw. Inlet and Outlet (Pa)	139.27	145.88	147.08	148.84
%App. Rel. Error	6.43	2.00	1.18	-

Analyses are run for the first 1 hour, and a computer with 50 CPU was used. Total run time values for analyses are tabulated in Table 4-4.

Table 4-4. Total run time for 1-hour analyses with respect to different mesh sizes

Mesh Size	**Total Run Time (hr)**
770 K	17.13
1.8 M	42.16
2.95 M	48.62
12.6 M	311.24

Considering the convergence of outlet temperature of the analyses and the run time, mesh size with 1.8 M was selected for time step independence study. Scenes for the specified mesh are given in Figure 4-9 and Appendix A.

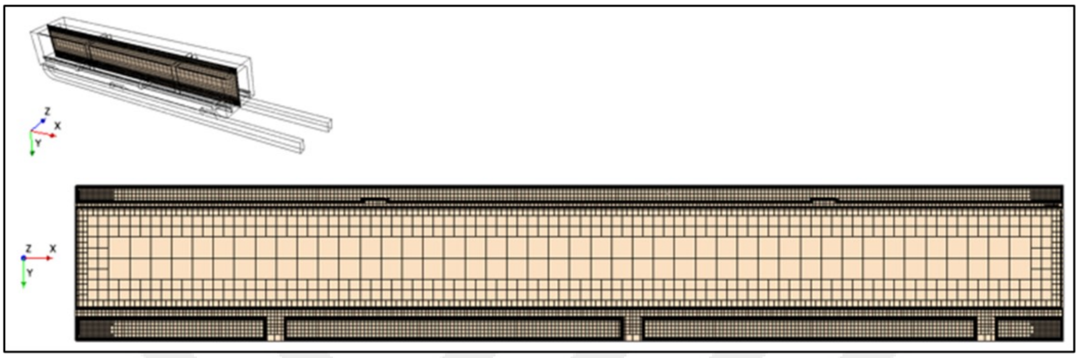

Figure 4-9. Meshed CFD model (1.8 M Mesh)

4.3 Time Step Independence Study

Time step independence studies were carried out to see the effect of the time step on the solutions in numerical analyses. As it is mentioned, time step 0.1 s was selected for mesh independence study. Analyses were run with 3 different time steps 0.2 s, 0.1 s and 0.05 s for 1.8 M mesh size. Change in the temperature at the outlet with respect to different time steps are presented in Figure 4-10. In addition, the section with the highest relative approximate error (maximum %0.1), according to the different time steps was shown in the specified time interval (2800 s - 3600 s) in Figure 4-11.

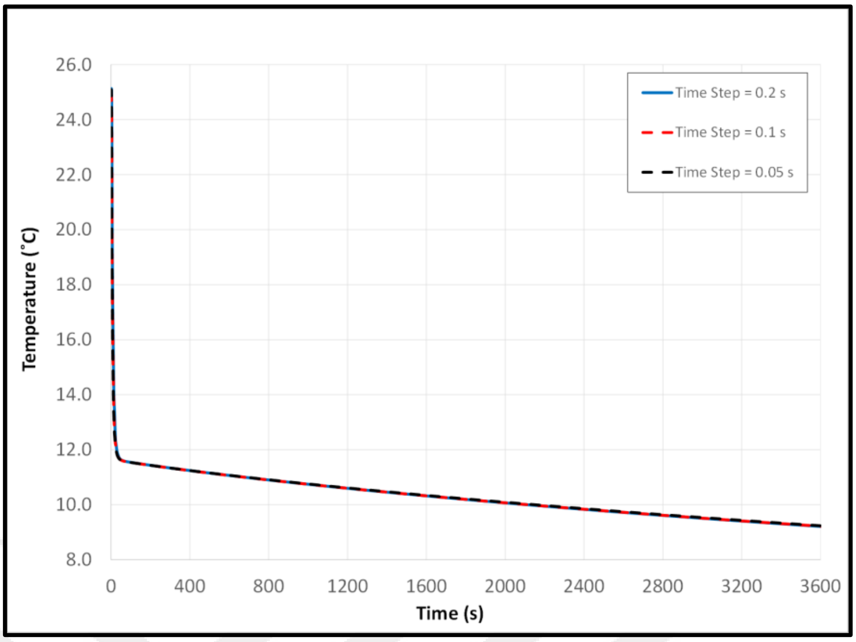

Figure 4-10. Change in outlet temperature for different time steps

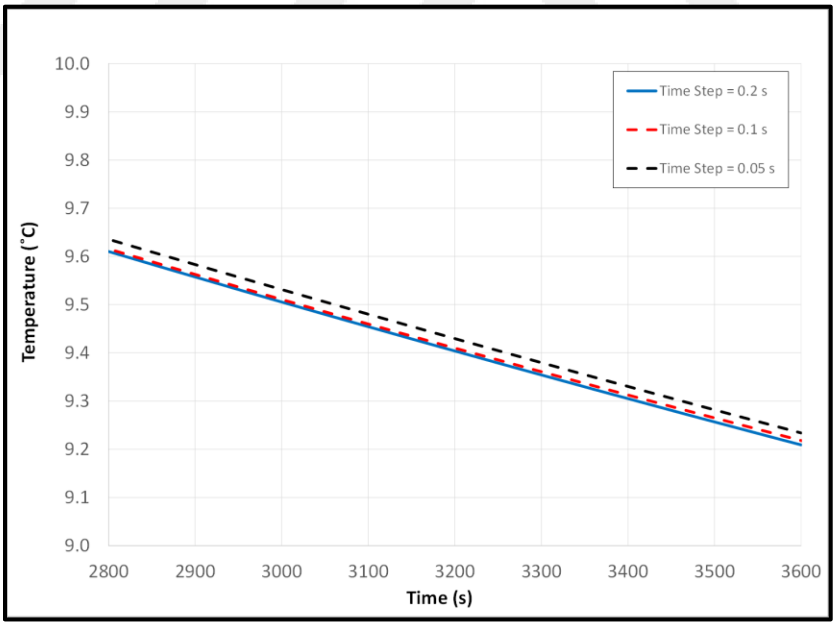

Figure 4-11. Change in the outlet temperature for different time steps for specified time interval

Pressure drops, calculated as mass averaged, between the inlet and outlet with respect to different time steps and approximate relative errors are also tabulated in Table 4-5.

Table 4-5. Pressure drops between inlet and outlet with respect to different time steps

Time Step (s)	**0.2**	**0.1**	**0.05**
Pressure Drop Btw. Inlet and Outlet (Pa)	145.87	145.88	145.91
%App. Rel. Error	0.03	0.02	-

Total run time values for time step independence analyses are tabulated in

Table 4-6.

Table 4-6. Total run time for 1-hour analyses with respect to different time steps

Time Step (s)	**Total Run Time (hr)**
0.2	23.54
0.1	42.16
0.05	84.75

It should be noted that when time step was increased to 0.4 s, the results of the analysis diverged. Screenshot of the residual graph for the analysis with 0.4-time step is given in Appendix A.

According to the results, the surface average outlet temperature and pressure drop values are time-independent at the examined time steps. Considering the numerical analyses to be run and time considerations, 0.2 s time step was selected for future studies.

4.4 CFD Results and Statistical Evaluation

54 CFD analysis were run for 2.5 hours with respect to assumed boundary and initial conditions. The reason for running the analysis for 2.5 hours is to examine the effects of the factors in 2.5 hours on the temperature values of the multi-purpose box and the air inside, considering the computation time for 54 CFD analyses.

According to the results, given in Appendix B, pressure difference, between inlet and outlet, and surface average outlet temperature, on the outlet boundary, values at the end of 2.5 hours are very close to each other. The maximum differences between the values are 44.9 Pa and 0.66˚C, respectively. The reason for the low-pressure loss is the low velocity of the recirculation air in the chamber. For this reason, these parameters were not used in the evaluation of the results with statistical approach. Instead, regions of the air in the multi-purpose box that reach the target temperature by volume were examined. According to the numerical results, volume ratios (VR), defined in equation 4.9 are tabulated in Table 4-7.

$$VR = \frac{Air\ Volume\ in\ the\ Multipurpose\ Box\ with\ a\ Temperature\ Below\ 15^{\circ}\mathrm{C}}{Air\ Volume\ in\ the\ Multipurpose\ Box} \tag{4.9}$$

Table 4-7. VR values for different configurations at the end of 2.5 hours

#	Configuration	VR
1	MM2020	0.7041
2	MM2035	0.7145
3	MM2050	0.7669
4	MM3520	0.6384
5	MM3535	0.6780
6	MM3550	0.7673
7	MM5020	0.6084
8	MM5035	0.6250
9	MM5050	0.6803
10	MD2020	0.9417
11	MD2035	0.9573
#	**Configuration**	**VR**
12	MD2050	0.9451
13	MD3520	0.8476
14	MD3535	0.8736

15	MD3550	0.8561
16	MD5020	0.8530
17	MD5035	0.8855
18	MD5050	0.8486
19	DM2020	0.9404
20	DM2035	0.9572
21	DM2050	0.9504
22	DM3520	0.7601
#	**Configuration**	**VR**
23	DM3535	0.7680
24	DM3550	0.7935
25	DM5020	0.7918
26	DM5035	0.8104
27	DM5050	0.8473
28	DD2020	0.9197
29	DD2035	0.9222
30	DD2050	0.9202
31	DD3520	0.9054
32	DD3535	0.9153
33	DD3550	0.9182
34	DD5020	0.8493

35	DD5035	0.8986
36	DD5050	0.8785
37	TM2020	0.9765
38	TM2035	0.9450
#	**Configuration**	**VR**
39	TM2050	0.9244
40	TM3520	0.8998
41	TM3535	0.9178
42	TM3550	0.9111
43	TM5020	0.8469
44	TM5035	0.8748
45	TM5050	0.9173
46	TD2020	0.9642
47	TD2035	0.9564
48	TD2050	0.9450
49	TD3520	0.9321
50	TD3535	0.9143
51	TD3550	0.9114
52	TD5020	0.8582
53	TD5035	0.8749
54	TD5050	0.8606

According to the values given in Table 4-7, while 98 % of the air in the multi-purpose box was reduced to target temperature in the TM2020 configuration, only 60 % percent of it was reduced to the target temperature in the MM5020 configuration.

Temperature distribution of the multi-purpose box for configurations MM5020 and TM2020 at the end of 2.5 hours are shown in Figure 4-12 and Figure 4-13, respectively. In addition, there are 5 planes in these figures to show the temperature distribution of the air in the multi-purpose box. Distance between the planes is 1325 mm.

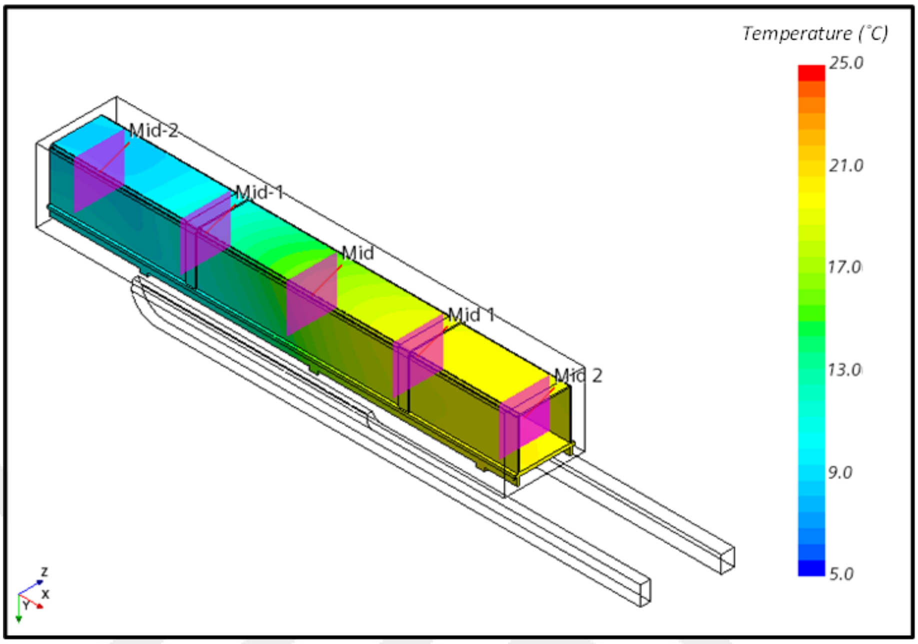

Figure 4-12. Temperature distribution of the multi-purpose box for configuration MM5020 at the end of 2.5 hours ("Mid" plane is at x=0 mm)

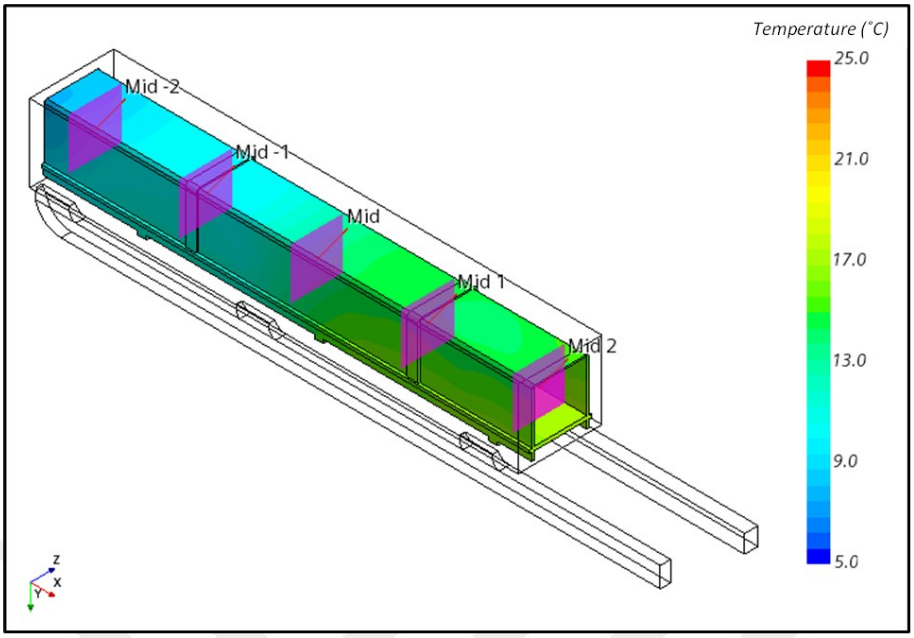

Figure 4-13. Temperature distribution of the multi-purpose box for configuration TM2020 at the end of 2.5 hours (“Mid” plane is at x=0 mm)

As shown in Figure 4-13, the target temperature could not be reached in some regions of the multi-purpose box for TM2020, which is one of the best configurations according based on VR. To show the time-dependent values of the temperature values on the multi-purpose box, temperature recording points were placed in some regions. Position and naming of them are given in Figure 4-14 and Figure 4-15, respectively. Location of them is also given in Appendix C. The temperature variation of these regions with respect to time is given in Figure 4-16. The number and position of the temperature recording points will remain the same for all numerical and experimental studies. According to Figure 4-13 and Figure 4-16, temperature of S-19 was calculated as 17.7 ˚C.

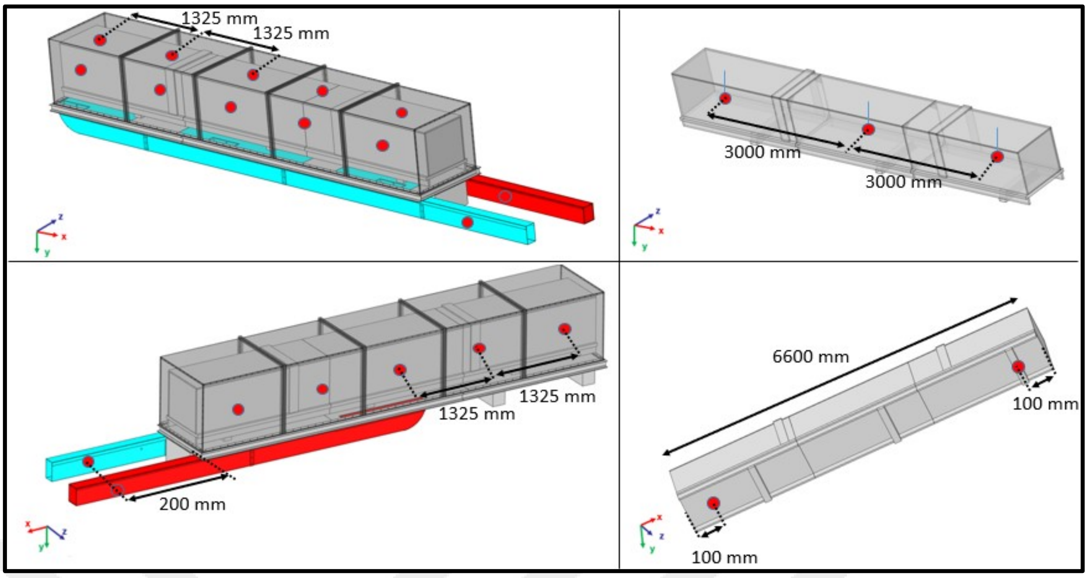

Figure 4-14. Position of the temperature recording points on the multi-purpose box in CFD models

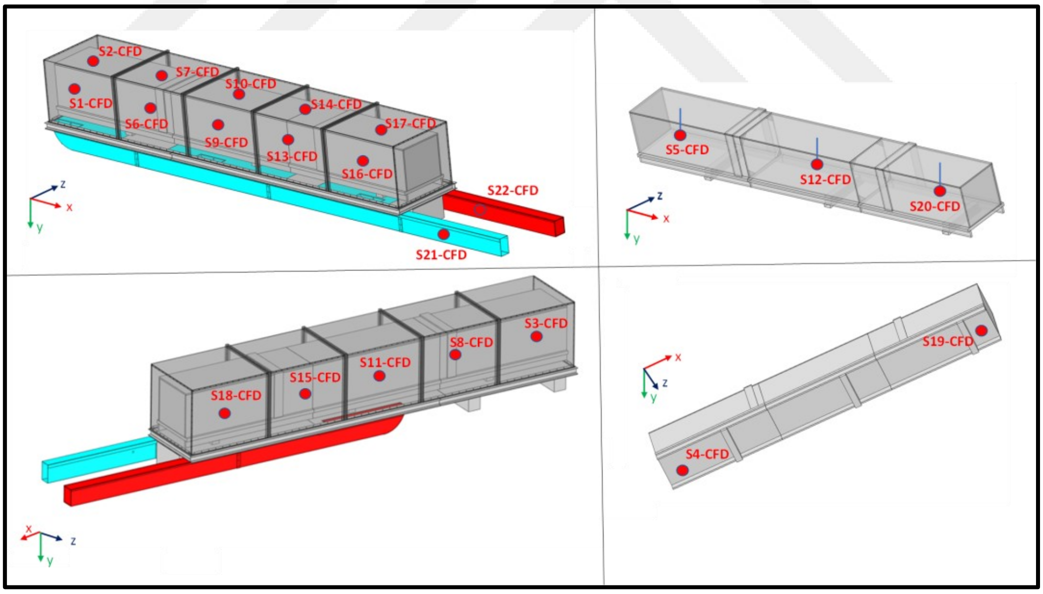

Figure 4-15. Naming for the temperature recording points in CFD models

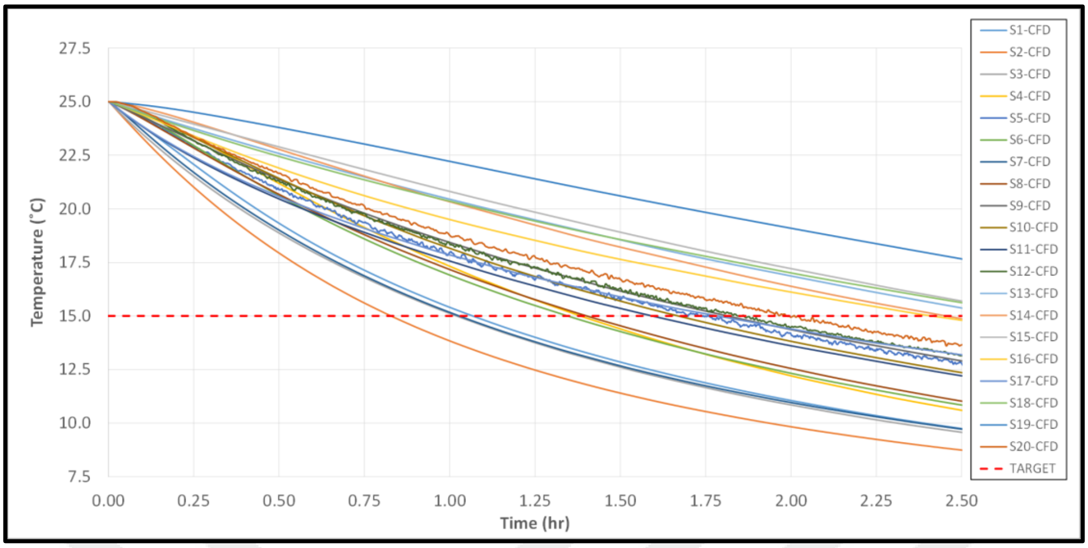

Figure 4-16. Temperature variation at the temperature recording points

Temperature distribution of the air in the multi-purpose box at the end of 2.5 hours for MM5020 and TM2020 configurations are shown in Figure 4-17 and Figure 4-18, respectively**.** In these figures, temperature contour is limited between 5˚C (theoretical minimum) and 15˚C (target temperature) to understand the regions reaching the target temperature more clearly. Regions that are not coloured in the frame are above 15˚C.

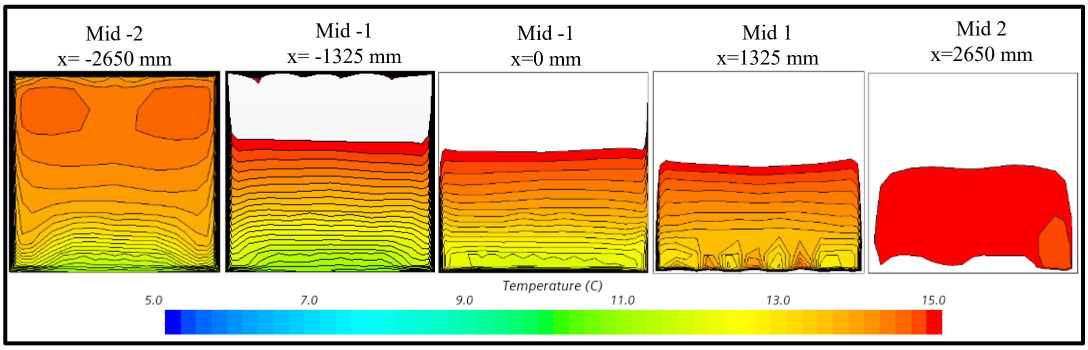

Figure 4-17. Temperature distribution of the air in the multi-purpose box for MM5020 configuration at the end of 2.5 hours

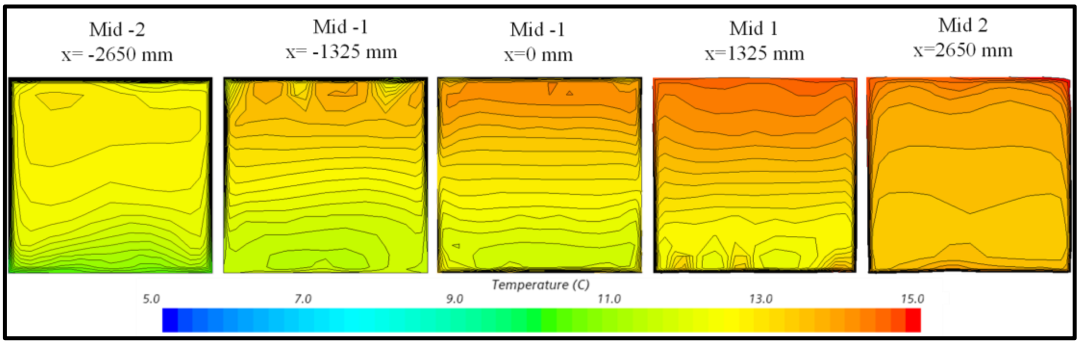

Figure 4-18. Temperature distribution of the air in the multi-purpose box for TM2020 configuration at the end of 2.5 hours

As it is shown from Figure 4-12, Figure 4-13, Figure 4-17 and Figure 4-18, both the multi-purpose box and the air inside were cooled faster and more at x= -2650 mm. The main reason for this situation is that the recirculation air coming from the inlet, reaches rear sections more due to the momentum it has for all configurations. An example is shown in Figure 4-19 for configuration TM2020. Moreover, there is temperature difference (4-4.5˚C) between two ends of the air in the multi-purpose box (between planes Mid 2 and Mid -2) in the multi-purpose box.

Velocity contours of the recirculation air for specified planes are shown in Figure 4-19 and Figure 4-20. According to the figures, there is also air flow at the bottom of the multi-purpose box. Especially, for some regions, the amount of recirculation air passing under the multi-purpose box is greater than the amount of air passing over the upper surface.

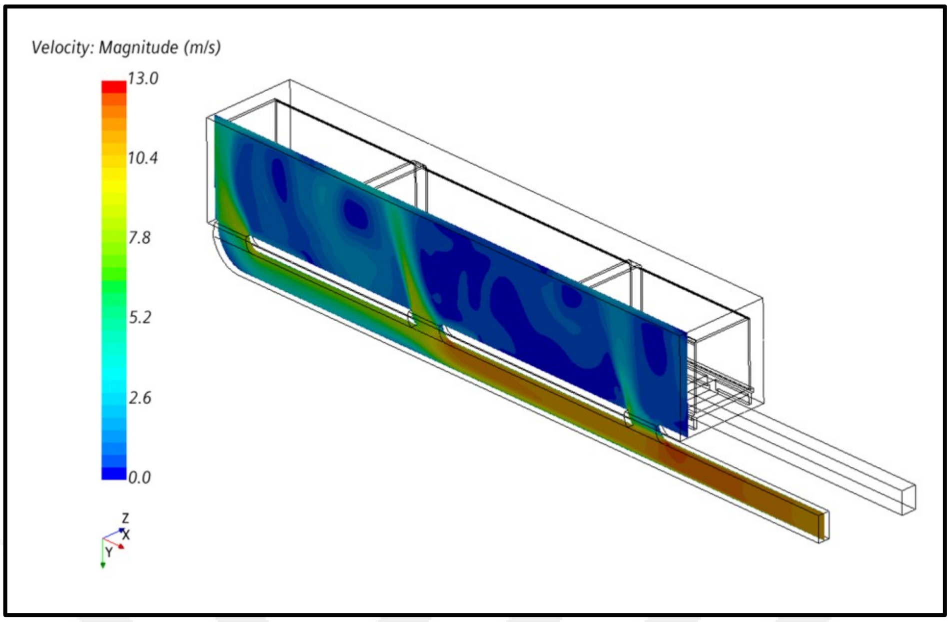

Figure 4-19. Velocity distribution of the recirculation air for configuration TM2020 (at t=2.5 hr)

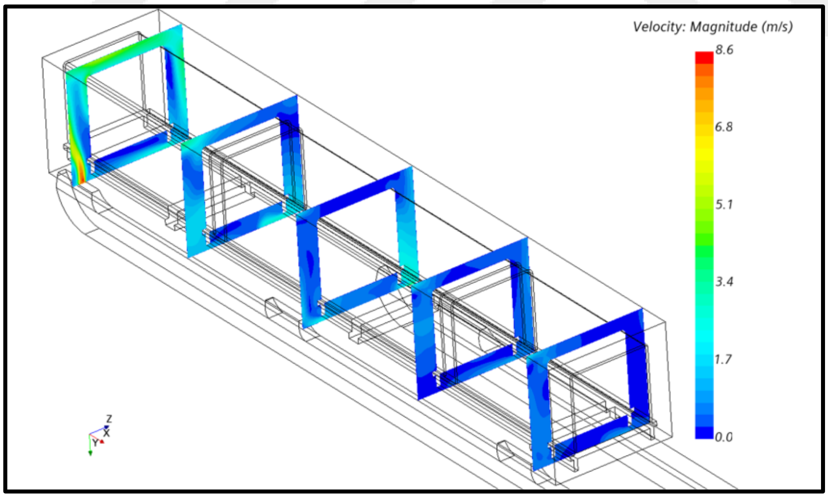

Figure 4-20. Velocity distribution of the recirculation air for the specified planes in TM2020 configuration (at t=2.5 hr)

The inhomogeneous cooling (or heat rejection) on the surface of the multi-purpose box causes the air inside to move at very low speeds. This natural convection flow in the multi-purpose box is due to the buoyancy forces arising from the temperature gradient in the air in the multi-purpose box. The flow of the air in the box is shown in Figure 4-21.

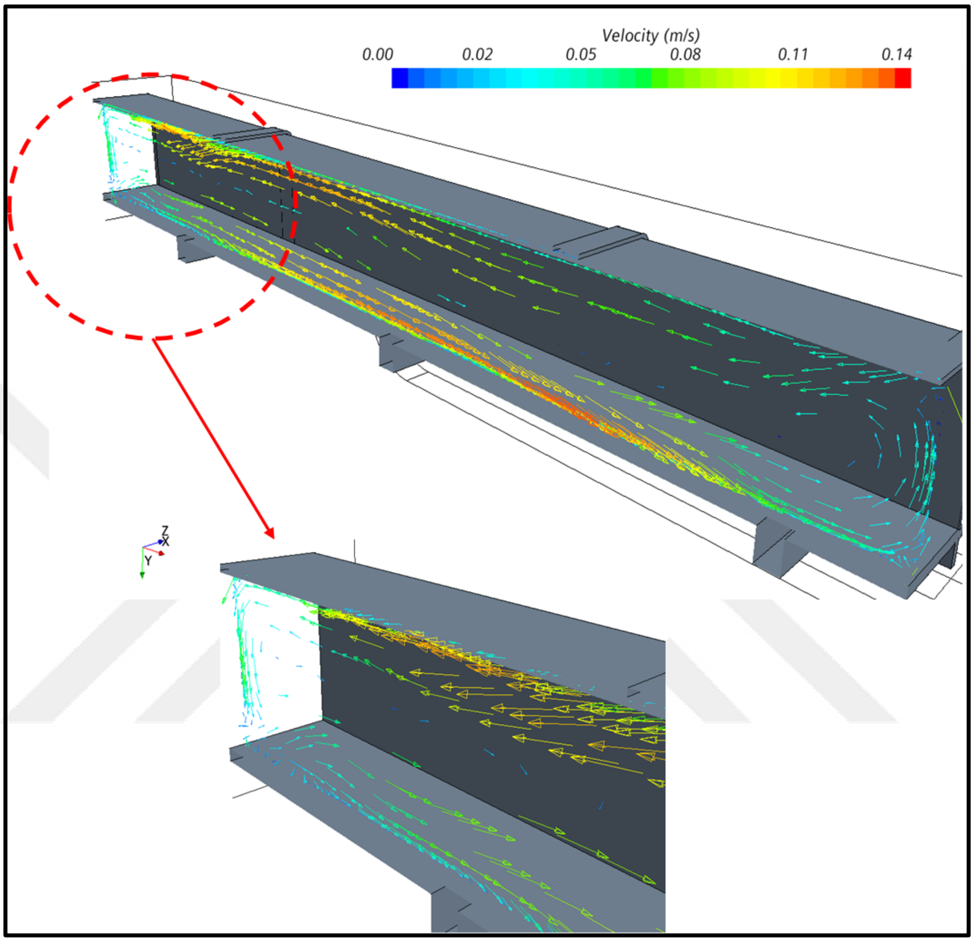

Figure 4-21. Air motion in the multi-purpose box at the end of 2.5 hours (Cross sectional view is taken from origin)

To evaluate the results with statistical point of view, the methodology given in Chapter 3 was applied. When examining the effects of the factors on the response, maximum 2-interactions of factors were taken. Pareto chart was used to decide which factor is effective for selected response value. According to the results in Table 4-7, pareto chart of the standardized effects is shown in Figure 4-22.

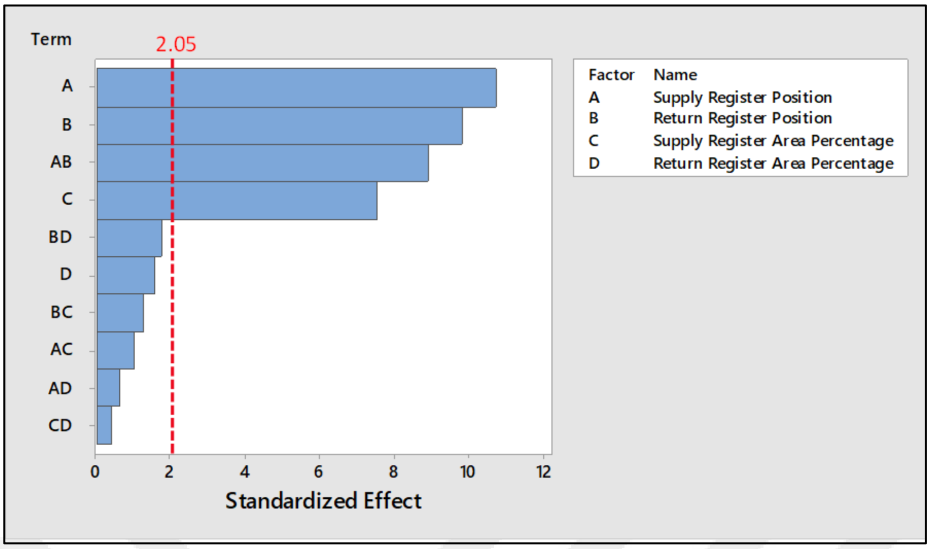

Figure 4-22. Pareto chart of the standardized effects

According to Figure 4-22, it is observed that the parameter, affecting temperature of the air in the multi-purpose box most, is the supply register position. This is followed by return register position, 2-interaction of supply register and return register position and supply register area percentage. It can be also deduced from the pareto chart that return register area percentage have no effect on the temperature of the air in the multi-purpose box. In Pareto chart, reference line is drawn at 2.05. This value and standardized effects of the factors are found by degree of freedom and confidence level [49].

To understand the significance level of the factors, p values were examined in Table 4-8. As stated before, significance level is selected as 0.05. When Table 4-8 is examined, it is observed that some values are higher than the specified significance level. To illustrate, p-value of the outlet area percentage is 0.128, which means that it is 12.8% risky to say that this factor influences the results. In another example, it is 32.4% risky to say that changing the supply register position and supply register area percentage together with other factors stay constant, has a logical effect on the response. Detailed information about p-value can be found in Chapter 3.2, page 38.

Table 4-8. P values of factors and 2-way interactions

Factors	p-value	Significance
Supply Register Position	0	Statistically Significant
Return Register Position	0	Statistically Significant
S. Register Area Percentage	0	Statistically Significant
R. Register Area Percentage	0.128	no association
2-Way Interactions	**p-value**	**Significance**
S. R. Position - R. R. Position	0	Statistically Significant
S. R. Position - S. R. Area Percentage	0.324	no association
S. R. Position - R. R. Area Percentage	0.543	no association
R.R. Position - S. R. Area Percentage	0.214	no association
R.R. Position - R. R. Area Percentage	0.095	no association
S.R. Area Percentage - R.R. Area Percentage	0.687	no association

The quantitative effect of the factors on the response is shown by main and interaction effect plots. In Figure 4-23, 4 main factors were evaluated with mean of VR values. As an example, while mean of VR value is approximately 0.79 for “Mono (M)” supply register, this value increases to 0.875 for “Dual (D)” supply register position and 0.925 for the “Triplum (T)” supply register position

It must be noted that main effects may not be decisive to explain the effects of factors on the response. Therefore, evaluation should be made together with interaction plots. Interaction plots are presented in Figure 4-24.

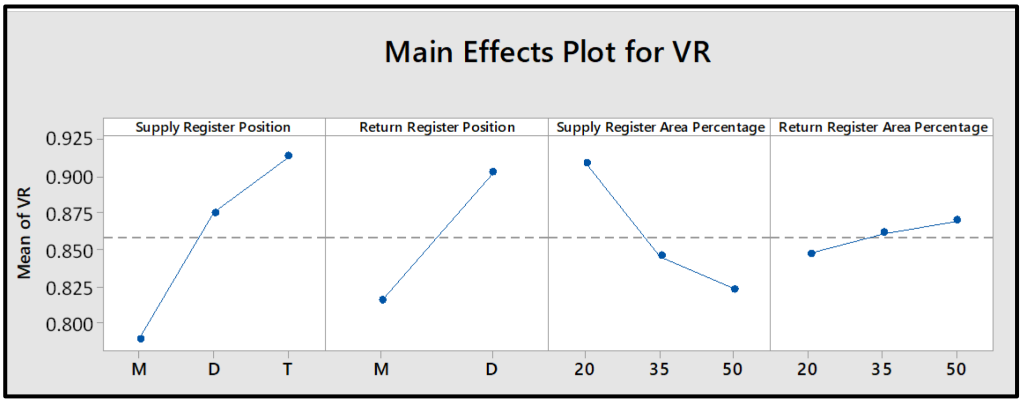

Figure 4-23. Main effects plots

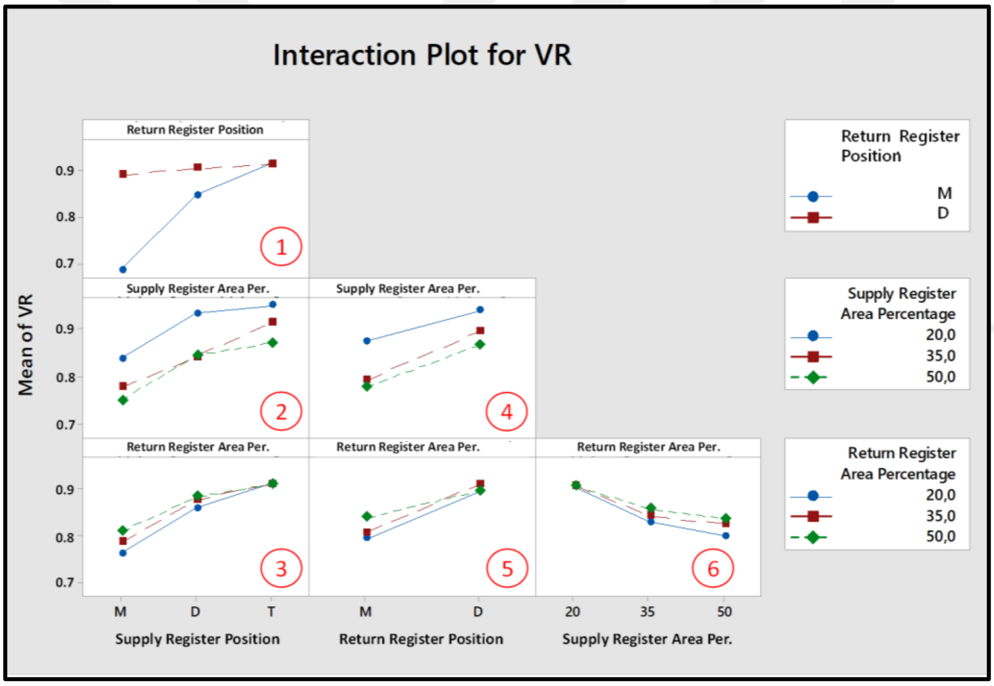

Figure 4-24. Interaction plots for VR

The following comments can be made according to Figure 4-24.

- When supply register position is selected “M” or “D”, it is observed that the “D” return register position gives better results than “M” return register position. In other words, more of the air in the multi-purpose box has reached the target temperature (15˚C), or below. In addition, when supply and register position is selected as "T" and "M", respectively, VR value increases again. (Graph 1)

- Using 20% supply register area percentage for each supply register position indicated that more air in the multi-purpose box has reached its target temperature. It is also interpreted that "T" supply register position gives better results than other supply register positions. (Graph 2)
- When supply register position and return register area percentage are considered together, it seems that "T" supply register position gives better results, however return register percentage area does not affect the VR values. (Graph 3)
- When return register position and supply register area percentage are examined together, "D" return register position is better than "M" return register position, and 20% supply register area is the best choice for VR values (Graph 4). However, it must be noted from Graph 1 that for "T" supply register position, "M" return register position gives high VR values, too.
- It is observed in Graph 5 that return register area percentage does not change VR values. In other words, the amount of the air in the multi-purpose box, cooled to the target temperature, does not change according to different return register area percentage values.
- When supply register area increases, VR value decreases according to Graph 6.

To determine how well the model fits data given in Table 4-7, "R-sq" and "S" values were calculated in Minitab. According to the results, R-sq and S are 93.8% and 0.03, respectively. This shows that the model highly fits the data.

4.5 Conclusions of the Chapter

To understand how supply register position, return register position, supply register area percentage and return register area percentage affect the temperature distribution of the multi-purpose box and the air inside, 54 different CFD analyses were conducted. According to the results of these analyses, the following outputs are obtained.

- The pressure loss between inlet and outlet for the configurations were close to each other and low due to low air velocity in the chamber. While the highest-pressure loss is obtained as 159 Pa, the lowest one is 114 Pa. These values are negligible compared to the pressure drop in the ducting that is not the scope of this thesis. Because of these reasons, pressure loss was not considered as a response value to examine effects of the factors.
- According to the numerical results, outlet temperatures for all configurations at the end of 2.5 hours, are very close to each other. In other words, minimum outlet temperature at the end of 2.5 hours is 8.7˚C, and maximum outlet temperature is 9.4˚C for examined configurations. Since the values are so close to each other, it does not make the statistical evaluation very properly. So that, outlet temperature was not taken as a response to compare effectiveness of factors.
- As a result of the analyses, when regions of the air in the multi-purpose box, reaching the target temperature, were examined, the values in Table 4-7 were obtained. According to the table, while the air in the multi-purpose box reached the target temperature, or below at a rate of 98% in TM2020 configuration, this rate was calculated as 60% in MM5020 configuration at the end of 2.5 hours.
- According to Figure 4-22, Figure 4-23 and Figure 4-24, it has been observed that the factor affecting the VR value the most is the supply register position. In addition to this, it was observed that return register area percentage did not influence the VR value.
- Although the air in the multi-purpose box mostly reaches the target temperature, it has been observed that some regions of it for TM2020 configuration did not reach the target temperature, as shown in Figure 4-16.

CHAPTER 5

EXPERIMENTAL STUDIES

5.1 Introduction

In this section, selection of the equipment in the AC Unit and the experimental studies are explained in detail. The experimental setup is designed to represent the physical model of the multi-purpose box with the outer chamber, inlet-outlet channel, supply and return registers and related with CFD configurations. The purpose of these studies is to experimentally validate CFD analyses results, explained in Chapter 4. In the experimental setup, K-type thermocouples were used to measure temperatures, and in-channel averaged pitot tube pressure sensors were used to measure static and dynamic pressure in the inlet channel. Detailed information about the sensors is given in Chapter 3.3.

5.2 Configuration of the AC Unit

As mentioned, volume of the AC unit on the mobile platform is limited. For this reason, the equipment was selected according to this constraint. Some other constraints on the placement of the AC unit within itself were also discussed. These are given as follows:

- The evaporator is located in front of the blower.
- Placing the condenser fans facing the space outside the unit. In other words, there should be no obstacles in front of the condenser fans.
- Blower and compressor were positioned vertically.

Some parts of the AC unit and their features are given in Table 5-1. It should be noted that studies were carried out on the placement of the AC unit and it was used as a ready-made product that gives air at 1500 m^3/hr volumetric flow rate and 5˚C temperature.

Table 5-1. Features of the equipment in the AC unit

Equipment	Features	Value	Unit
Compressor	Power Input	10.5	kW
	Evaporator Capacity	11.76	kW
	Condenser Capacity	21.3	kW
	Mass Flow	601	kg/hr
	Weight	240	kg
	Dimensions	796 x 440 x 500	mm
Blower Fan (Snail Type)	Power Input	9.5	kW
	Volumetric Flow Rate (@5 kPa)	1500	m^3/hr
	Weight	100	kg
	Dimensions	830 x 730 x 650	mm
Condenser Fan	Power Input	1.3	kW
	Max. Back Pressure	200	Pa
	Weight	16	kg
	Dimensions	ϕ700 x 250	mm
Condenser	Type	Micro Channel	-
	Weight	7	kg
	Dimensions	890 x 600 x 22	mm
Evaporator	Pressure Drop (@1500 m^3/hr)	100	Pa
	Weight	68	kg
	Dimensions	740 x 750 x 350	mm
Expansion Valve	Max. Working Pressure	28	bar
	Weight	2	kg
	Dimensions	120 x 80 x 110	mm

5.3 Experimental Setup and Configurations

During the experimental studies, supply registers in the experimental setup and mechanical interfaces at the bottom of the chamber were changed for the configurations to be tested. The configurations tested in the first place are listed in Table 5-2. The 3D model of the experimental setup is shown in Figure 5-1 and Figure 5-2. Moreover, view of the experimental setup is shown in **Error! Reference source not found.**. It must be noted that these figures are illustrated for TM2020 configuration.

Table 5-2. List of the configurations that will be carried out for experimental studies

#	**Configurations**
1	TM2020
2	MM2020
3	DM2020
4	TM3520
5	TM5020

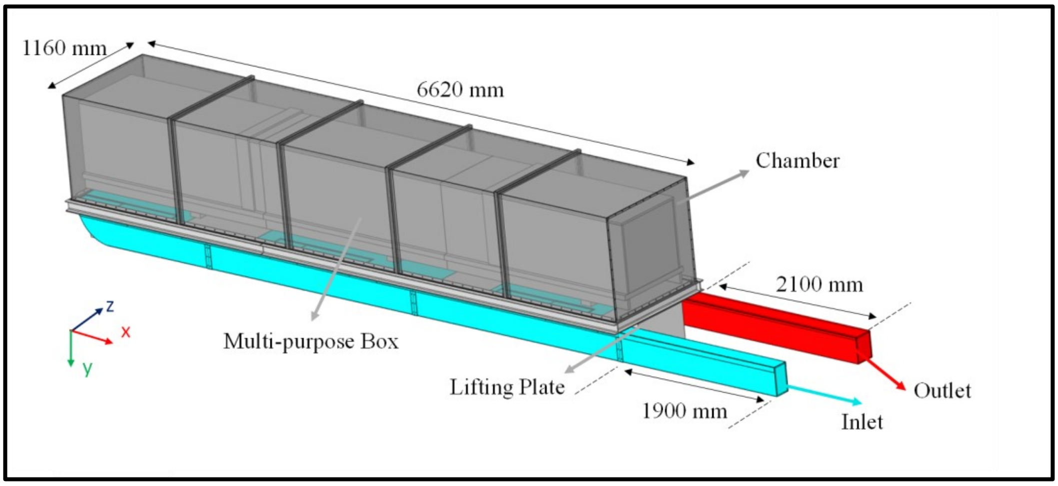

Figure 5-1. 3D model of the experimental setup (multi-purpose box with outer chamber and inlet and outlet channels)

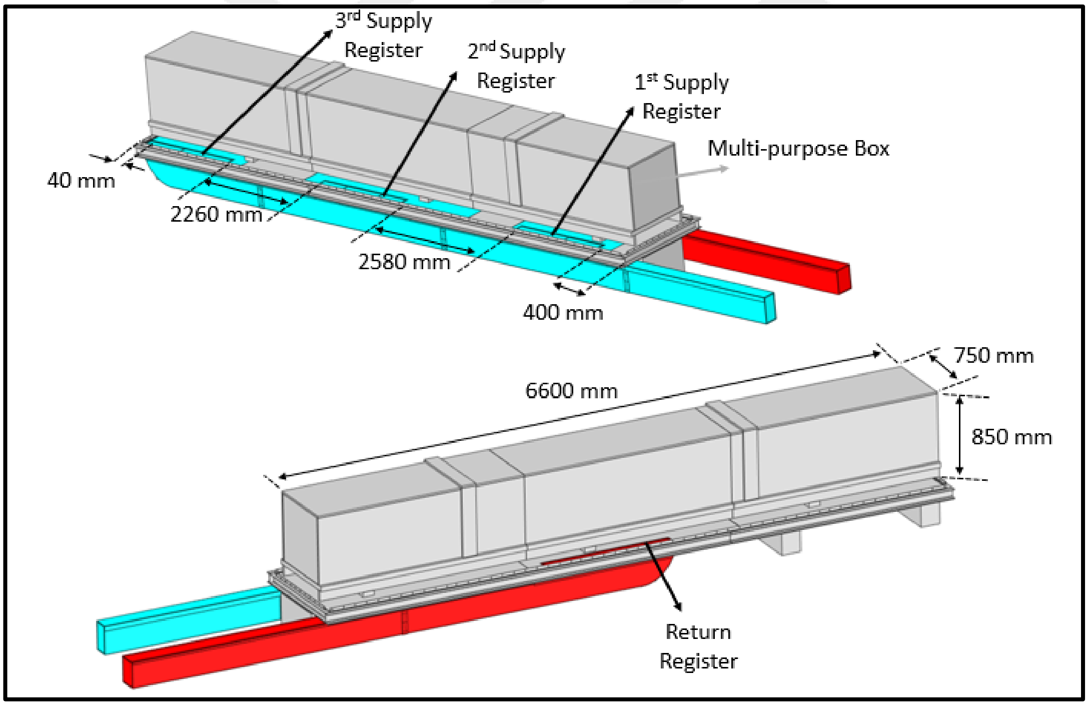

Figure 5-2. 3D model of the experimental setup (multi-purpose box with outer chamber and inlet and outlet channels for TM2020 configuration)

The positions of the thermocouples, placed in the experimental setup and the temperature recording points in CFD models, are compatible with each other. For easier understanding, thermocouple locations and their naming are shown in Figure 5-3 and Figure 5-4, respectively.

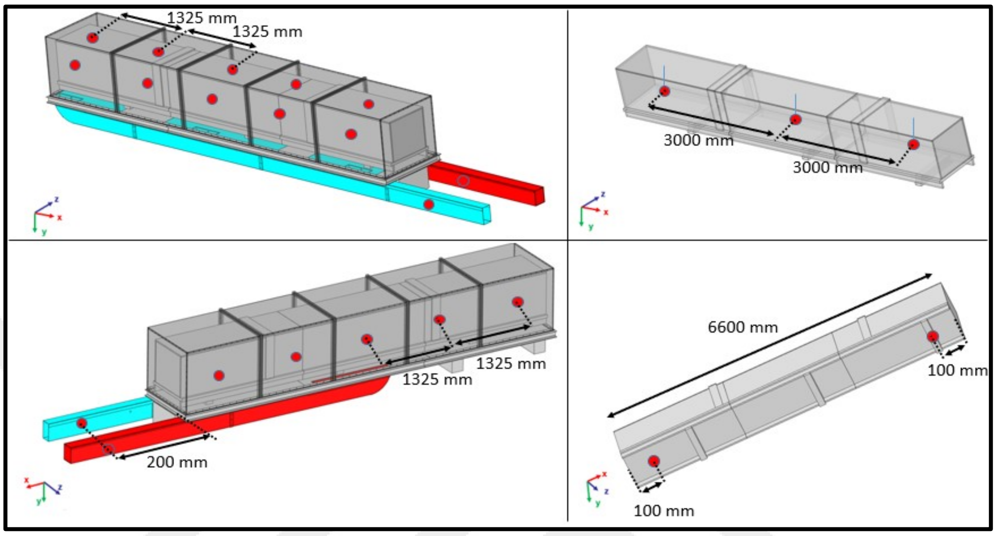

Figure 5-3. Positions of the thermocouples

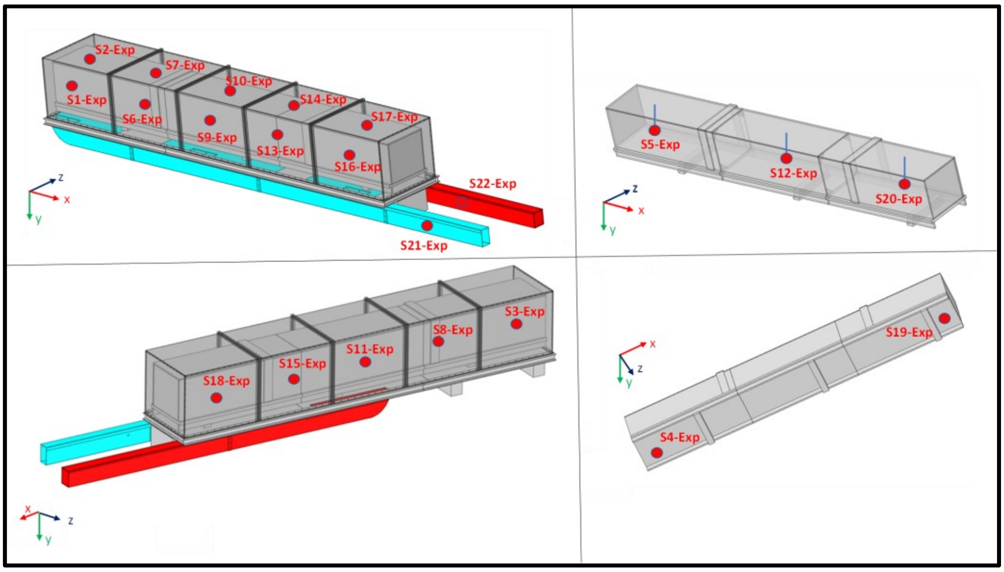

Figure 5-4. Naming for the thermocouples

To calculate volumetric flow rates of the recirculation air, passing through each supply register, velocity values were measured from 3 different points in the inlet duct. Positions of the in-channel averaged pitot tube pressure sensors are shown in Figure 5-5.

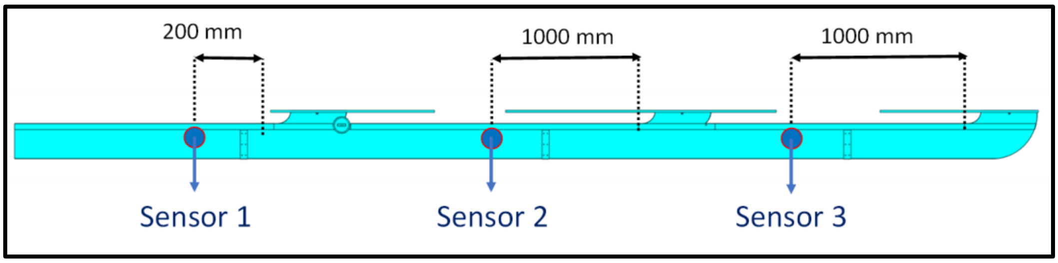

Figure 5-5. Positions of the in-channel averaged pitot tube pressure sensors

Two assumptions, valid only for ideal conditions, were made in the numerical analyses. These are 5˚C constant temperature inlet boundary condition and adiabatic wall Neumann boundary condition for the recirculation air domain.

In AC units, operating with the principle of the vapour compression refrigeration cycle, the air passing through the evaporator is not expected to give air at a constant temperature from the first moment it is started [50]. The main reasons are given below.

- When the AC unit is started, the air coming from the indoor environment (it is inside of the chamber for this case) is at ambient temperature and this temperature is gradually reduced.
- The blowing temperature corresponding to inlet temperature boundary condition for CFD models changes. As the ambient temperature increases, the amount of heat released from refrigerant decreases at the condenser region, which also reduces the cooling capacity [51].

For these reasons, inlet temperature was obtained as in Figure 5-6 by the trial test. As it is shown in the figure, the inlet temperature is at the temperature in the chamber after the experimental procedure, or preconditioning is completed. It decreased from

38˚C to approximately 8˚C within about 10 minutes. Inlet temperature reached the regime in about half an hour, and it was about 5˚C. There is also some fluctuation in the inlet temperature due to condenser suction temperature (i.e., ambient temperature).

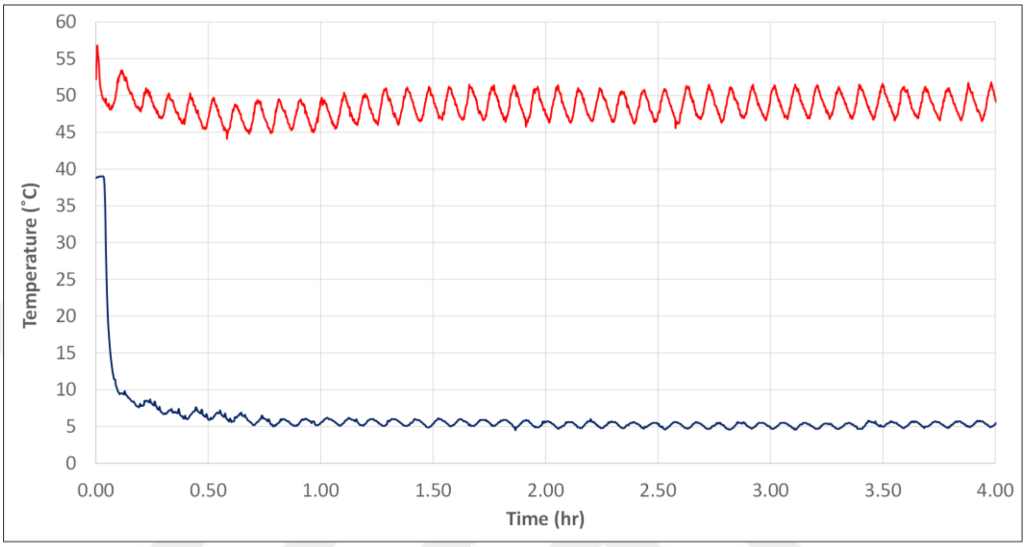

Figure 5-6. Inlet temperature and condenser suction temperature for TM2020 configuration

The chamber is well insulated, so that the adiabatic wall boundary condition assumption is valid as much as possible. However, to control, or check this assumption, 4 additional thermocouples were placed in two different regions, the upper surface of the chamber and the inner surface of the insulation material in the trial test. The location of the thermocouples is shown in Figure 5-7. It must be noted that every red point represents the two thermocouples.

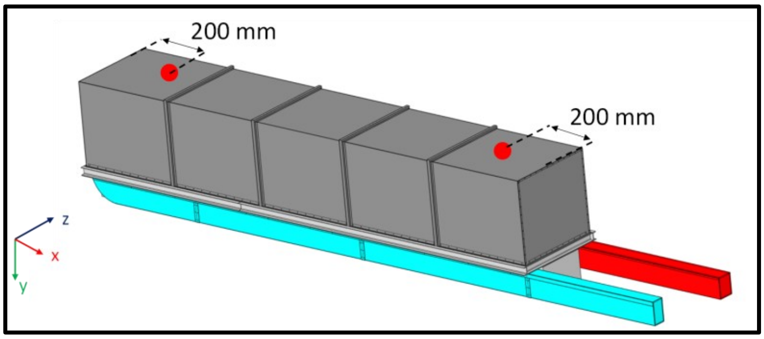

Figure 5-7. Location of the thermocouples on chamber outer surface and insulation inner surface

Time-dependent temperatures are shown in Figure 5-8. According to the results, at both ends of the chamber, temperatures are very close to each other, and the chamber is mostly homogeneously conditioned in the control room. Moreover, temperatures on the inner surface of the insulation reached an average of 23˚C after about 35 minutes and remained constant.

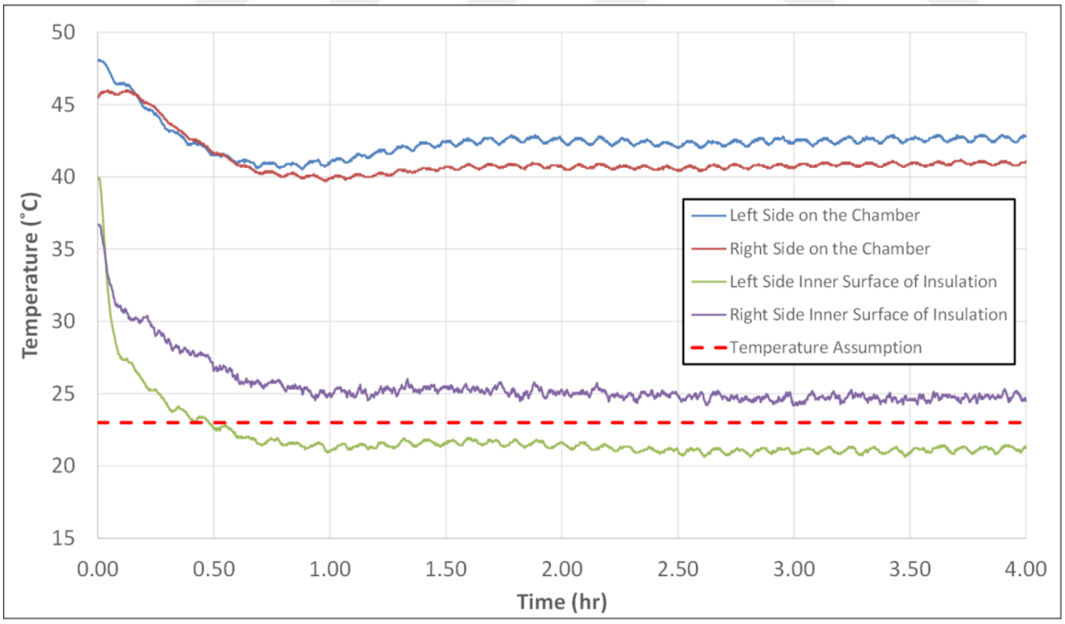

Figure 5-8. Time-dependent temperatures on the chamber surface and insulation inner surface

Another conclusion to be drawn from the figure is that since the insulation surface is 23˚C, it causes heat gain inside of the chamber. Thus, adiabatic wall boundary condition applied to the recirculation air region is not valid. As a result, 23˚C constant temperature wall boundary condition was applied to the recirculation air to take into account the heat gain from the control room into the chamber in the validation studies.

According to Figure 5-6, Figure 5-8 and considerations about initial temperature of the multi-purpose box, mentioned in Chapter 4, the initial and boundary conditions of the CFD models that will be validated by experimental results are rearranged as follows and shown in Figure 5-9.

- Due to experimental procedure applied to bring the multi-purpose box and the air inside to the initial temperature (or higher than the initial temperature) before experimental studies, initial temperature of the multi-purpose box and the air inside are increased from 25˚C to 26.5˚C. The reason is that the temperature values of them were not homogeneously distributed after the experimental procedure has been applied. When the temperature distribution on the multi-purpose box and the air inside was examined, it was observed that an average 26.5˚C was obtained.
- Constant 5˚C temperature inlet boundary condition was changed with time-dependent variable inlet boundary condition shown in Figure 5-6.
- Adiabatic wall boundary condition for the recirculation air region was changed with constant 23˚C temperature wall boundary condition.

Initial Temperature	25˚C
Wall Boundary Condition	Adiabatic
Inlet Boundary Condition	5˚C

→

Initial Temperature	26.5˚C
Wall Boundary Condition	23˚C
Inlet Boundary Condition	Variable

Figure 5-9. Rearranged initial and boundary conditions for validation CFD models with experimental results

5.4 Validation of "TM2020" CFD Model with Experimental Results

Experimental results of TM2020 configuration are shown in Figure 5-10. These results include temperature values on the side and the top surface of the multi-purpose box, bottom of the multi-purpose box and the air inside. (See Figure 5-3, Figure 5-4 and Appendix C for the location of the thermocouples.)

The data from each thermocouple is separately shown in Figure 5-12 through Figure 5-31 for a better understanding of the experimental results and comparison with the CFD results. In these figures, "S#-CFD" shows the results of the CFD analysis with dashed lines and with the rearranged assumptions (the table on the right in Figure 5-9). "S#-Exp" shows the experimental results of the temperatures with respect to time. The uncertainty in the temperature measurement is ±0.4˚C [41,42]. "S#-U+" and "S#-U-" shows the upper and lower uncertainty values of the thermocouples due to measurement accuracies, respectively.

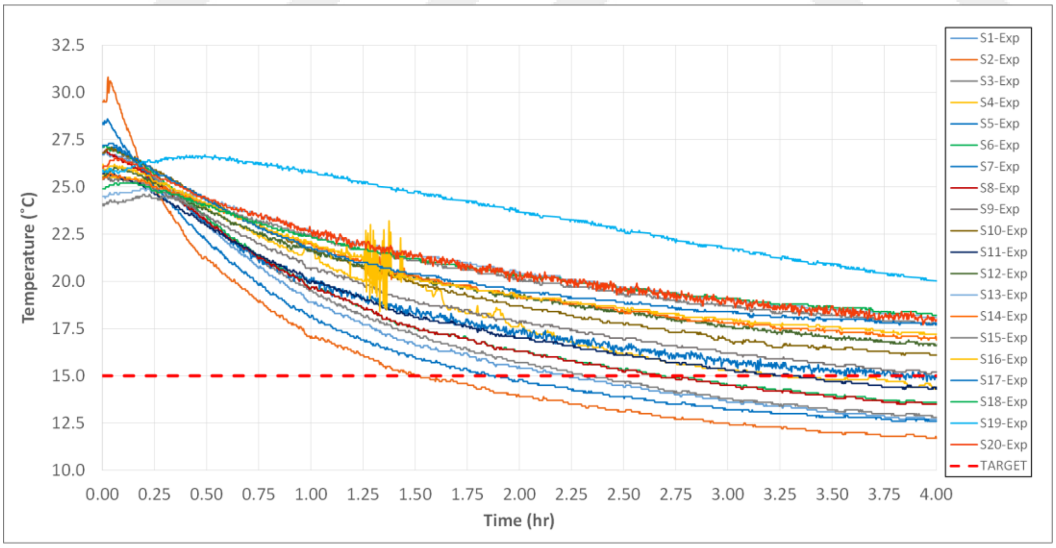

Figure 5-10. Experimental results for TM2020 configuration

According to the Figure 5-10, when the experimental procedure, or preconditioning is completed (designated as t=0), it is observed that the temperatures are not homogeneously distributed at t=0 due to preconditioning at the beginning. Since the design objective is conditioning the multi-purpose box from 25˚C to 15˚C, the actual t=0 is determined as the time when temperatures are approximately 25˚C, which occurs at approximately 0.24 hour later. Therefore, the graph, experimental and CFD results, is shifted 0.24 hour to left and the rearranged graph is shown in Figure 5-11.

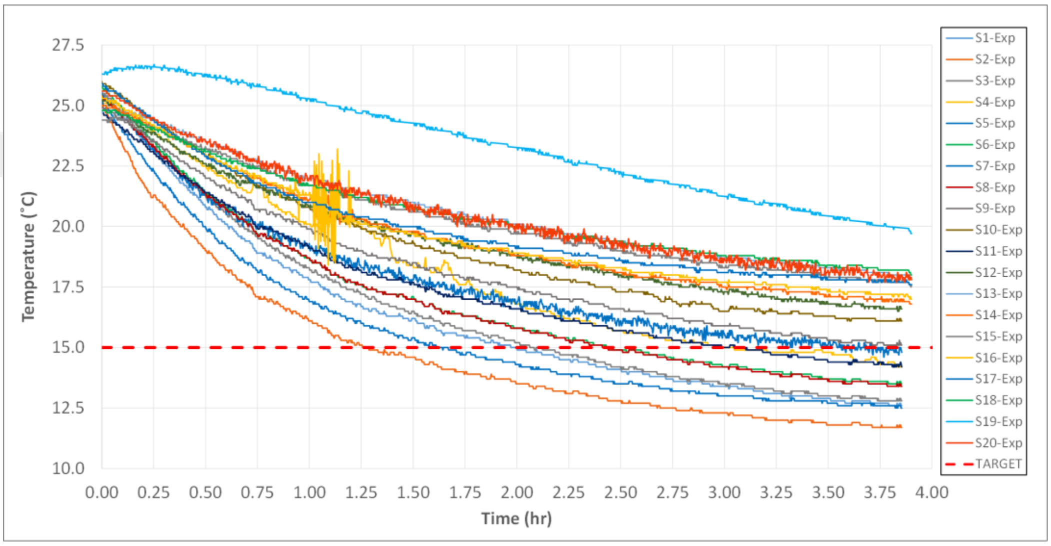

Figure 5-11. Rearranged experimental results for TM2020 configuration

<u>Thermocouples on the Side and Top Surfaces of the Multi-Purpose Box</u>

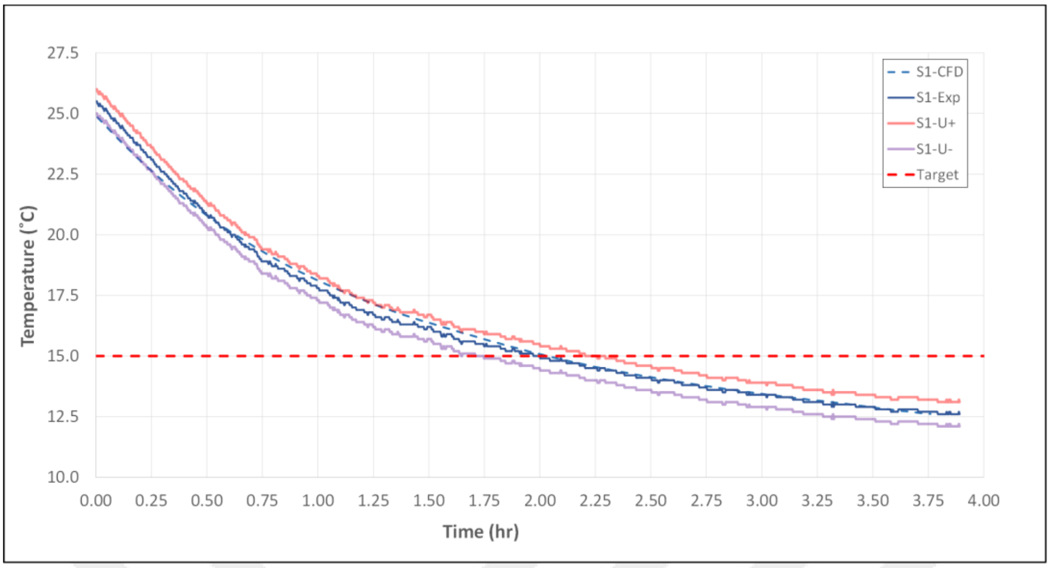

Figure 5-12. Results for S1

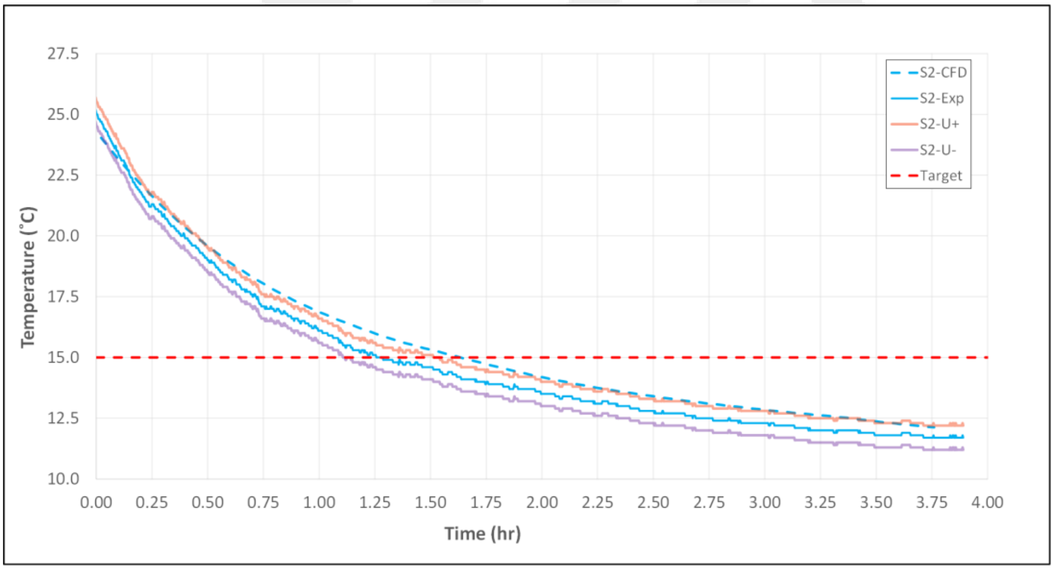

Figure 5-13. Results for S2

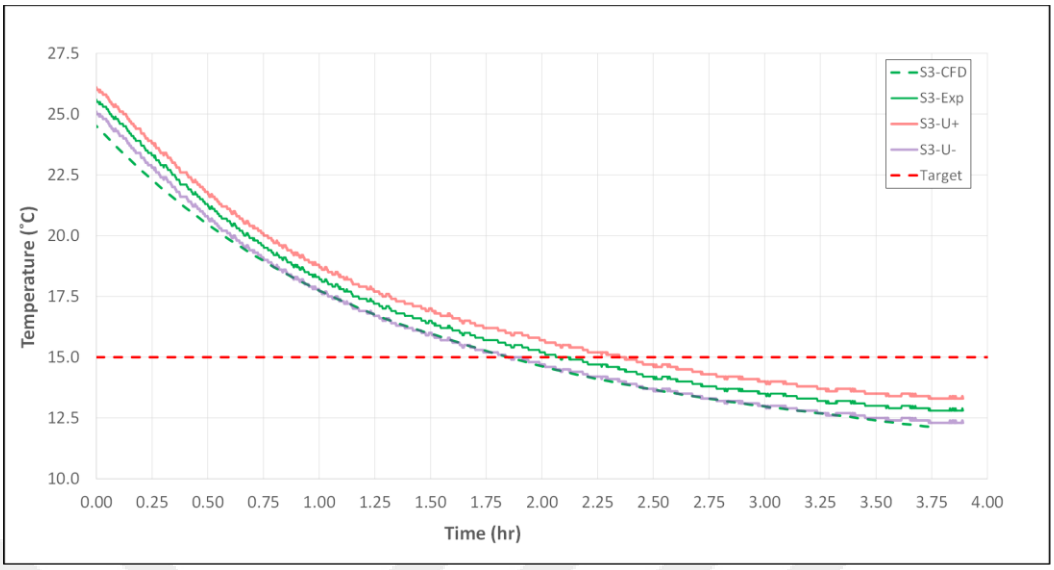

Figure 5-14. Results for S3

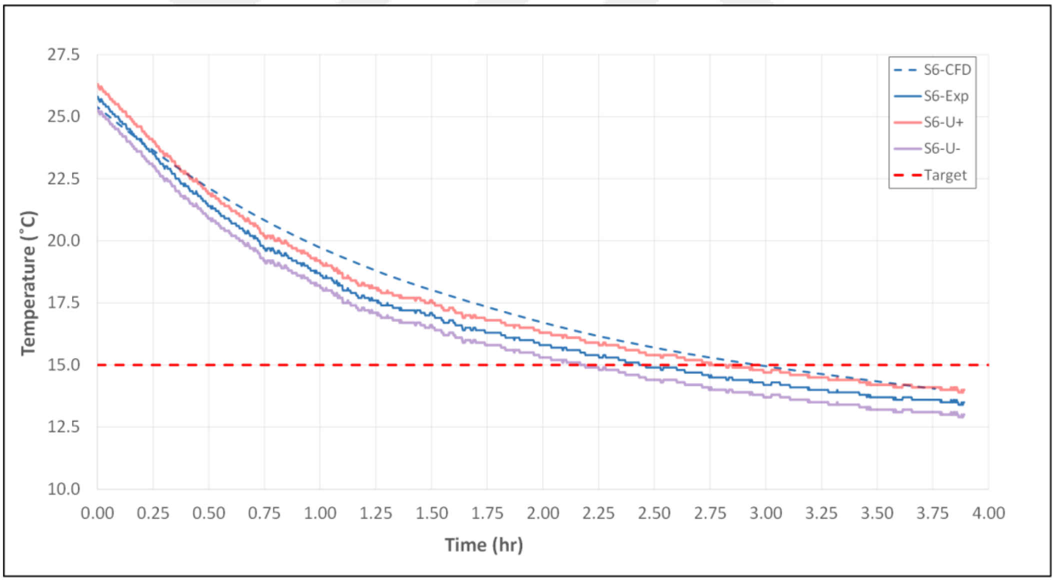

Figure 5-15. Results for S6

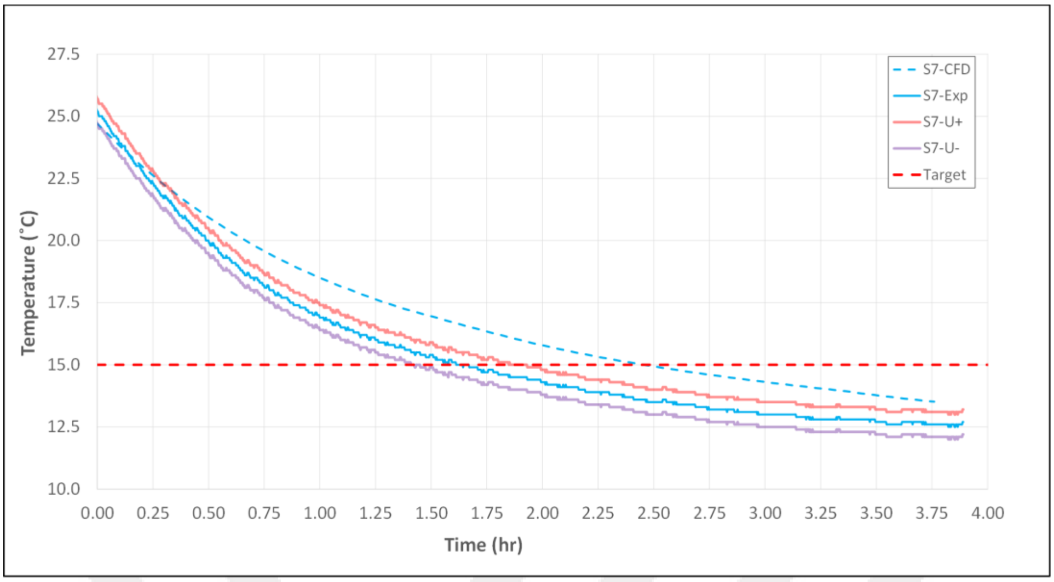

Figure 5-16. Results for S7

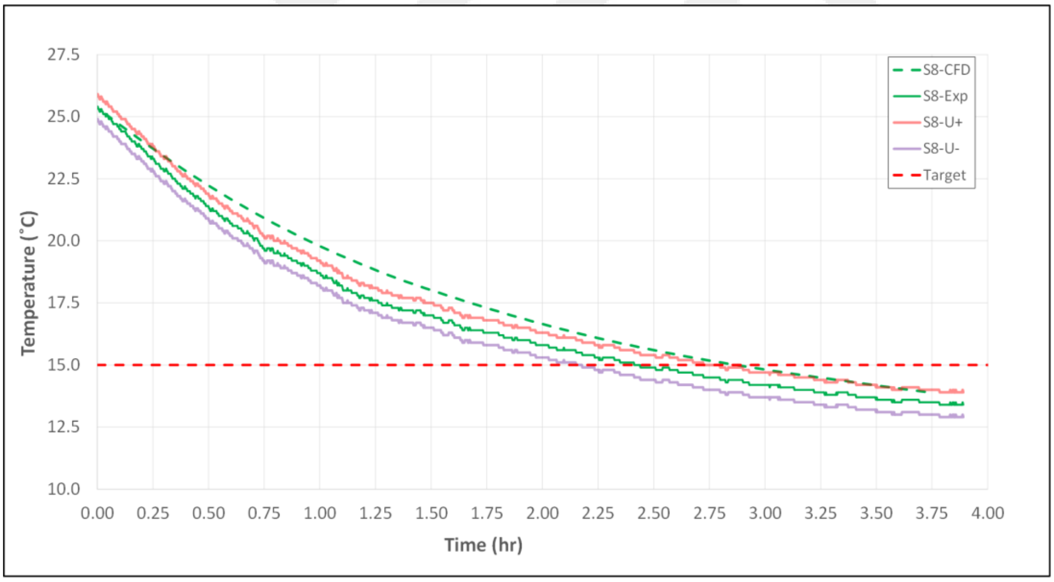

Figure 5-17. Results for S8

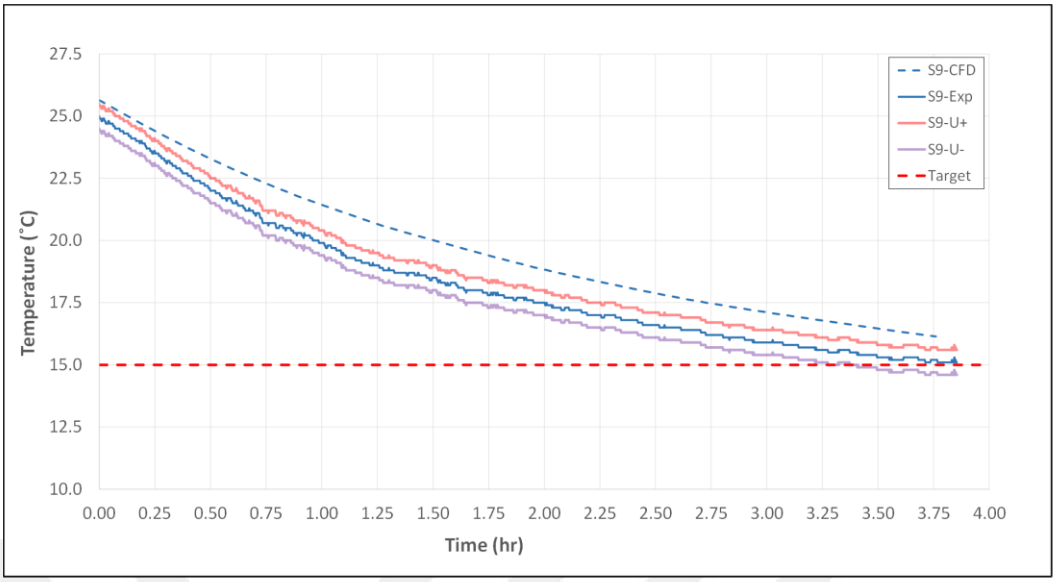

Figure 5-18. Results for S9

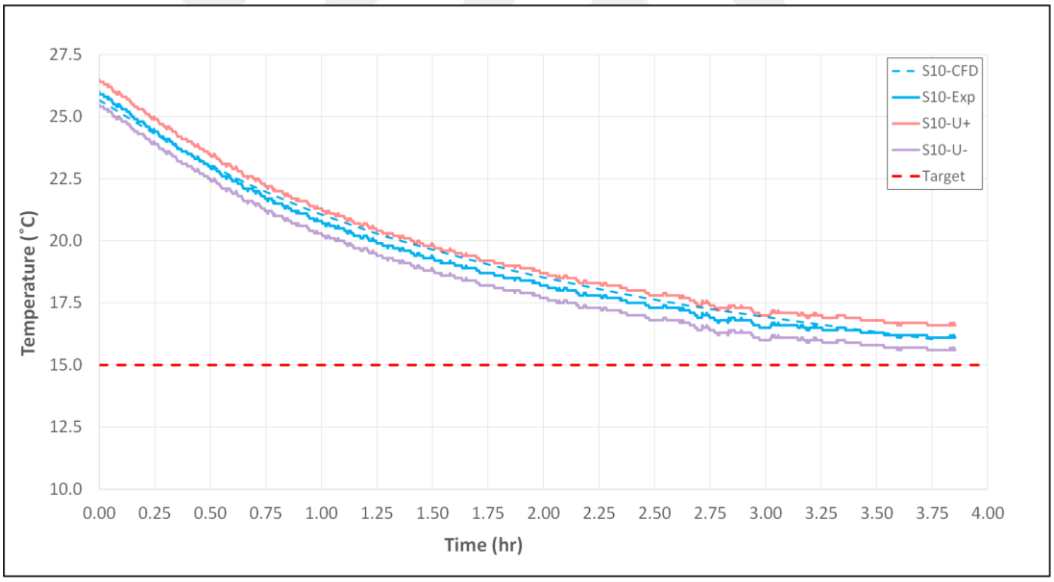

Figure 5-19. Results for S10

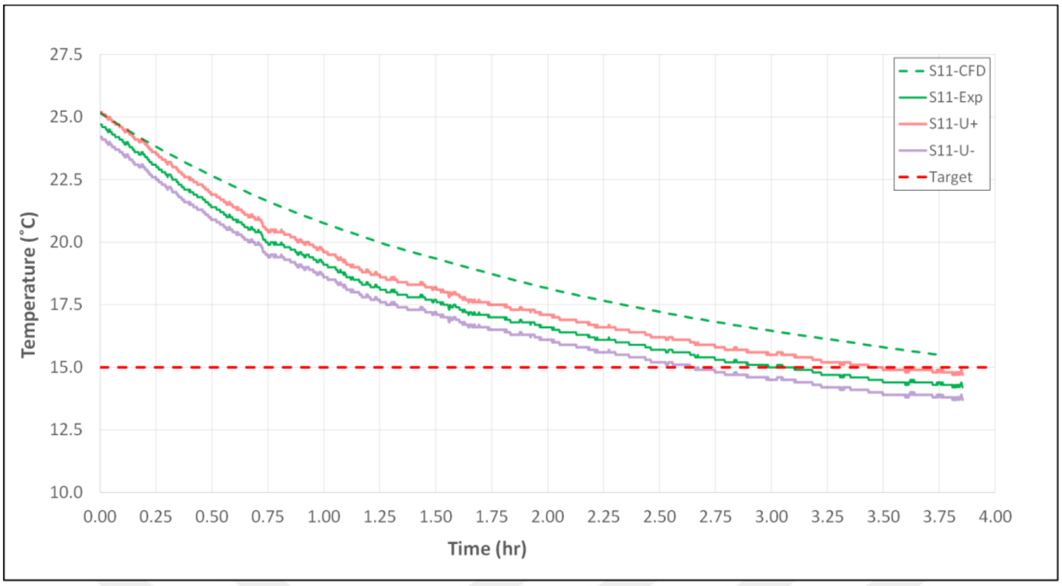

Figure 5-20. Results for S11

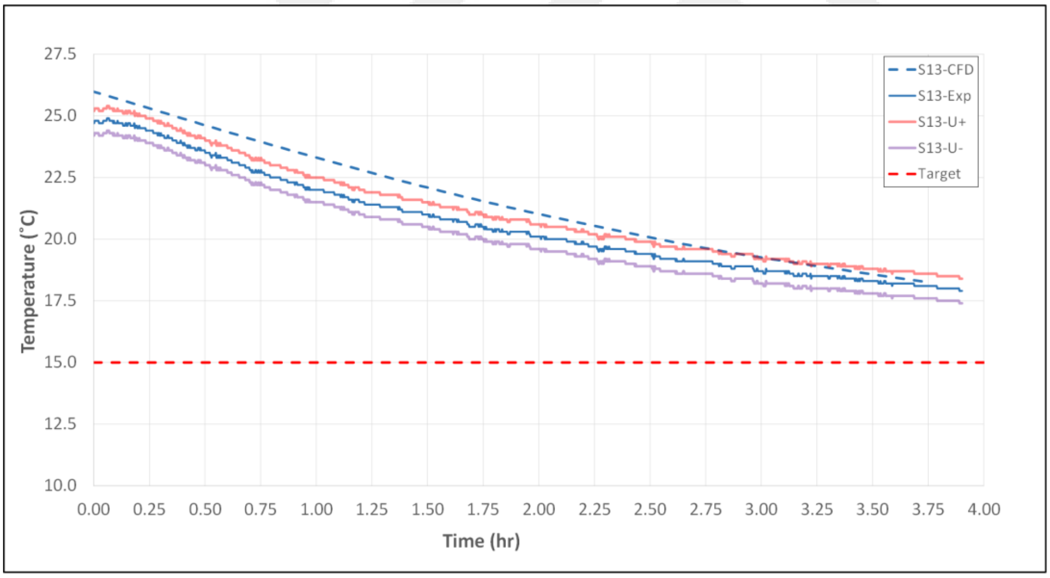

Figure 5-21. Results for S13

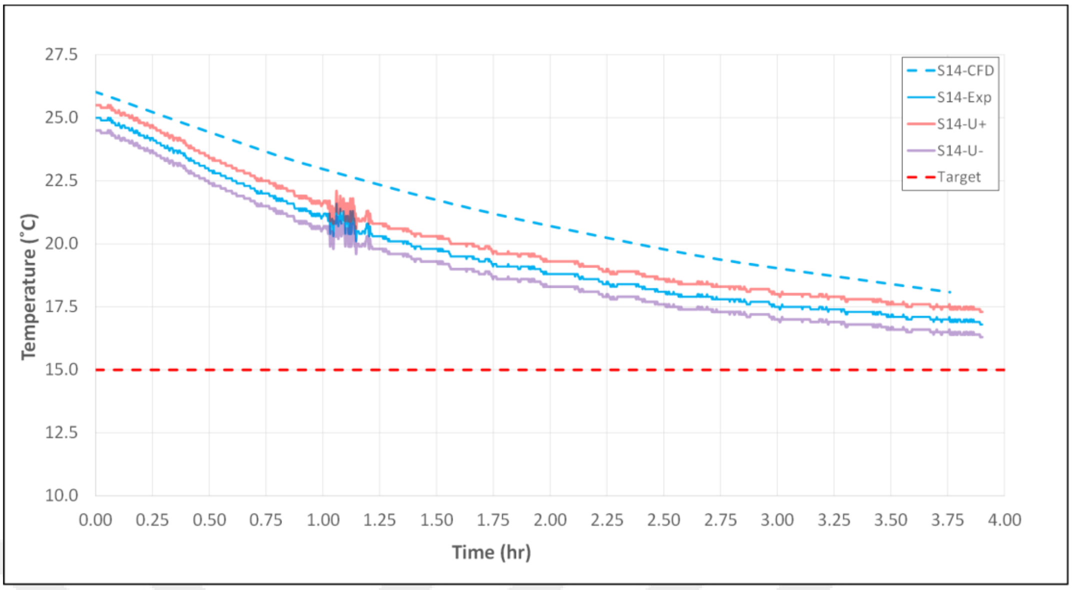

Figure 5-22. Results for S14

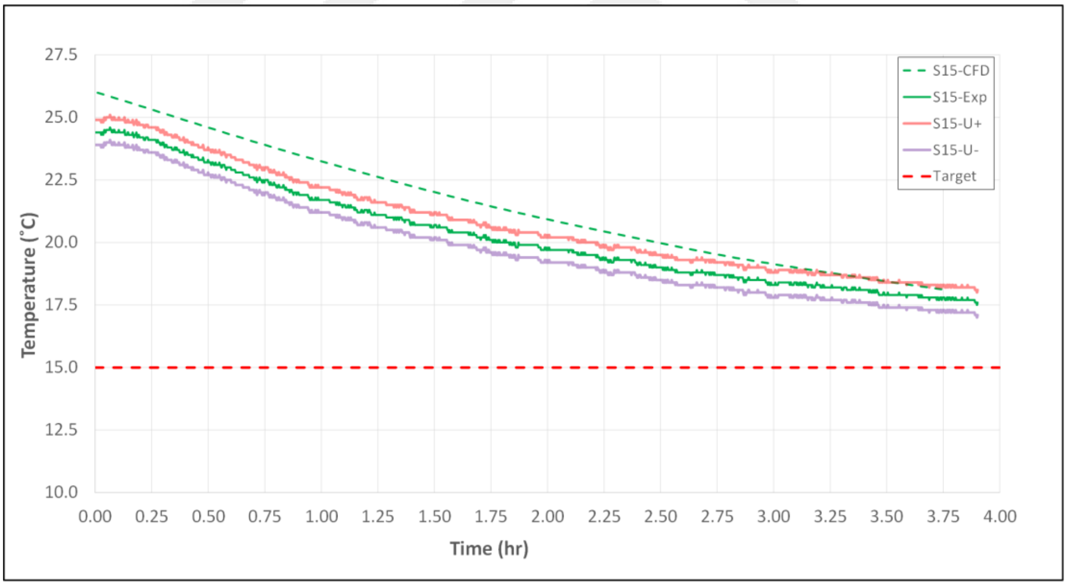

Figure 5-23. Results for S15

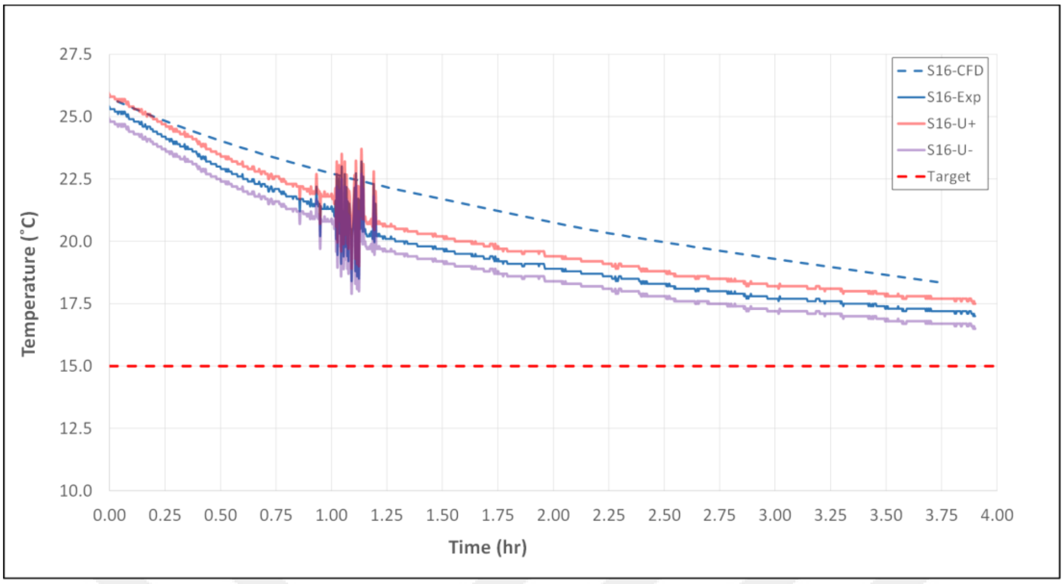

Figure 5-24. Results for S16

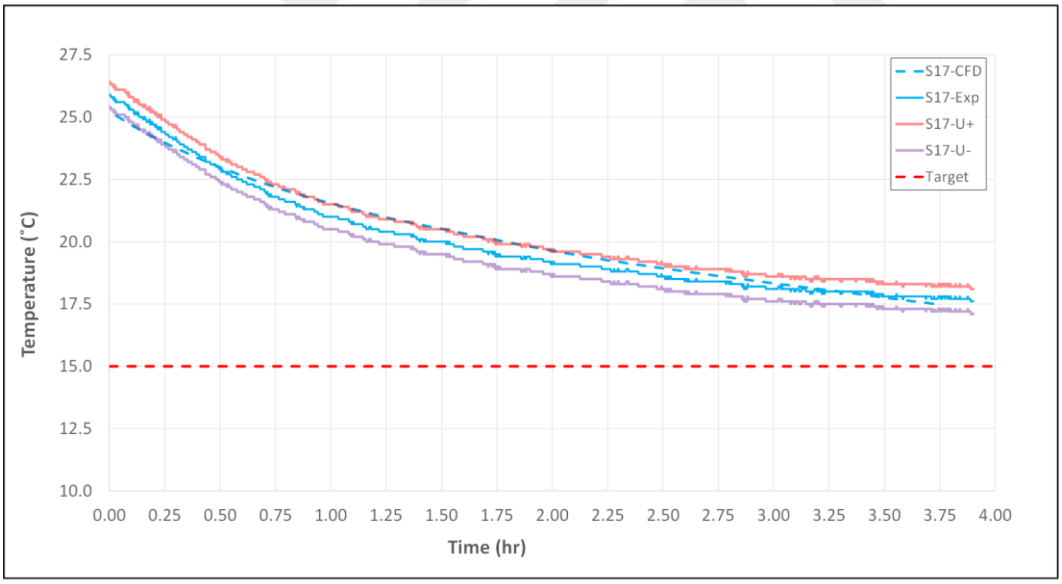

Figure 5-25. Results for S17

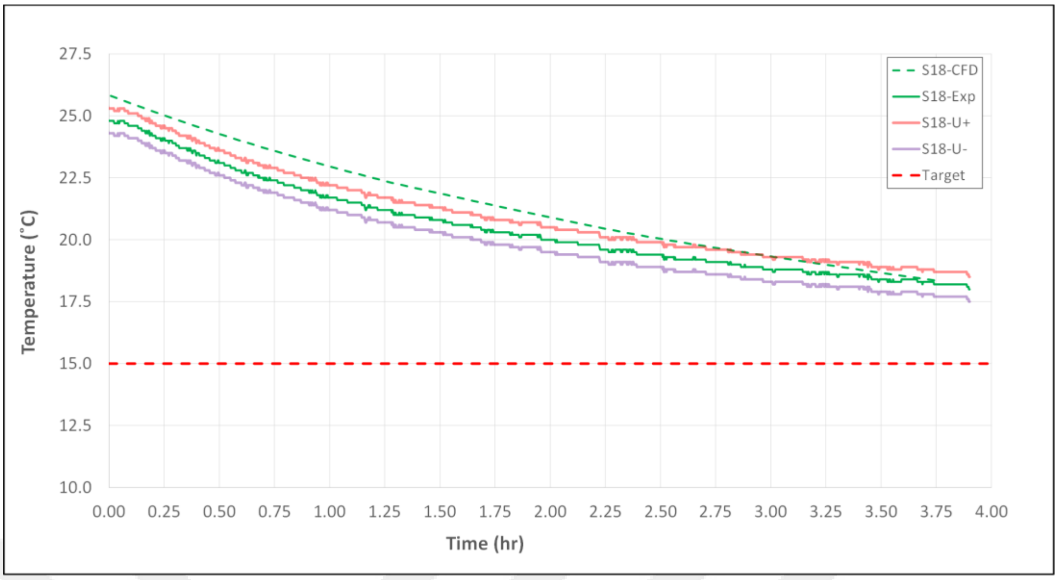

Figure 5-26. Results for S18

<u>Thermocouples on the Bottom Surface of the Multi-Purpose Box</u>

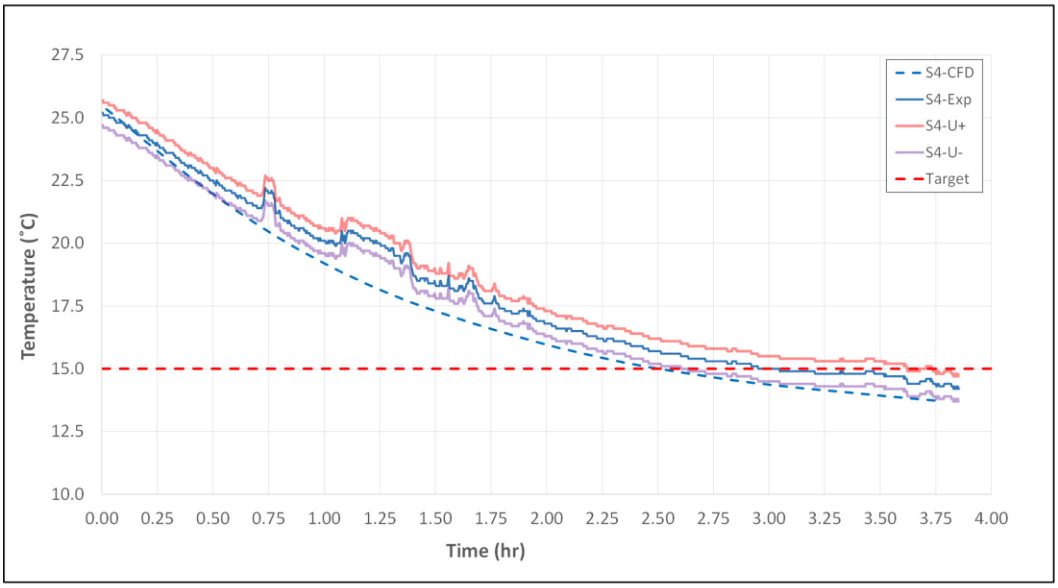

Figure 5-27. Results for S4

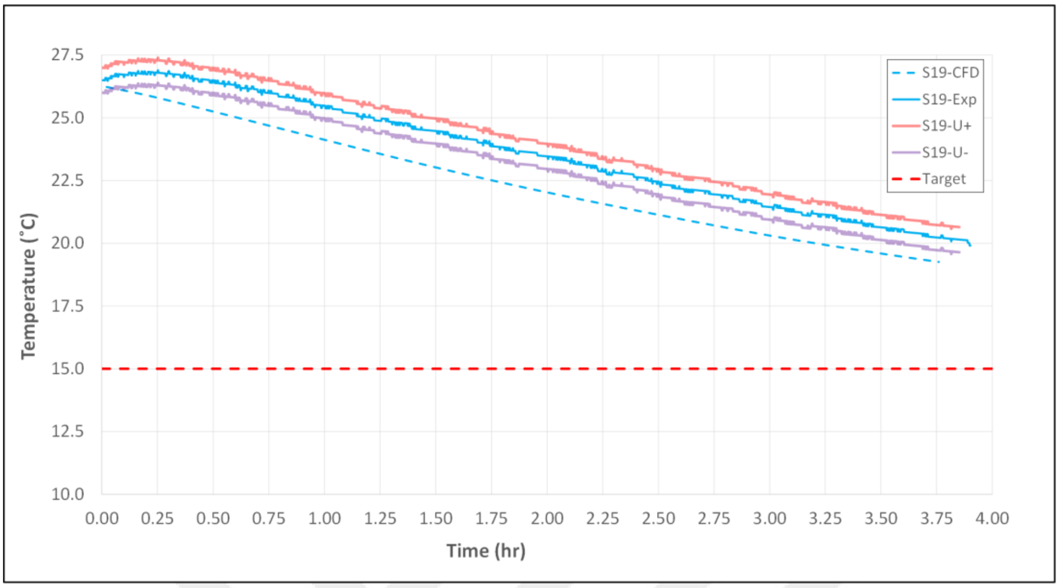

Figure 5-28. Results for S19

Thermocouples in the Air in the Multi-purpose Box

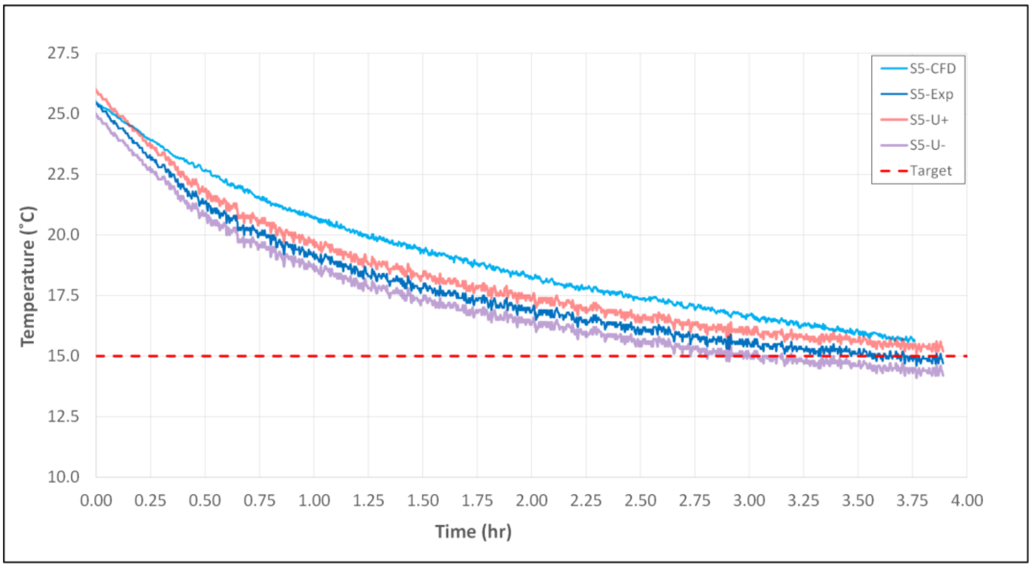

Figure 5-29. Results for S5

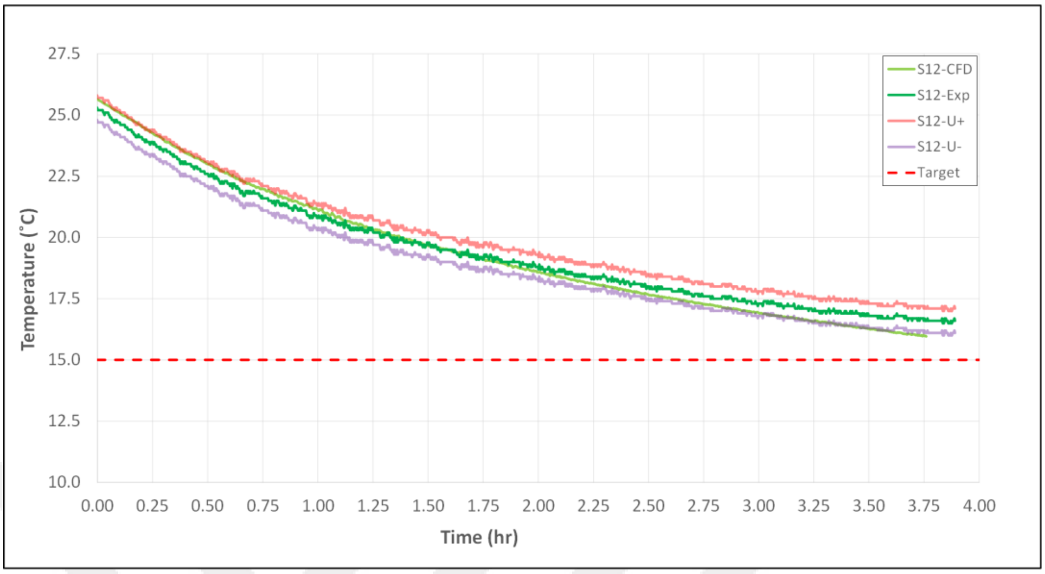

Figure 5-30. Results for S12

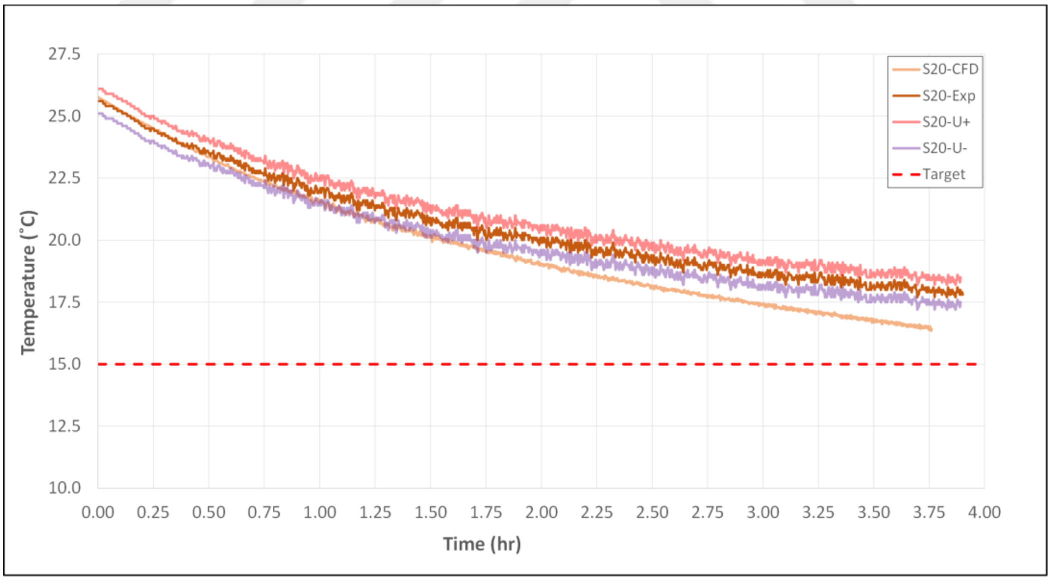

Figure 5-31. Results for S20

To interpret the results in this section more clearly, the multi-purpose box is divided into regions as shown in Figure 5-32. The results obtained in the studies, carried out in Chapter 5, are summarized below.

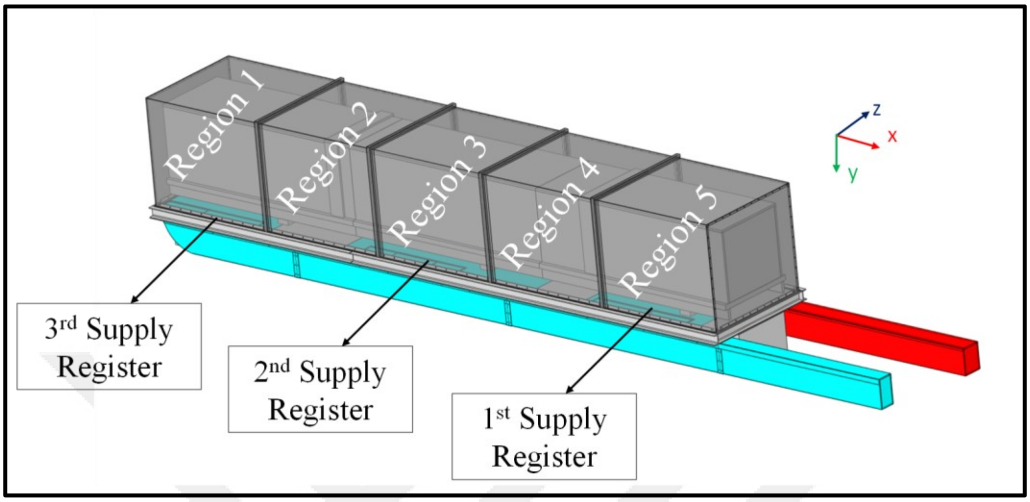

Figure 5-32. Regions of the multi-purpose box

According to Figure 5-12 through Figure 5-31, results of CFD analysis have been validated with experimental results with high accuracy.

It was observed that the temperatures in the 4th and 5th regions did not reach the target temperature within 4 hours. Especially, the highest temperature is measured at region 5 and at the bottom of the multi-purpose box. It is approximately 20˚C at the end of 4 hours. The reason is that the recirculation air passing through the first supply register is less when it is compared with other supply registers because of the momentum of recirculation air in the inlet channel. Due to low volumetric flow rate at this section, the amount of heat rejection from bottom of the multi-purpose box was very low. When the temperature of the air in the multi-purpose box is examined, it is observed that S20 is about 2.5˚C higher than the target temperature. The same reason about volumetric flow rates, mentioned before, was also valid indirectly for this thermocouple, or region.

When temperatures on the surface of the multi-purpose box and in the air inside are examined in Figure 5-10, an increase in temperatures is observed in the first 15 minutes. The source of this increase is that inlet temperature (shown in Figure 5-6), which is in the range of 40˚C-10˚C in this time period.

When the experimental results were examined, it was observed that there was noise in some thermocouples, especially in S16-Exp. This is due to the irregularities of the electrical network of the control room where the experimental setup is located.

Comparison of the experimental and numerical results of the volumetric flow rates of the recirculation air passing through each supply register is given in Table 5-3. The uncertainty of the in-channel averaged pitot tube pressure sensor, used to measure the volumetric flow rates for each supply register, is 2% [43].

Table 5-3. The experimental and numerical results of the recirculation air passing through each supply register

Experimental Results			Numerical Results		Relative True Error (%)
Measured Average Velocity (m/s)	**Measured Volumetric Flow Rate (VFR) (m^3/hr)**	**VFR (%)**	**Calculated VFR (m^3/hr)**	**VFR (%)**	
Sensor 1 11.0	1st S. Register 262.63±5.2	17.50	213.30	14.22	18.8
Sensor 2 9.1	2nd S. Register 530.71±10.6	35.36	545.80	36.39	2.8
Sensor 3 5.2	3rd S. Register 707.62±14.1	47.14	740.85	49.39	4.7

When the amount of the recirculation air passing through the supply registers is examined, it is observed that the most of it passes through the 3rd supply register.

According to Table 5-3, when numerical results of the recirculation air passing through the supply registers are compared with the experimental results, relative true error percentages in the 1st, 2nd and 3rd supply registers were calculated as 18.8%, 2.8% and 4.7%, respectively. Although relative true error for the 1st supply register is high, it did not have a drastic effect on the temperatures at corresponding region of the multi-purpose box, because the recirculation air flow passing through the 1st supply register is approximately 1/6 of the total air flow in the inlet channel. The reason is that the recirculation air bypasses the 1st supply register due to the momentum it has in the inlet channel.

5.5 Effect of Supply Register Position on Temperatures

To examine the effect of supply register position on temperatures, experiment number 1, 2 and 3, given in Table 5-2, have been carried out. Experimental results of TM2020, DM2020 and MM2020 configurations are shown in Figure 5-33, Figure 5-34 and Figure 5-35, respectively.

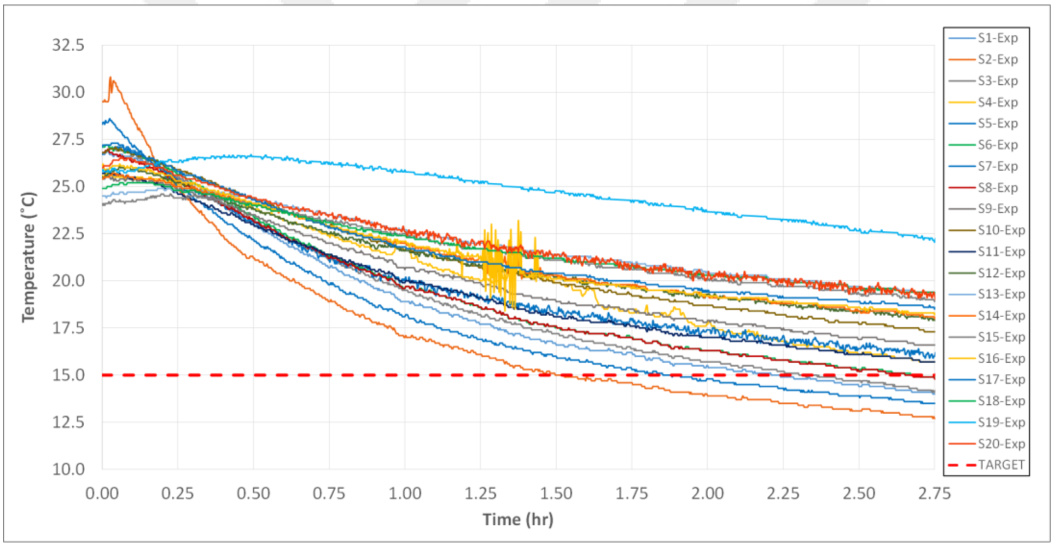

Figure 5-33. Experimental Results for TM2020 Configuration

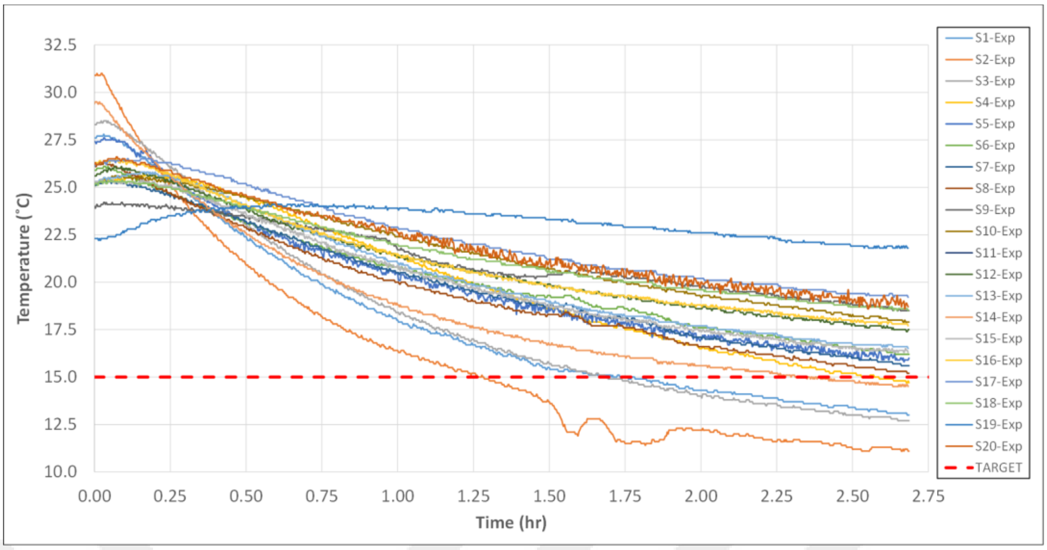

Figure 5-34. Experimental Results for DM2020 Configuration

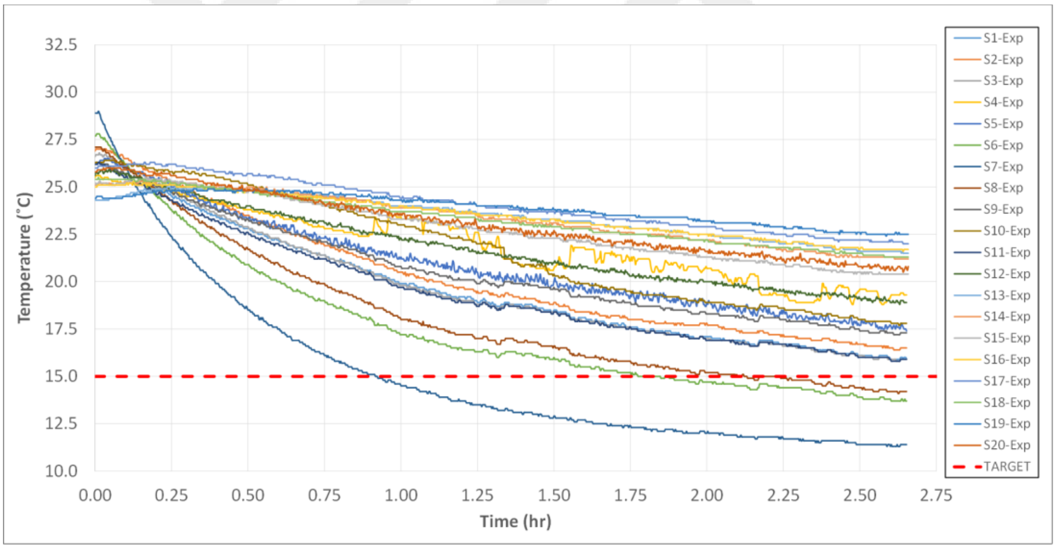

Figure 5-35. Experimental Results for MM2020 Configuration

When the results were examined, it was observed that the temperature values in TM2020 configuration were more homogeneously distributed than other configurations after approximately 2.75 hours. In addition, the region reaching the target temperature in MM2020 configuration is less than the ones in other two configurations.

The temperature distribution of DM2020 and TM2020 configuration is close to each other. However, especially in DM2020 configuration, although S19 measured temperature as 23.5˚C initially, no decrease in this temperature was observed at the end of 2.75 hours. The main reason for this phenomenon is the low air flow rates at the bottom of multi-purpose box and small amount of heat rejection from the bottom surface.

5.6 Effect of Supply Register Area Percentage on Temperatures

To examine the effect of the supply register area percentage on temperatures, experiment number 1, 4 and 5, given in Table 5-2, have been carried out. Experimental results of TM2020, TM3520 and TM5020 configurations are shown in Figure 5-36, Figure 5-37 and Figure 5-38, respectively. It must be noted that experimental results of TM2020 configuration is presented again in this section for easier evaluation.

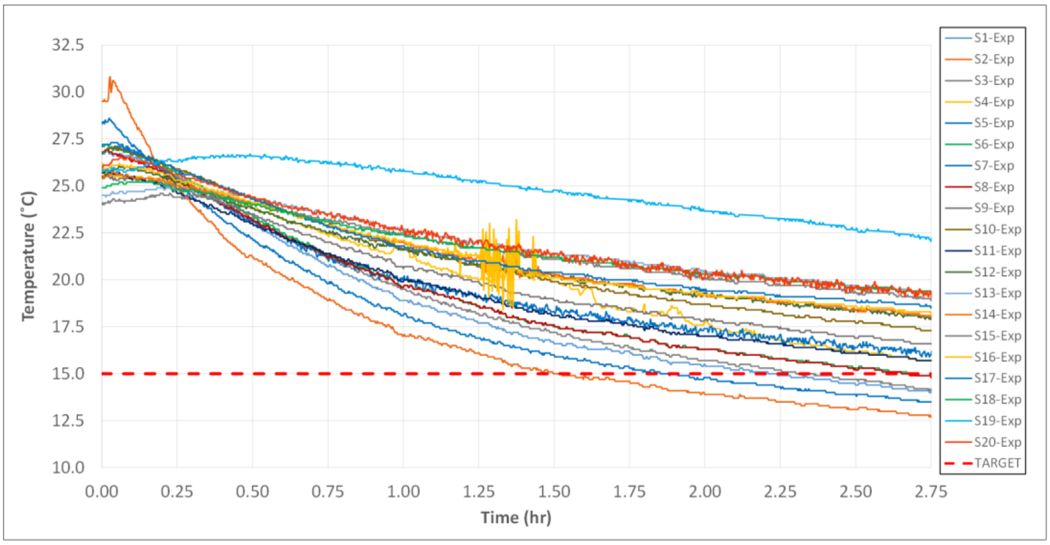

Figure 5-36. Experimental Results for TM2020 Configuration

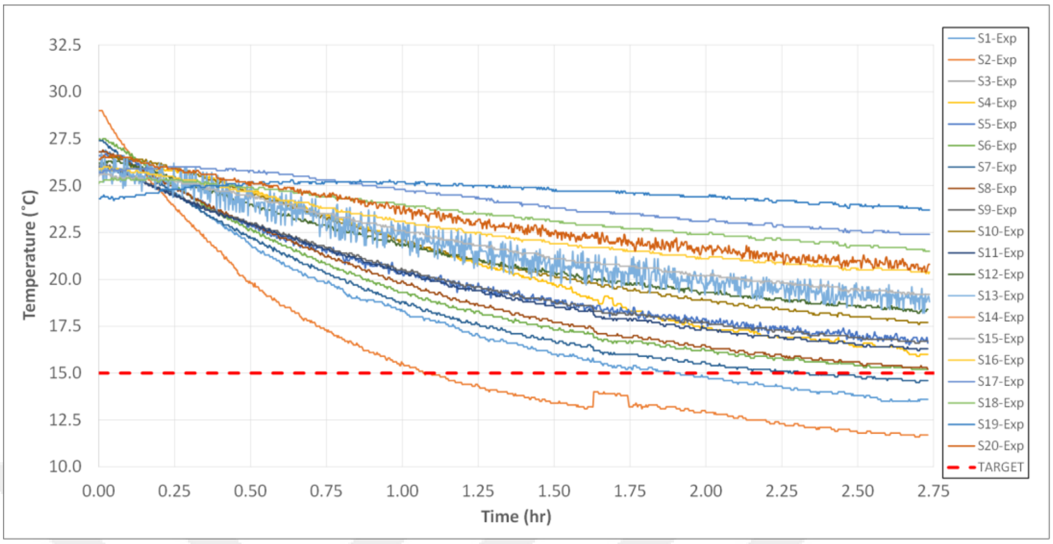

Figure 5-37. Experimental Results for TM3520 Configuration

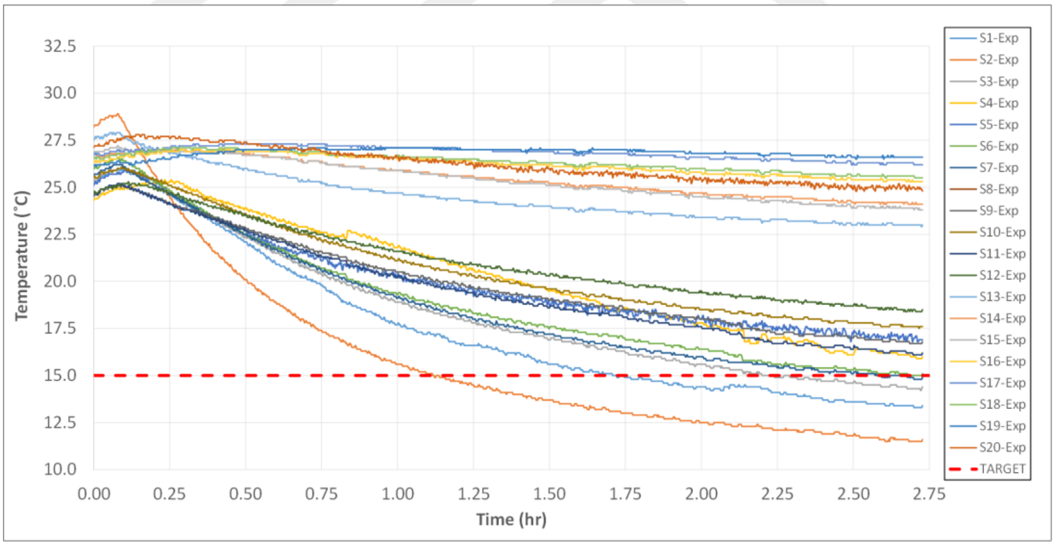

Figure 5-38. Experimental Results for TM5020 Configuration

When the results were examined, it was observed that the increase in the supply register area percentage negatively affected the temperature distribution on the surface of the multi-purpose box and the air inside at the end of 2.75 hours. The most homogeneous temperature distribution in the examined time interval was observed in the TM2020 configuration. In other words, homogeneous temperature distribution has not been achieved with increasing supply register area percentage. In TM5020 configuration, it was observed that temperatures did not decrease in some regions on the multi-purpose box. The main reason for this situation is that recirculation air did not reach the 4th and 5th regions due to low momentum of recirculation air in the regions, as mentioned and expected from the CFD analyses.

5.7 Conclusions of the Chapter

In this chapter, experiments have been set up for the configurations shown in Table 5-2, and they have been completed. For validation studies, results of TM2020 configuration were presented and validated with experimental results. According to Figure 5-12 through Figure 5-31, results of CFD analyses have been validated with experimental results with high accuracy. Furthermore, the experiments were also conducted to understand the effect of supply register position and supply register area percentage on temperatures. According to the first results, more homogeneous temperature distribution was obtained by increasing supply register position from "Mono" to "Triplum", when other factors remained constant. It is also shown that more region of the multi-purpose box has reached target temperature in TM2020 configuration. In addition to this, by increasing supply register area percentage while other factors are constant, the homogeneous temperature distribution was not achieved, and the temperatures moved away from the target temperature at the end of 2.75 hours. These results are compatible with the statistical evaluations.

As a result, it was observed that the temperatures, measured by the thermocouples in the 4th and 5th regions could not reach the target temperature in TM2020 configuration at the end of approximately 4 hours. The highest temperature was measured at the bottom of the multi-purpose box and in the 5th region. Here is also the region where airflow rate is the least. For this reason, it was decided to design a baffle in the 1st supply register, and effect of it was examined in Chapter 6.

CHAPTER 6

ENHANCEMENTS IN COOLING WITH BAFFLE DESIGN

6.1 Introduction

According to the results in Chapter 5, temperature values of the multi-purpose box in the 4th and 5th regions did not reach the target temperature. The main reason is that volumetric flow rate of the recirculation air, passing through the first supply register, which corresponds to specified regions, is less when it is compared with other supply registers.

In this chapter, studies were carried out to increase volumetric flow rate of the recirculation air passing through the first supply register for TM2020 configuration. For this purpose, a baffle, or a router, was placed in the 1st supply register. The 3D model of the baffle is given in Figure 6-1.

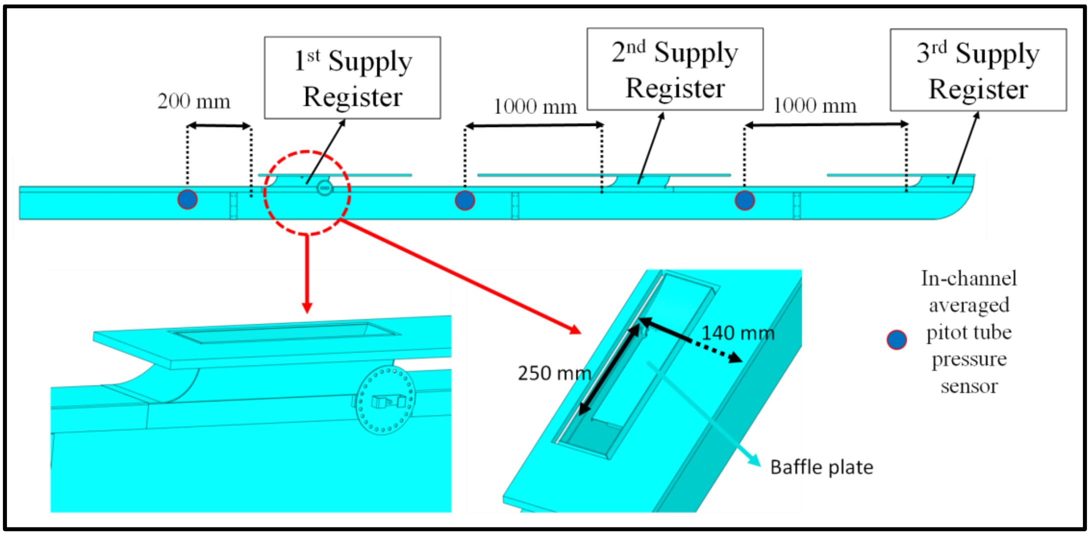

Figure 6-1. 3D CAD model of the baffle

Two factors were examined to optimize the length and angle of the baffle. For both factors, 3 levels were examined. Angle values are 10˚, 25˚ and 45˚. The length values are 125 mm, 250 mm and 375 mm. In the case where the baffle angle is 45˚ and the length is 375 mm, almost all the recirculation air passes through the 1st supply register. As an example, the schematic view of the 250 mm length baffle with different angles is given in Figure 6-2 as an example.

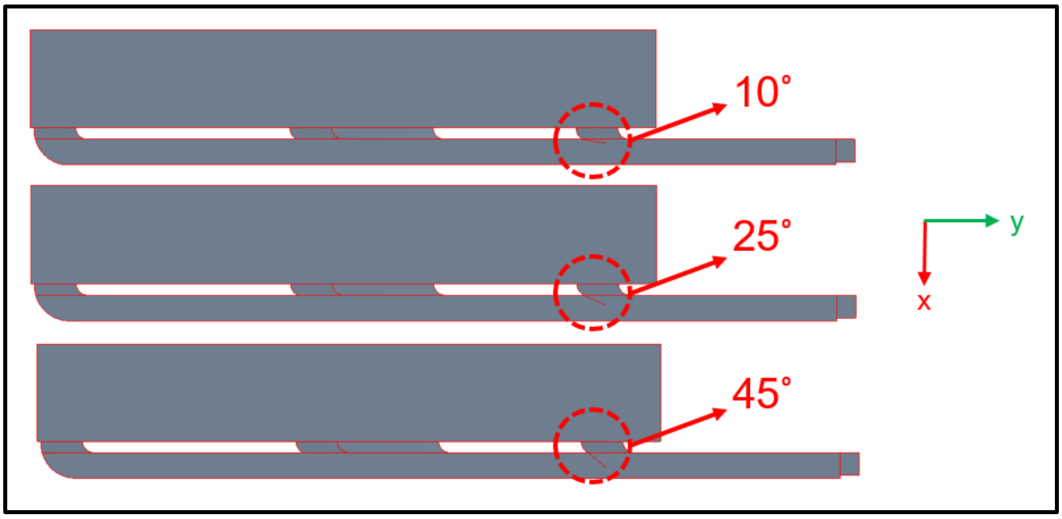

Figure 6-2. Schematic view of the baffles with different angles

A naming has been made to evaluate numerical and experimental results of TM2020 configuration with baffles. It is made in the form of "B-#(˚)-#(mm length). To illustrate, "B-45-250" denotes a baffle configuration with 45˚ angle between it and the horizontal axis, and 250 mm length.

Within the scope of the studies, CFD analyses of the configurations, given in Table 6-1, were conducted. In addition, experimental studies were carried out for a selected configuration "B-25-250" to validate configuration with the baffle.

Table 6-1. Configurations to be analyzed within the scope of studies

Configurations
B-10-125
B-10-250
B-10-375
B-25-125
B-25-250
B-25-375
B-45-125
B-45-250
B-45-375

6.2 Validation of "B-25-250" CFD Model with Experimental Results

Experimental results of "B-25-250" configuration are shown in Figure 6-3. These results include temperature values on the side and the top surface of the multi-purpose box, bottom of the multi-purpose box and the air inside. (See Figure 5-3, Figure 5-4 and Appendix C for the location of the thermocouples.) The data from each thermocouple is separately presented in Figure 6-5 through Figure 6-24 for a better understanding of the experimental results and comparison with the CFD results. In these figures, "S#-CFD" shows the results of the CFD analysis with the rearranged assumptions (the table on the right in Figure 5-9). "S#-Exp" shows experimental results with respect to time. As mentioned, the uncertainty in the temperature measurement is ±0.4˚C [41, 42]. "S#-U+" and "S#-U" shows the upper and lower uncertainty values of the thermocouples due to measurement accuracies, respectively. "S#-Exp(TM2020)" shows experimental results of TM2020 configuration with black lines for all graphs to make comparisons with and without baffle configurations.

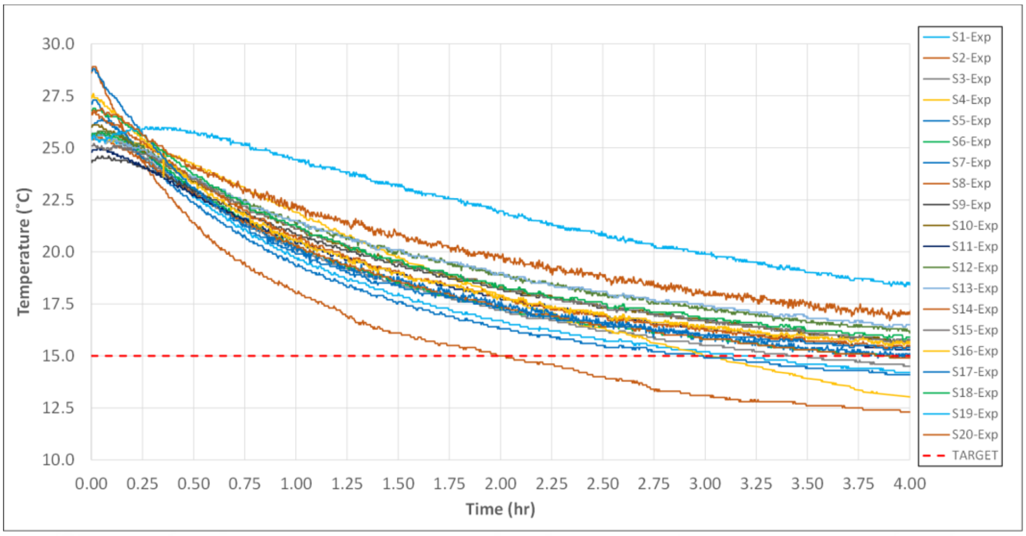

Figure 6-3. Experimental results for TM2020 configuration with 25˚ angle and 250 mm baffle length (i.e., B-25-250 configuration)

According to the Figure 6-3, when the experimental procedure is applied, it is observed that the temperatures are not homogeneously distributed (at t=0) due to preconditioning at the beginning. Since the design objective is conditioning the multi-purpose box and the air inside from 25˚C to 15˚C, the time in the graph was determined as the region where temperatures are approximately 25˚C. Therefore, the graph, experimental and CFD results, is shifted 0.21 hour to left. Rearranged graph is shown in Figure 6-4.

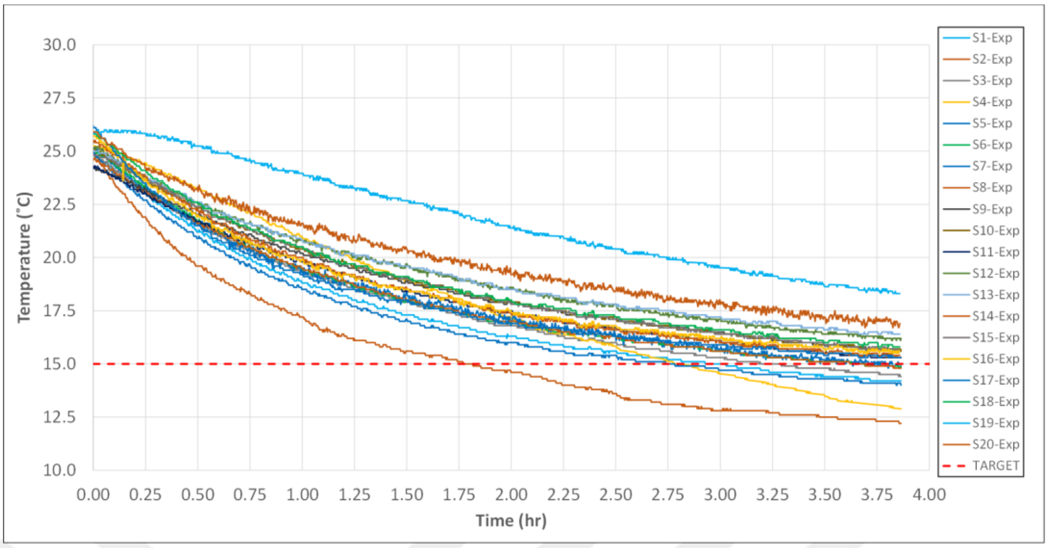

Figure 6-4. Rearranged experimental results for B-25-250 configuration

Thermocouples on the Side and Top Surfaces of the Multi-Purpose Box

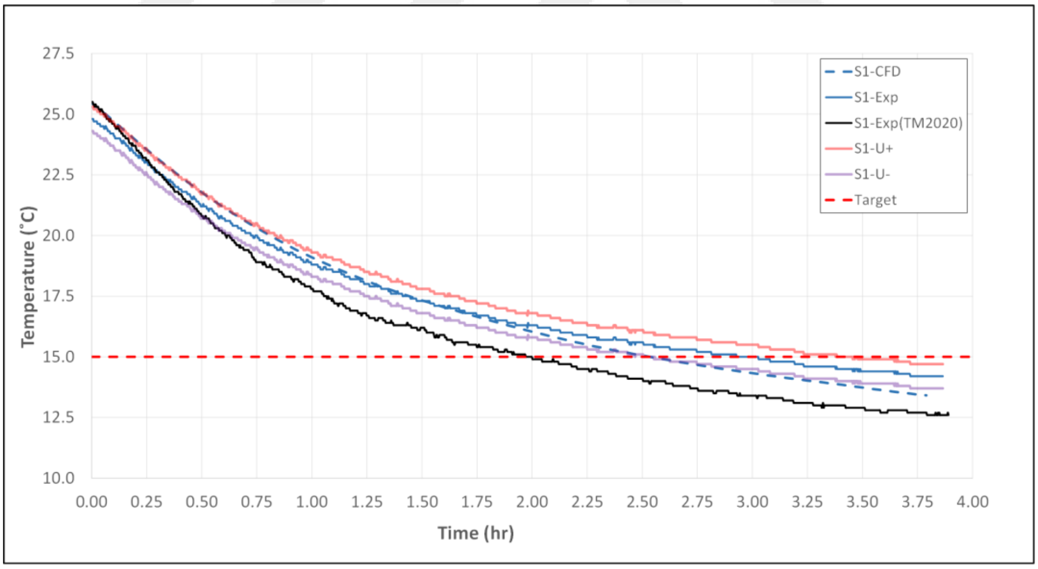

Figure 6-5. Results for S1

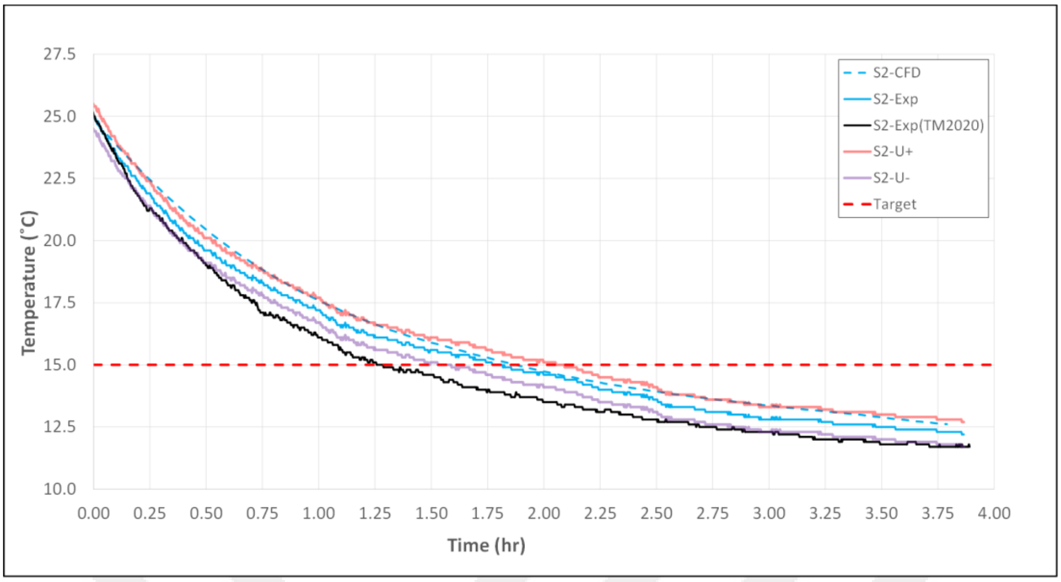

Figure 6-6. Results for S2

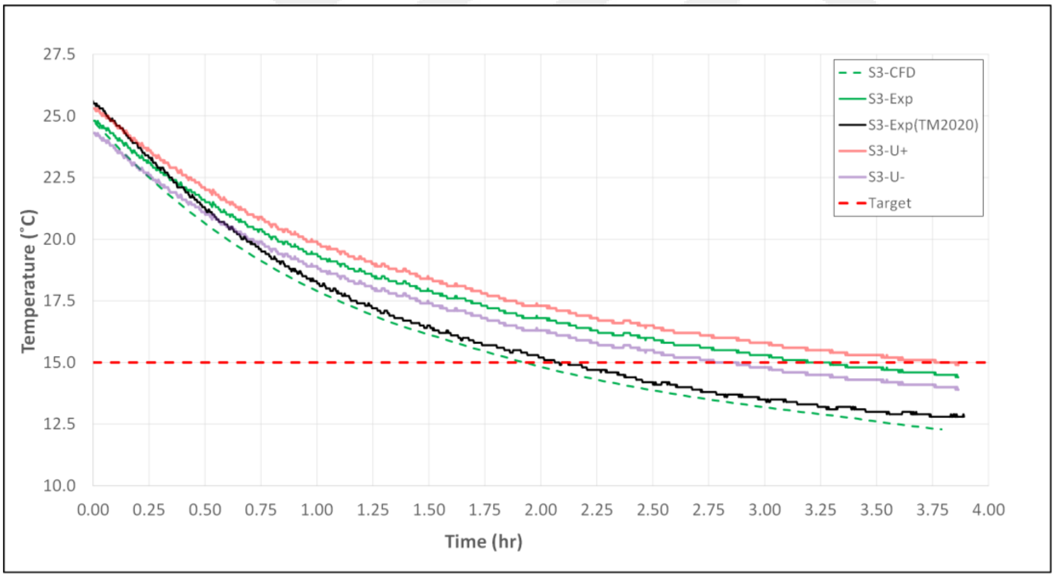

Figure 6-7. Results for S3

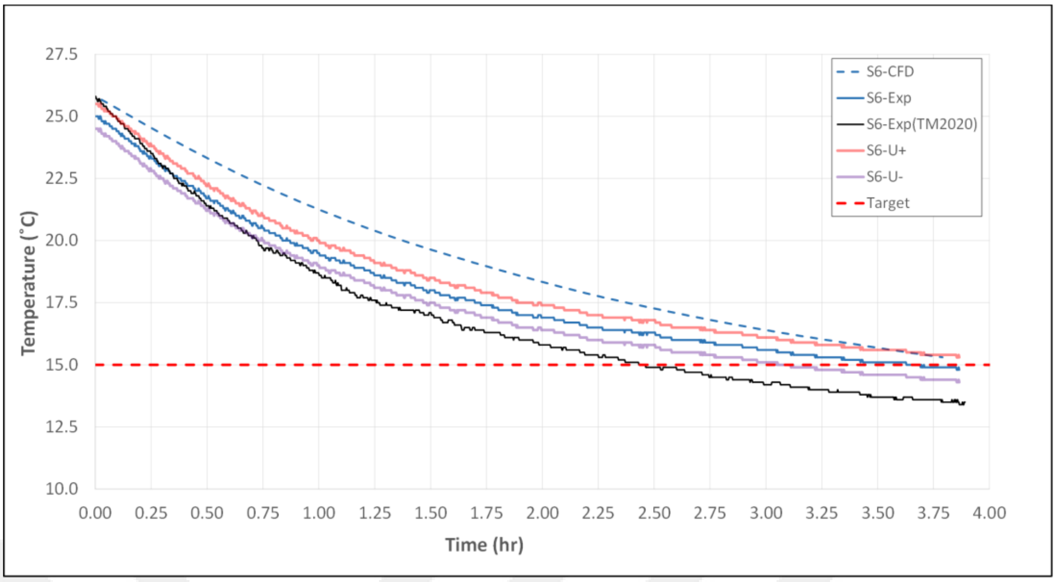

Figure 6-8. Results for S6

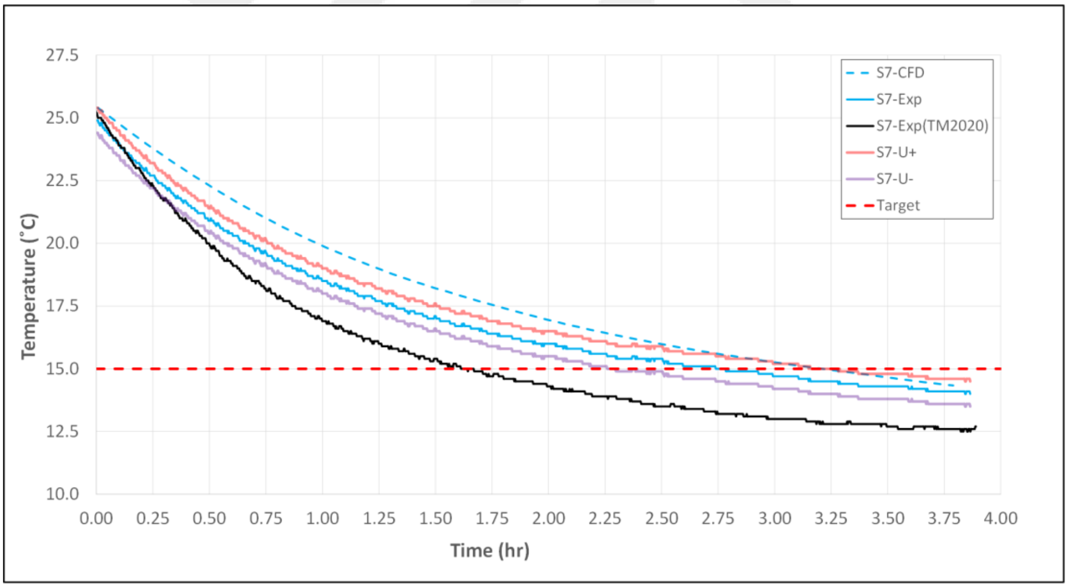

Figure 6-9. Results for S7

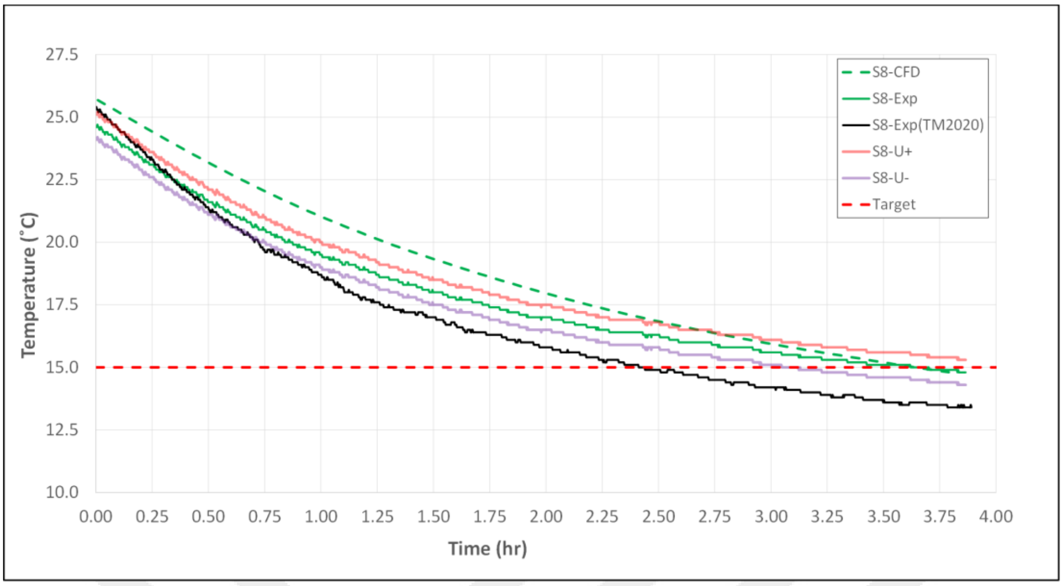

Figure 6-10. Results for S8

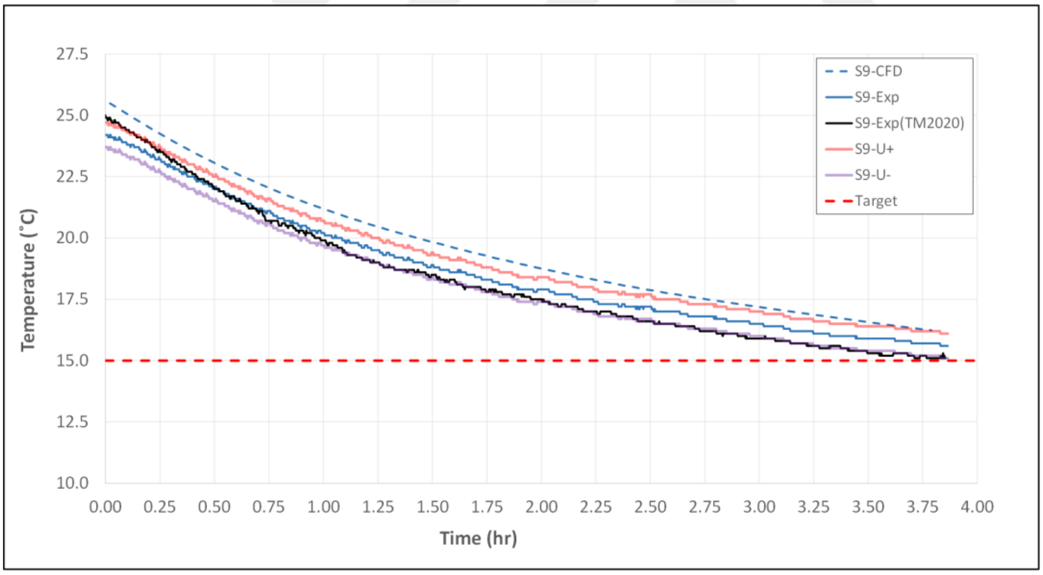

Figure 6-11. Results for S9

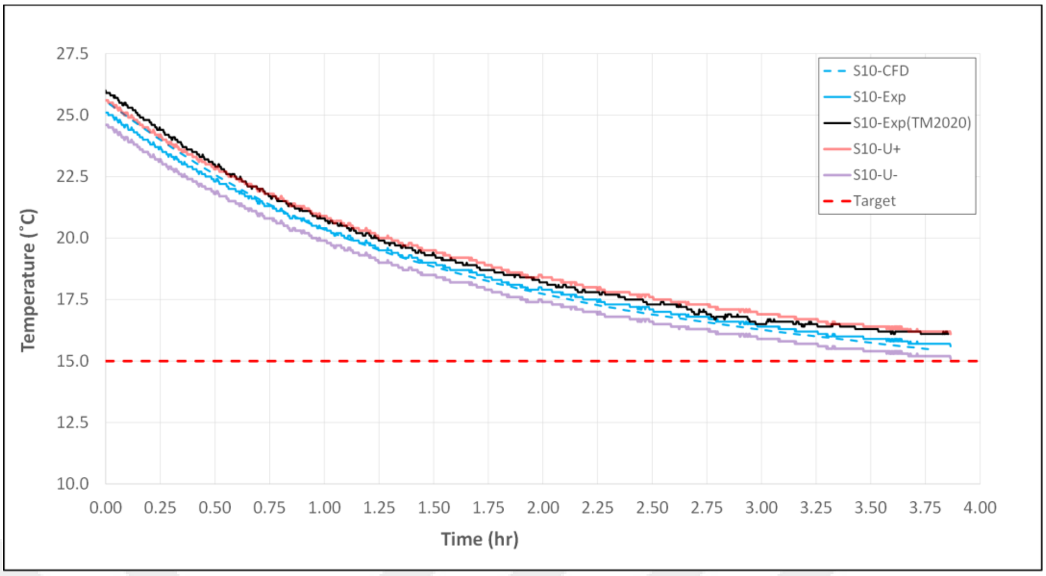

Figure 6-12. Results for S10

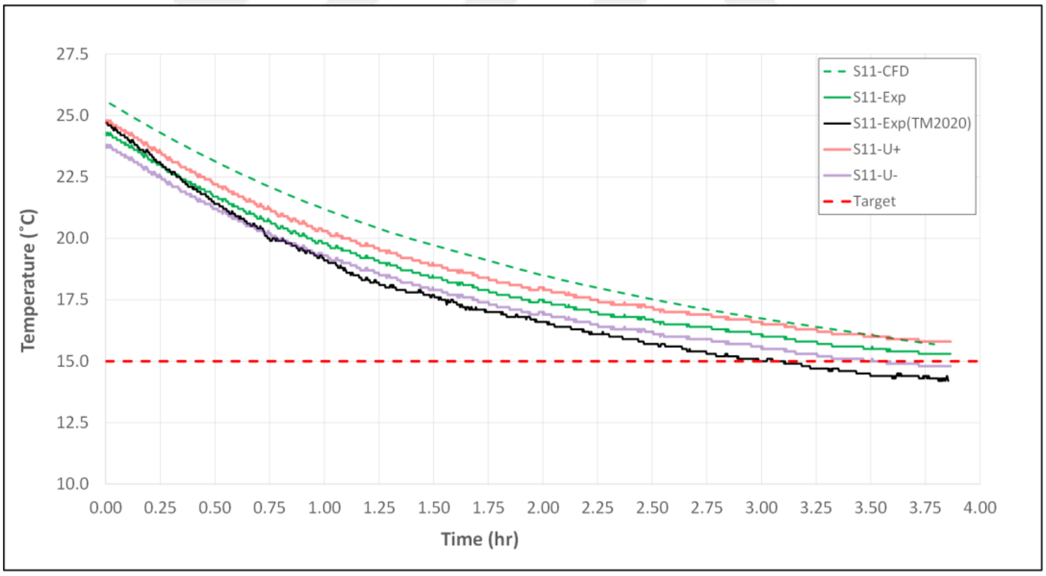

Figure 6-13. Results for S11

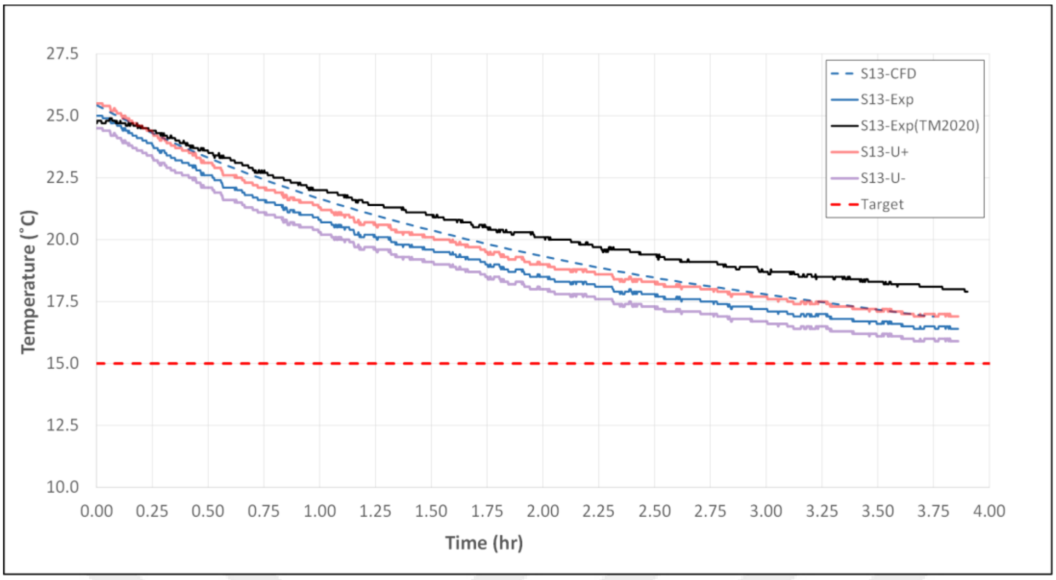

Figure 6-14. Results for S13

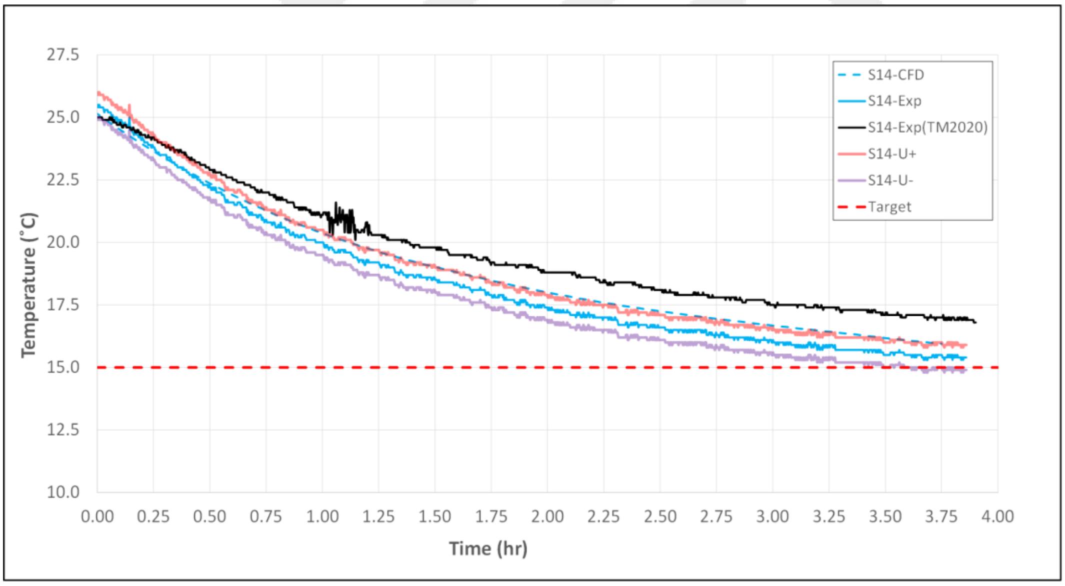

Figure 6-15. Results for S14

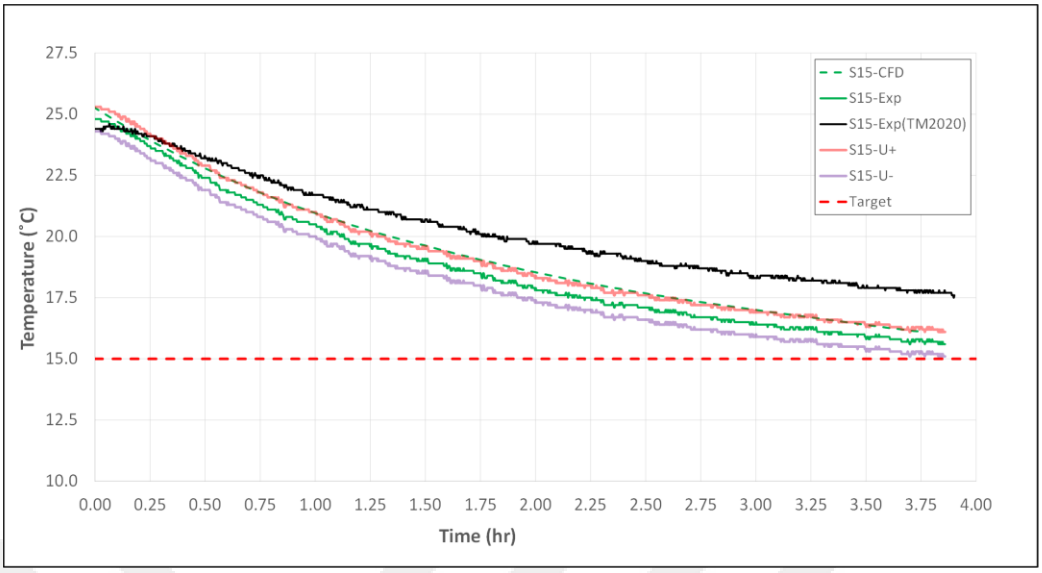

Figure 6-16. Results for S15

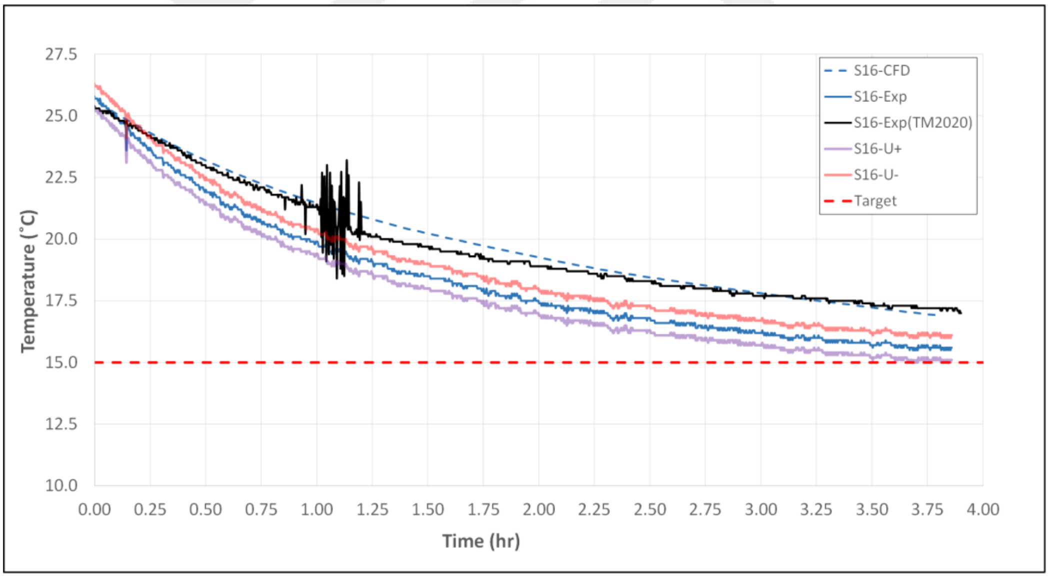

Figure 6-17. Results for S16

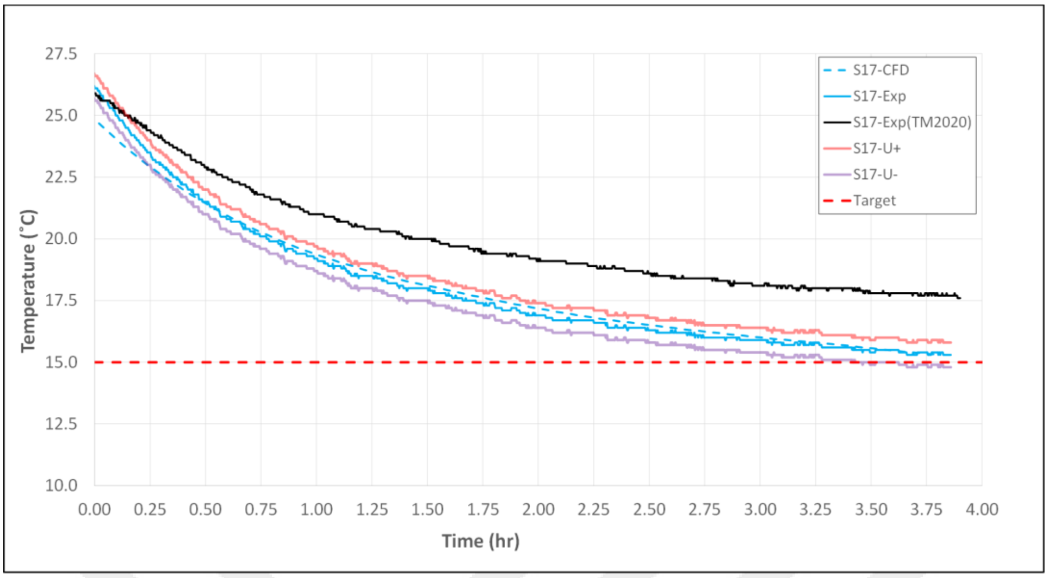

Figure 6-18. Results for S17

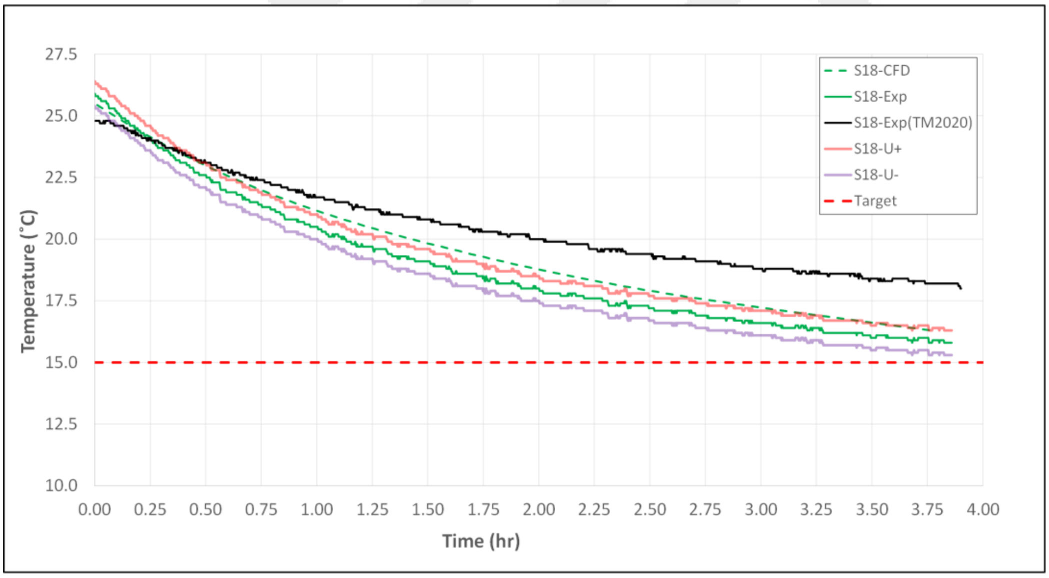

Figure 6-19. Results for S18

Thermocouples on the Bottom Surface of the Multi-Purpose Box

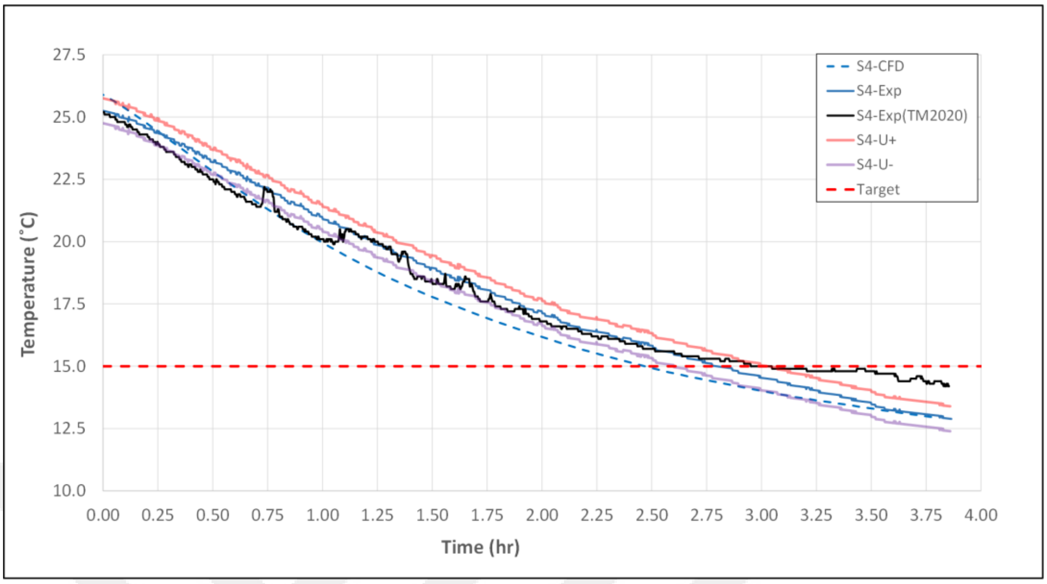

Figure 6-20. Results for S4

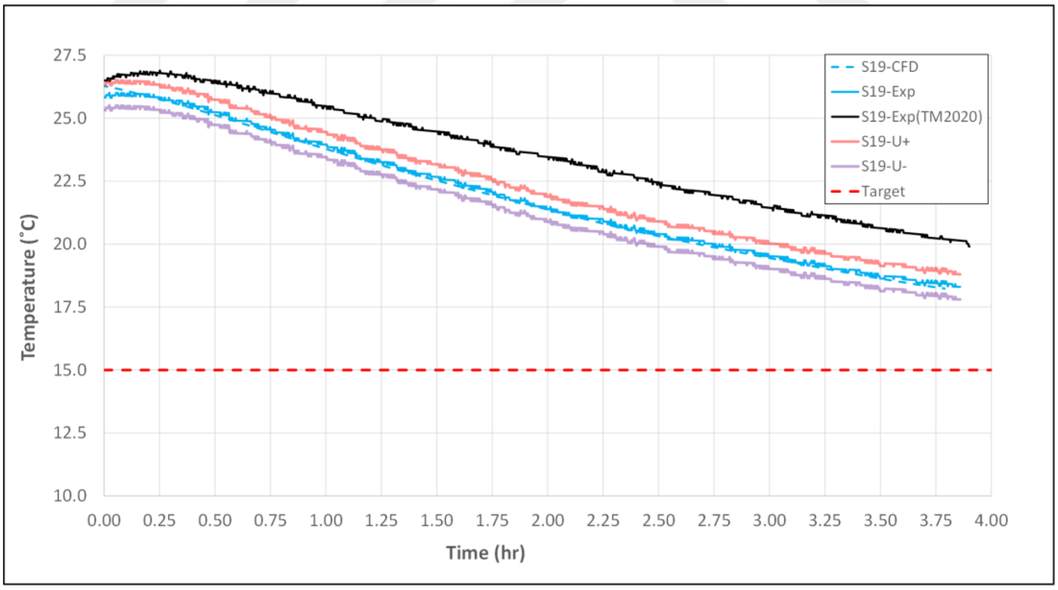

Figure 6-21. Results for S19

Thermocouples in the Air in the Multi-purpose Box

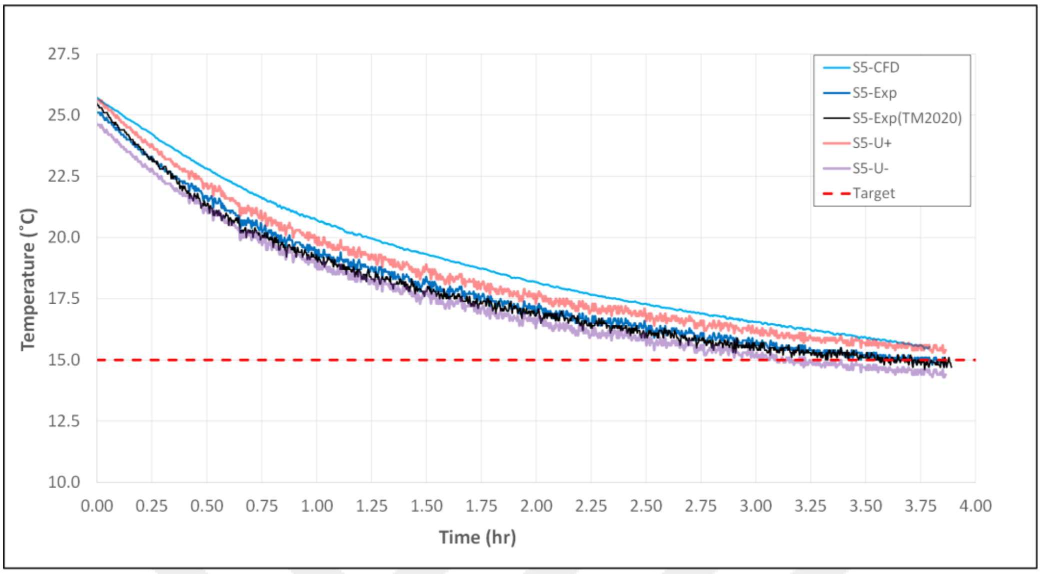

Figure 6-22. Results for S5

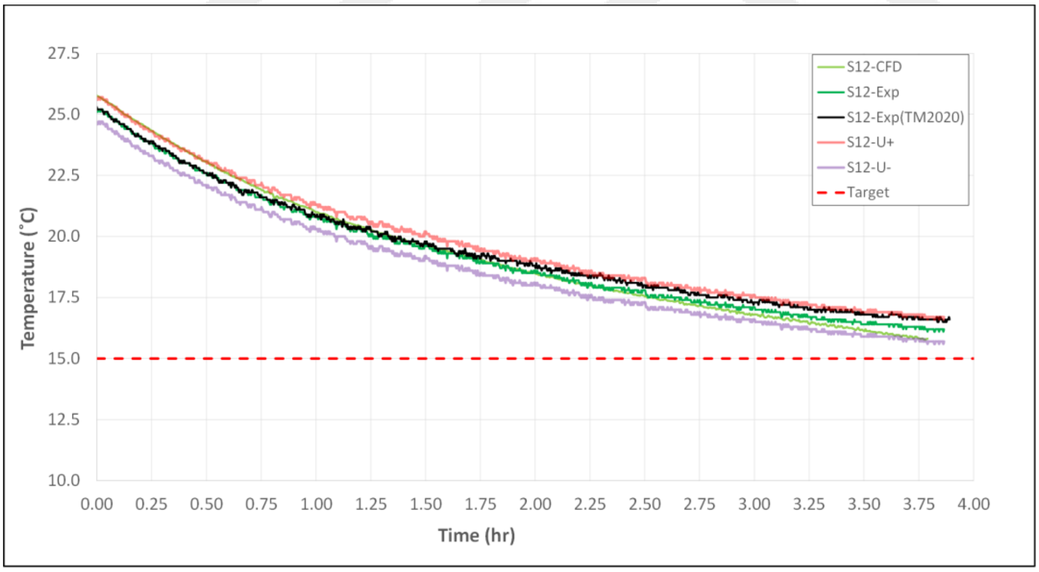

Figure 6-23. Results for S12

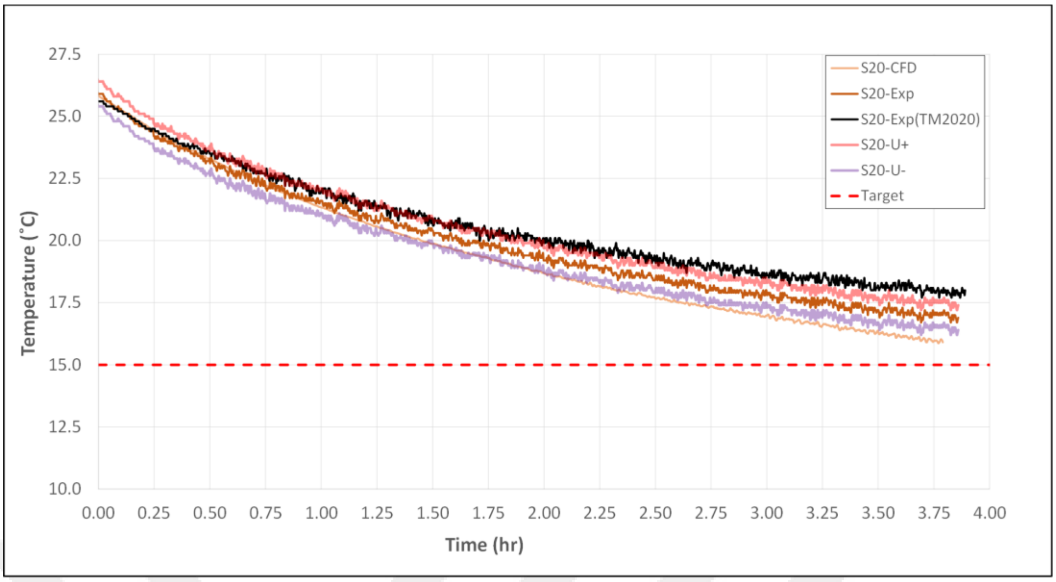

Figure 6-24. Results for S20

Comparison of the experimental and numerical results of volumetric flow rates of the recirculation air passing through each supply register for TM2020 configuration with and without baffle is given in Table 6-2. As it mentioned, the uncertainty of the in-channel averaged pitot tube pressure sensor, used to measure the volumetric flow rates for each supply register, is 2% [43].

Table 6-2. Comparison of experimental and numerical results of the baffled and unbaffled cases for TM2020 configuration

Configurations			Experimental Results					Numerical Results		Relative True Error (%)
Analysis Name	Baffle Angle (°)	Baffle Length (mm)	Measured Average Velocity (m/s)		Measured Volumetric Flow Rate (VFR) (m^3/hr)		VFR (%)	Calculated VFR (m^3/hr)	VFR (%)	
TM2020	-	-	Sensor 1	11.03	1^{st} S. Register	262.63±5.2	17.50	213.30	14.22	18.8
			Sensor 2	9.10	2^{nd} S. Register	530.71±10.6	35.36	545.80	36.39	2.8
			Sensor 3	5.20	3^{rd} S. Register	707.61±14.1	47.14	740.85	49.39	4.7
TM2020 (B-25-250)	25.00	250.00	Sensor 1	11.10	1^{st} S. Register	530.71±10.6	35.14	520.91	34.7	1.8
			Sensor 2	7.20	2^{nd} S. Register	340.2±6.8	22.52	321.75	21.5	5.4
			Sensor 3	4.70	3^{rd} S. Register	639.576±12.8	42.34	657.34	43.8	2.8

When the experimental and CFD results were examined, CFD results were validated for “B-25-250” baffle configuration.

When experimental results of TM2020 configuration with and without baffles, were examined, it is observed that temperature variation, at the end of 4 hours, is more homogeneous in “B-25-250” configuration. In other words, with the addition of the baffle, the temperatures in the 4th and 5th regions decreased, on the other hand the temperatures in 1st and 2nd regions increased. While the highest temperature difference measured from the thermocouple between the highest and the lowest in TM2020 configuration (without baffle) is 8.5˚C, this value is 5.5˚C for B-25-250 configuration (TM2020 configuration with the baffle). The reason is explained by the decrease in the volumetric flow rate in the 2nd and 3rd supply registers with the increase in the 1st supply register, as presented in Table 6-2.

In this configuration, the highest temperature is measured in the 5th region and at the bottom of the multi-purpose box, as in the configuration without baffle. However, this temperature was measured approximately 2˚C lower than the configuration without baffle (see Figure 6-21 and Figure 5-28).

When temperature variation of the air in the multi-purpose box was examined, it was observed that the added baffle did not influence S5 and S12. For S20, the temperature has dropped 1˚C at the end of the experiment when it is compared with TM2020 configuration.

When Table 6-2 is examined, it is observed that the experimental and numerical results are compatible. The highest error was calculated as 5.4% for the 2nd supply register. With the addition of the baffle, more recirculation air passed through the 1st supply register than TM2020 without baffle configuration. This increase was calculated as approximately 100%. However, volumetric flow rate of the recirculation air passing through the second supply register decreased by approximately 40%, since the baffle placed in the first supply register changed the airflow pattern in the inlet channel. For the same reason, the amount of the recirculation air passing through the third supply register has also decreased by 10%.

This caused the temperatures in the 1st and 2nd regions to increase and the temperatures in the 4th and 5th regions to decrease, as mentioned before.

When the recirculation air passing through the supply registers is examined, it is observed that the most air passes through the 3rd supply register when the baffle is installed, similar to the result when no baffle is used.

As shown in the experimental and numerical results in Chapter 5, an increase in temperatures was observed in the first 15 minutes, and the reason is that inlet temperature changed between 40˚C and 10˚C at this time period.

As a result, temperature values and volumetric flow rates of CFD results were validated by experimental results. Thanks to the baffle added to the air conditioning system, it was observed that the temperature values on the multi-purpose box were more homogeneous at the end of 4 hours.

6.3 CFD Results and Optimization

CFD analyses of the configurations, shown in Table 6-1, were run. Temperature values, calculated at the surface of the multi-purpose box and the air inside for each configuration, versus time are shown in Appendix D. In this chapter, the initial temperature condition of the multi-purpose box and the air inside was set as 25˚C, because the aim of the thesis is to reduce the temperatures of the multi-purpose box and the air inside from 25˚C to 15˚C, as mentioned. In this way, the initial conditions of the CFD model, which was validated by experimental studies, were rearranged in accordance with the purpose of the thesis. Configurations were evaluated according to specified two responses. These are “Max. Temp. Diff.” and “Region Below 15˚C (%)” and their explanations are as follows.

<u>Max. Temp. Diff:</u> It is the difference of the maximum and minimum temperature values calculated in the temperature recording points of the CFD model.

Region Below 15˚C (%): It is the volume ratio, as a percentage, of the regions of the multi-purpose box that reach or below the target temperature to the total volume.

Results are tabulated in Table 6-3.

Table 6-3. Results for baffle configurations

Configurations	**Max. Temp. Diff.**	**Region Below 15˚C (%)**
B-10-125	8.01	56.19
B-10-250	7.81	56.30
B-10-375	7.30	57.31
B-25-125	7.26	57.11
B-25-250	4.47	66.20
B-25-375	4.35	70.29
B-45-125	5.94	66.75
B-45-250	3.58	56.14
B-45-375	9.94	35.72

According to the Table 6-3, the highest temperature difference was calculated in the B-45-375 configuration. This configuration is also the one where all the recirculation air passes through of the first supply register. As presented in Figure D-9, while temperatures of the multi-purpose box at the 4th and 5th regions fell below the target temperature in this configuration, the temperature of the other regions did not reach to it. Especially, it was observed that the temperatures in the 1st and 2nd regions were above 20˚C at the end of 4 hours. In other words, this configuration is the worst configuration in terms of homogeneous temperature distribution. Furthermore, it was calculated that only 35.72% of the multi-purpose box volume has reached target temperature or below in this configuration.

The configuration with the lowest temperature difference is B-45-250. This configuration is one of the configurations with the most homogeneous temperature distribution. In addition, the configuration with the highest volume of the multi-purpose box, reaching the target temperature, is B-25-375 with 70.29%.

According to the results in Table 6-3, the regression equations for each response were found in Minitab software as follows:

$$\begin{aligned} Max.Temp.Diff. \\ &= 1.09 + 0.704\alpha + 6.92 \times 10^{-2}L - 7.98 \times 10^{-3}\alpha^2 \\ &- 1.04 \times 10^{-4}L^2 - 6.724 \times 10^{-3}\alpha L \\ &+ 5.6 \times 10^{-5}\alpha^2 L + 0.8 \times 10^{-5}\alpha L^2 \end{aligned} \tag{6.1}$$

$$\begin{aligned} Region\ below\ 15°C\ (\%) \\ &= 77.51 - 2.68 \times \alpha - 0.1685 \times L \\ &+ 5.434 \times 10^{-2} \times \alpha^2 + 1.09 \times 10^{-4}L^2 \\ &+ 2.0106 \times 10^{-2}\alpha L - 3.44 \times 10^{-4}\alpha^2 L \\ &- 0.1 \times 10^{-4}\alpha L^2 \end{aligned} \tag{6.2}$$

where; α and L are the angle and length of the baffle, respectively.

According to the regression equations and results, optimization study was carried out by maximizing the "Region Below 15˚C (%)" and minimizing the "Max. Temp. Diff." values. Results and graphics are shown in Figure 6-25.

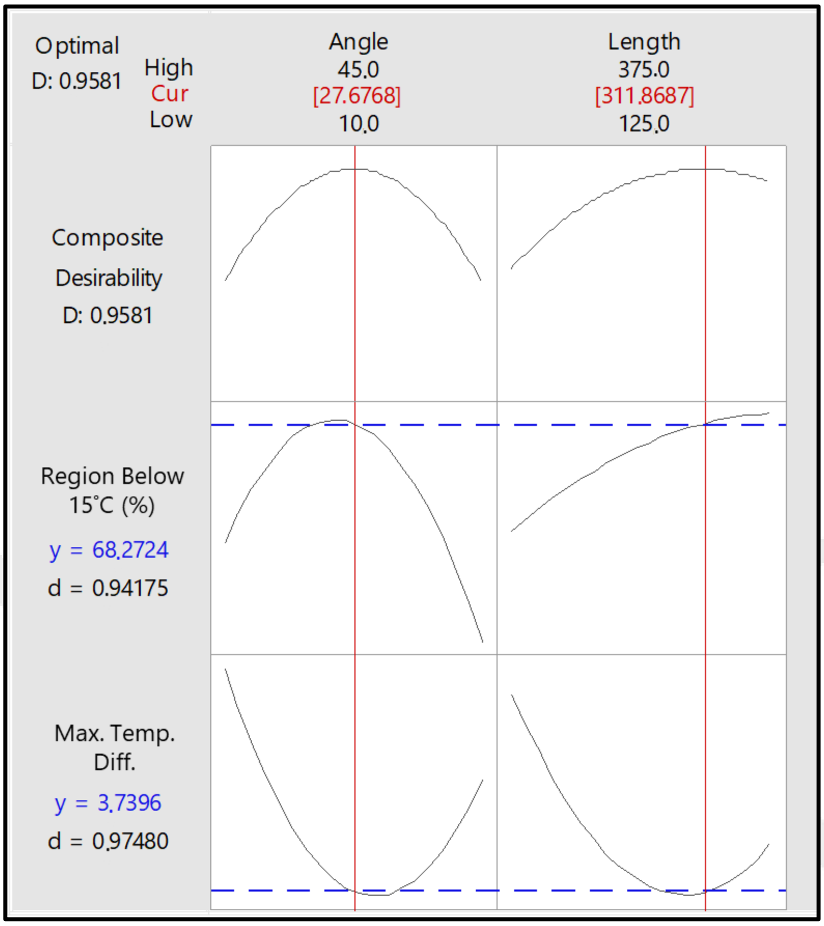

Figure 6-25. Optimization of the baffle configurations

As a result, the individual desirability values for each response were calculated higher than 0.9. In addition, composite desirability of the optimization study was calculated as 0.96. Detailed information about the desirability values is given in Chapter 3.2, page 40-41.

According to Figure 6-25, it has been deemed appropriate to place a baffle with an angle of approximately 28° and a length of 312 mm. The specified baffle angle and length are placed in the 1st supply register in the TM2020 configuration and the CFD analysis was conducted. The CFD results in terms of temperature variation of the multi-purpose box and in the air inside for B-28-312 (TM2020 configuration with

28˚ angle and 312 mm length baffle) are presented in Figure 6-26. The comparison of the CFD results with optimization outputs is given in Table 6-4.

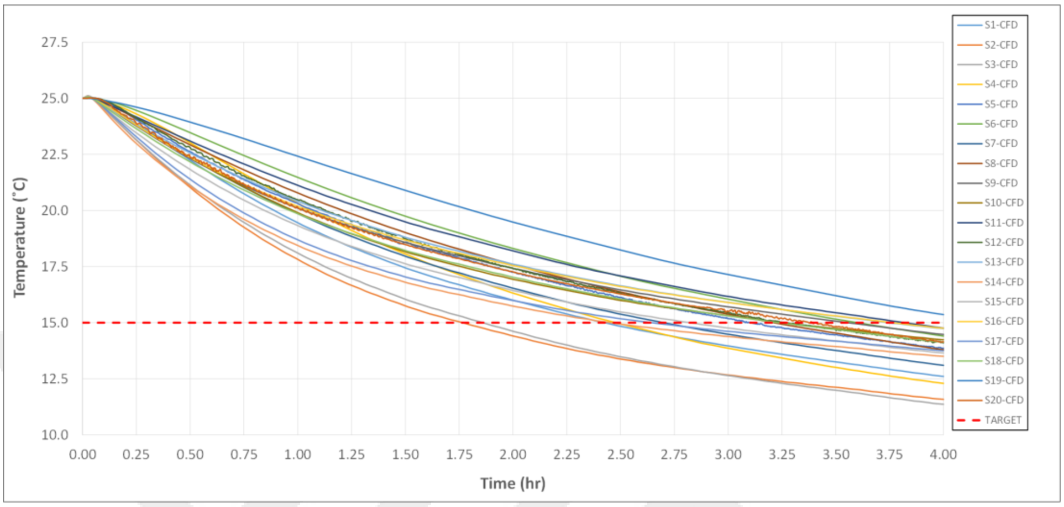

Figure 6-26. Temperature variation at thermocouple locations of the multi-purpose box and the air inside for B-28-312 configuration

Table 6-4. Comparison of the CFD results with optimization outputs

Responses	**Optimization Outputs**	**CFD Results**	**Relative Approximate Error (%)**
Max. Temp. Diff. (˚C)	3.7	4.0	8.1
Region Below 15˚C (%)	68.3	67.9	0.6

According to Figure 6-26, the temperatures calculated, except for S19, have reached the target temperature or below. When the volumetric airflow rate percentages through the supply registers are examined, airflow in the 1st, 2nd and 3rd supply register was calculated as 48.84%, 16.58% and 34.58, respectively. All the air in the multi-purpose box volume has reached the target temperature (15˚C), or below. This graph shows that the temperatures are more homogeneously distributed. According to the results, the calculated maximum temperature difference was 4˚C, and 67.9% of the multi-purpose box volume reached the target temperature or below. When Table 6-4 is examined, it is observed that the optimization outputs and CFD results are compatible with each other. Accordingly, the approximate relative error rate is 8.1% for “Max. Temp. Diff.” and 0.6% for “Region Below 15˚C (%)”.

To examine the effect of the baffle added to the air conditioning system in CFD analyses, the configuration with the baffle is compared with the configuration without baffle in Table 6-5.

Table 6-5. Comparison of results for TM2020 and B-28-312 configurations

Responses	**Configurations**		**Percent Change**
	TM2020	**B-28-312**	
Max. Temp. Diff. (˚C)	8.1	4.0	50.6
Region Below 15˚C (%)	56.1	67.9	21.1

According to Table 6-5, it was observed that the baffle added to the air conditioning system contributed to improvement in the temperature distribution and the increase in the volume, reaching the target temperature. With the addition of the baffle to the 1st supply register of the TM2020 configuration, the maximum temperature difference decreased by 50.6%. Moreover, the rate of the multi-purpose box volume reaching the target temperature or below, increased by 21.1%.

6.4 Conclusions of the Chapter

In this chapter, improvements studies were carried out based on the temperature distribution and volumetric flow rate results in Chapter 5. For this reason, a baffle was placed in the first supply register for TM2020 configuration. A total of 9 CFD analyses were made to optimize the length and angle of this baffle. The selected CFD model, "B-25-250", from baffle configurations was validated by experimental studies. Two evaluation criteria, or responses, were specified for optimization studies. Regression equations were created for each response. As a result of optimization studies, the angle and length of the baffle were determined. With these results, the analysis was performed with validated CFD model and results were compared with TM2020 (without baffle) configuration.

CHAPTER 7

CONCLUSION AND FUTURE WORK

7.1 General

This thesis focuses on the studies carried out for the most efficient air cooling of a multi-purpose box and the air inside. This study was inspired by the problems experienced in the transportation of temperature sensitive products, especially on highways. Within the scope of the thesis, the effect of the position and area of the supply and return register on the temperature distribution have been investigated. Enhancements in cooling with baffle design has also been examined in the scope.

The solution of the problem started with the preparation of the CFD models. STAR CCM+ software program was used for CFD studies. The previously determined initial and boundary conditions are provided as input to the CFD model. According to the first results obtained, it has been observed that the examined factors influence the temperature distribution of the multi-purpose box and the air inside, except for the effect of the return register area percentage. According to the results of 54 CFD analyses, while the VR value was 60% in the MM5020 configuration, this value increased to 98% in the TM2020 configuration. According to the statistical results, higher VR values were obtained, when the supply register position, or number was increased. In addition, when the supply register area percentage was increased, the VR values decreased, since the velocity of the recirculation air in the chamber decreased. It has also been shown that the effect of the return register area percentage is negligible. However, since single interactions are not enough to make comments on the subject, 2 interactions of the factors were also examined and detailed information was given in Chapter 4.4, page 73-75.

In the first 54 CFD analyses, the wall boundary condition of the recirculation air was assumed as adiabatic, and the inlet boundary condition was taken as constant 5˚C.

An experimental setup was constructed to validate the analysis results of TM2020 configuration. First, some trial experiments were made on this experimental setup, and the assumptions used in the analyses were checked. In the trial experimental studies, performed with the AC unit, it was observed that the constant 5˚C inlet boundary condition and adiabatic wall boundary condition assumptions were not valid. According to the studies, it has been understood that a thicker insulation material, or an insulation material with lower thermal conductivity should be used to minimize the heat gain from the control room.

Because of the reasons mentioned above, the variable temperature inlet boundary condition and assumed constant 23˚C temperature wall boundary condition were applied to the analysis model. Thus, the CFD analysis for the TM2020 configuration was repeated, and results were compared with the experimental results. The results showed that the CFD model was validated with high accuracy. When the temperature distribution of the multi-purpose box was examined, it was observed that the temperatures were not homogeneously distributed. The maximum measured temperature difference is approximately 8.5˚C. While the temperatures in the 1st region reach the target temperature, the ratio decreases towards the 5th region. The reason is that while recirculation air passing through the 3rd supply register is approximately 50% of the total flow rate, it was calculated as 14% for the first supply register according to the experimental results.

It was decided to add a baffle to the 1st supply register to regulate airflow pattern in the inlet channel, because it was observed that temperatures in the 4th and the 5th regions were far from the target temperature at the end of 4 hours. For this reason, 9 CFD analyses were carried out to decide the length and the angle of the baffle. Among these analyses, B-25-250 configuration was validated by experimental studies. According to the results of the baffle analyses, when the baffle length is 125 mm and 250 mm, a more homogeneous temperature distribution was obtained when the angle was increased from 10˚ to 45˚, however the same situation had the opposite effect in the 375 mm baffle. The reason is, when the baffle length is 375 mm, and its angle is 45˚, all the recirculation air passed through the 1st supply register. Thus, temperatures of the multi-purpose box at the 1st and 2nd regions did not even reach the 20˚C at the end of the analyses. Similarly, variable effects of increasing the length at constant angle values have observed. For these reasons, it has been concluded that an optimization study for the length and angle is necessary. According to the results, the regression equations for each response were found with the Minitab software, and optimized baffle length and angle was found as 312 mm and 28˚, respectively. CFD analysis was repeated with the validated model and optimized values. The results were first compared with the estimated optimization results. Then, a comparison was made between TM2020 configuration and B-28-312.

To sum up, it has been observed that addition of the baffle makes the temperature distribution of the multi-purpose box more homogeneous. The homogeneous temperature distribution here also affected the temperature distribution of the air in the multi-purpose box. It is important to note that the baffle had an appropriate length and was placed at an appropriate angle in this study. In the air conditioning system, the effects of the baffle to be placed in the 2nd supply register were not examined, however it was observed that there was no difference in the configurations with and without baffle configurations at the temperatures corresponding to the 2nd supply register.

7.2 Future Work

Following studies may be performed in the future to examine temperature distribution of the multi-purpose box and air inside.

- The effect of different inlet temperatures and volumetric flow rates on the temperature distribution can be investigated by changing the equipment such as blower, evaporator, condenser etc, in the AC unit that is used for the thesis study.
- Different supply and return register configurations can be analysed in the CFD environment. Mechanical construction of the chamber limits the

possible configurations in this study. For future chamber design, these limitations can be rearranged according to different supply and register configurations.

- In this thesis, maximum number of 3 supply register positions have been examined in the configurations of supply register positions. By increasing this number, configurations with a larger number of supply registers may be examined. Moreover, asymmetric configurations for register positions can be examined.
- The experimental setup can be improved by working on the insulation material and adding the appropriate insulation material to the experimental setup. Thus, the heat gain from the control room to the air conditioning system can be reduced.
- The effect of the baffle to be added to the second supply register can be examined, and the scope of the design of experiment can be expanded.

REFERENCES

[1] Tassou, S. A., Lewis, J. S., Ge, Y. T., Hadawey, A., and Chaer, I., A Review of Emerging Technologies for Food Refrigeration Applications, Applied Thermal Engineering, vol. 30, pp. 263–276, 2010.

[2] Barbosa, J. R., Ribeiro, G. B., & de Oliveira, P. A. (2012). A state-of-the-art review of compact vapor compression refrigeration systems and their applications. Heat Transfer Engineering, 33(4-5), 356–374. https://doi.org/10.1080/01457632.2012.613275

[3] American Society of Heating, Refrigerating and Air-Conditioning Engineers. ASHRAE Standard: Standards for Natural and Mechanical Ventilation. New York: The Society, 1973.

[4] Gebremedhin, K., & Wu, B. (2005). Simulation of flow field of a ventilated and occupied animal space with different inlet and outlet conditions. *Journal of Thermal Biology*, *30*(5), 343–353. https://doi.org/10.1016/j.jtherbio.2004.10.001

[5] Maher, D., Issakhov, A. (2021). *Effect of Inlet/Outlet on Thermal Performance of Naturally Ventilated Building.* International Journal of Low-Carbon Technologies 16(2). https://doi:10.1093/ijlct/ctab055

[6] Lim, T. G., & Kim, Y. H. (2014). Analysis of Airflow Pattern in Plant Factory with Different Inlet and Outlet Locations using Computational Fluid Dynamics. *Journal of Biosystems Engineering*, *39*(4), 310–317. https://doi.org/10.5307/jbe.2014.39.4.310

[7] Yongson, O., Badruddin, I. A., Zainal, Z. A., & Aswatha Narayana, P. A. (2007). *Airflow analysis in an Air Conditioning Room*. Building and Environment, 42(3), 1531–1537. https://doi.org/10.1016/j.buildenv.2006.01.002

[8] Lenin, V. R., Sivalakshmi, S., & Raja, M. (2018). *Optimization of window type and vent parameters on single-sided natural ventilation buildings*. Journal of

Thermal Analysis and Calorimetry, 136(1), 367–379. https://doi.org/10.1007/s10973-018-7913-4

[9] Koufi, L., Younsi, Z., Cherif, Y., & Naji, H. (2017). *Numerical investigation of turbulent mixed convection in an open cavity: Effect of inlet and outlet openings*. International Journal of Thermal Sciences, 116, 103–117. https://doi.org/10.1016/j.ijthermalsci.2017.02.007

[10] Perén, J. I., van Hooff, T., Leite, B. C. C., & Blocken, B. (2015). *CFD analysis of cross-ventilation of a generic isolated building with asymmetric opening positions: Impact of roof angle and opening location.* Building and Environment, 85, 263–276. https://doi.org/10.1016/j.buildenv.2014.12.007

[11] Khaled, A., Saadeddin. (2016). *The Effects Of Diffuser Exit Velocity And Distance Between Supply And Return Apertures On The Efficiency Of An Air Distribution System In An Office Space.* Master Thesis, South Dakota State University, Minneapolis.

[12] Susin, R. M., Lindner, G. A., Mariani, V. C., & Mendonça, K. C. (2009). Evaluating the influence of the width of inlet slot on the prediction of indoor airflow: Comparison with experimental data. *Building and Environment*, *44*(5), 971–986. https://doi.org/10.1016/j.buildenv.2008.06.021

[13] Murakami, S., & Kato, S. (1989). Numerical and experimental study on room airflow—3-D predictions using the k-ϵ turbulence model. *Building and Environment*, *24*(1), 85–97. https://doi.org/10.1016/0360-1323(89)90019-x

[14] Harral, B., & Boon, C. (1997). Comparison of Predicted and Measured Air Flow Patterns in a Mechanically Ventilated Livestock Building without Animals. *Journal of Agricultural Engineering Research*, *66*(3), 221–228. https://doi.org/10.1006/jaer.1996.0140

[15] Bjerg, B., Svidt, K., Zhang, G., Morsing, S., & Johnsen, J. (2002). Modeling of air inlets in CFD prediction of airflow in ventilated animal houses. *Computers and*

Electronics in Agriculture, *34*(1–3), 223–235. https://doi.org/10.1016/s0168-1699(01)00189-2

[16] Hatif, I. H., Hariri, A., & Idris, A. F. (2020). *CFD analysis on effect of Air Inlet and outlet location on air distribution and thermal comfort in small office*. CFD Letters, 12(3), 66–77. https://doi.org/10.37934/cfdl.12.3.6677

[17] Montazeri, H., & Montazeri, F. (2018). *CFD simulation of cross-ventilation in buildings using rooftop wind-catchers: Impact of outlet openings*. Renewable Energy, 118, 502–520. https://doi.org/10.1016/j.renene.2017.11.032

[18] Chen, T., Feng, Z., & Cao, S.-J. (2019). The effect of Vent Inlet aspect ratio and its location on ventilation efficiency. Indoor and Built Environment, 29(2), 180–195. https://doi.org/10.1177/1420326x19865930

[19] Cao, S.-J., Deng, H.-Y., Zhou, X., & Deng, Y. (2018). *Ventilation inlets design based on ventilation performance assessment using a dimensionless time scale.* Indoor and Built Environment, 28(8), 1049–1063. https://doi.org/10.1177/1420326x18815321

[20] Khan, J. A., Feigley, C. E., Lee, E., Ahmed, M. R., & Tamanna, S. (2006). *Effects of inlet and exhaust locations and emitted gas density on indoor air contaminant concentrations*. Building and Environment, 41(7), 851–863. https://doi.org/10.1016/j.buildenv.2005.04.002

[21] Cheng, Y., Zhang, S., Huan, C., Oladokun, M. O., & Lin, Z. (2019). *Optimization on fresh outdoor air ratio of air conditioning system with stratum ventilation for both targeted indoor air quality and maximal energy saving. Building and Environment*, 147, 11–22. https://doi.org/10.1016/j.buildenv.2018.10.009

[22] Kurtbaş, R. (2008). The effect of different inlet conditions of air in a rectangular channel on convection heat transfer: Turbulence flow. *Experimental Thermal and Fluid Science*, *33*(1), 140–152.https://doi.org/10.1016/j.expthermflusci.2008.07.012

[23] Moureh, J., & Flick, D. (2004). Airflow pattern and temperature distribution in a typical refrigerated truck configuration loaded with pallets. *International Journal of Refrigeration*, *27*(5), 464–474. https://doi.org/10.1016/j.ijrefrig.2004.03.003

[24] Nada, S. A., Said, M. A., & Rady, M. A. (2016). *Numerical investigation and parametric study for thermal and energy management enhancements in data centers' buildings.* Applied Thermal Engineering, 98, 110–128. https://doi.org/10.1016/j.applthermaleng.2015.12.020

[25] Roh, J., Cho, H., Choi, Y., Park, H., Moon, I., & Kim, J. (2020). CFD-based Design Optimization of Air Quenching Equipment to Enhance the Cooling Effect. Computer Aided Chemical Engineering, 289–294. https://doi.org/10.1016/b978-0-12-823377-1.50049-5

[26] Assari, M. R., Basirat Tabrizi, H., & Savadkohy, M. (2018). Numerical and experimental study of inlet-outlet locations effect in horizontal storage tank of solar water heater. *Sustainable Energy Technologies and Assessments*, *25*, 181–190. https://doi.org/10.1016/j.seta.2017.12.009

[27] F. M. White, Viscous Fluid Flow, 2nd ed., McGraw-Hill, 1991 (QA929 .W48)

Allmendinger, R. W.1999. Introduction to Structural Geology. Lecture notes. 279 p.

[28] Tu, J., Yeoh, G. H., & Liu, C. (2018). Computational fluid dynamics a practical approach. Elsevier/BH.

[29] Versteeg, H. K., & Malalasekera, W. (2011). *An introduction to computational fluid dynamics: The Finite Volume Method*. Prentice Hall.

[30] B.E. Launder, D.B. Spalding, Lectures in Mathematical Models of Turbulence, McGraw-Hill, (1972).

[31] Shih, T.-H., Liou, W.W., Shabbir, A., Yang, Z. and Zhu, J. 1994. "*A Ne*

ε *Eddy Viscosity Model for High Reynolds Number Turbulent Flows Model*

Development and Validation", NASA TM 106721.

[32] Siemens STAR CCM+ https://help.sw.siemens.com

[33] Fisher, R. A. (1925). Statistical methods for research workers. Edinburgh: Oliver and Boyd.

[34] Box, G. E. P., & Wilson, K. B. (1951). Experimental attainment of optimum conditions. Journal of the Royal Statistical Society, 13, 1–45.

[35] Taguchi, G., & Wu, Y. (1980). Introduction to off-line quality control. Nagoya: Central Japan Quality Control Association.

[36] MONTGOMERY, D. O. U. G. L. A. S. C. (2021). Design and analysis of Experiments. JOHN WILEY & SONS.

[37] M. Cavazzuti, Optimization Methods: From Theory to Design, Springer-Verlag Berlin Heidelberg, 2013.

[38] Standardization Agreement STANAG 2895, February 2001

[39] TC Direct, https://www.tcdirect.co.uk/, 11/06/2022

[40] Schedule of Accreditation issued by United Kingdom Accreditation Service, 30March 2020, 2 Pine Trees, Chertsey Lane, Staines-upon-Thames, TW18 3HR, UK

[41] OMEGA, https://assets.omega.com

[42] EXTECH, http://www.extech.com

[43] Tetisan Tesisat. (n.d.). Retrieved August 21, 2022, from https://tetisantesisat.com/

[44] Guide: Guide for the verification and validation of Computational Fluid Dynamics Simulations (AIAA G-077-1998(2002)). (1998). Guide: Guide for the Verification and Validation of Computational Fluid Dynamics Simulations (AIAA G-077-1998(2002)). https://doi.org/10.2514/4.472855.001

[45] Freitas, C. J. (2006). Verification and validation in computational fluid dynamics and heat transfer: PTC 61. ASME 2006 Power Conference. https://doi.org/10.1115/power2006- 88166

[46] Roache, P. J., 1998, Verification and Validation in Computational Science and Engineering, Hermosa Publishers, Albuquerque, August 1998. http://www.hermosa-pub.com/hermosa.

[47] 11. Roache, P. J., 1993, "A Method for Uniform Reporting of Grid Refinement Studies," Proceedings of Quantification of Uncertainty in Computation Fluid Dynamics, Edited by Celik, et al., ASME Fluids Engineering Division Spring Meeting, Washington D.C., June 230-240, ASME Publ. No. FED-Vol. 158.

[48] Coleman, H. W. and Stern F., 1997, "Uncertainties in CFD Code Validation," ASME Journal of Fluids Engineering, Vol. 119, pp. 795-803.

[49] Dunnett, C. W., & Sobel, M. (1954). A Bivariate Generalization of Student's t-distribution, with Tables for Certain Special Cases. Biometrika, 41(1-2), 153–169. doi:10.1093/biomet/41.1-2.153

[50] Wang, T., Sheng, C., & Nnanna, A. G. A. (2014). Experimental investigation of air conditioning system using evaporative cooling condenser. Energy and Buildings, 81, 435–443. https://doi.org/10.1016/j.enbuild.2014.06.047

[51] Miller, R., & Miller, M. R. (2012). Air Conditioning and refrigeration. McGraw-Hill Professional.

APPENDICES

A. The Mesh Images and the Residual Graph

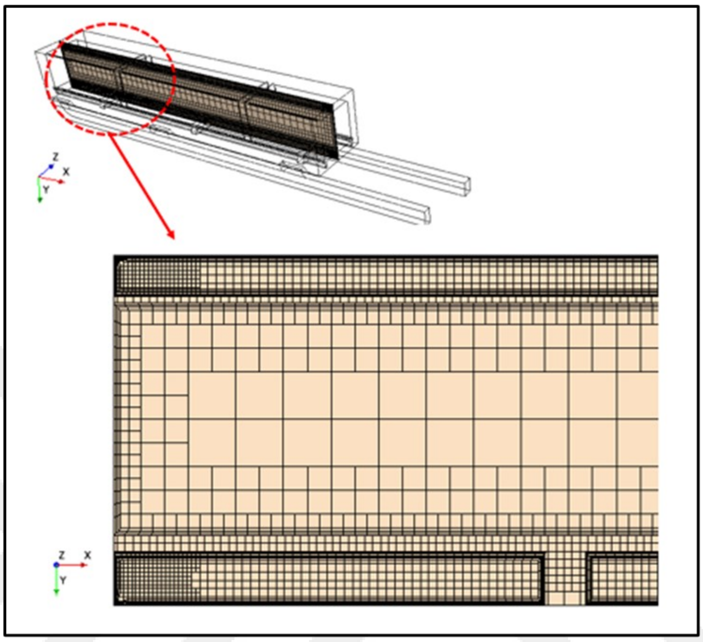

Figure A-1. A mesh image of an illustrative configuration (TM2020)

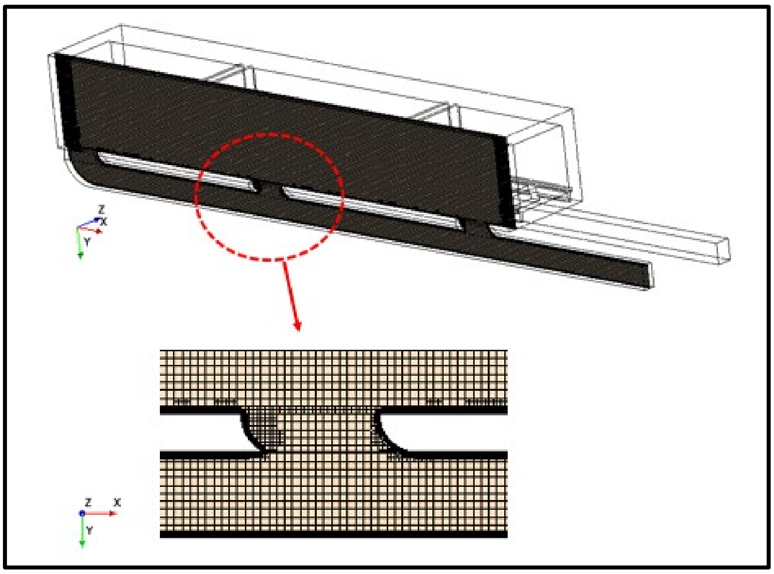

Figure A-2. A mesh image of an illustrative Configuration (TM2020)

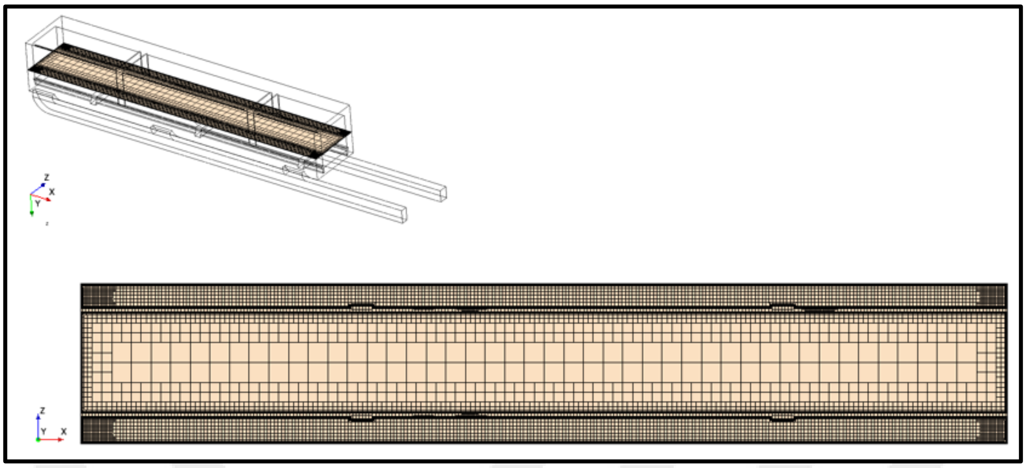

Figure A-3. A mesh image of an illustrative Configuration (TM2020)

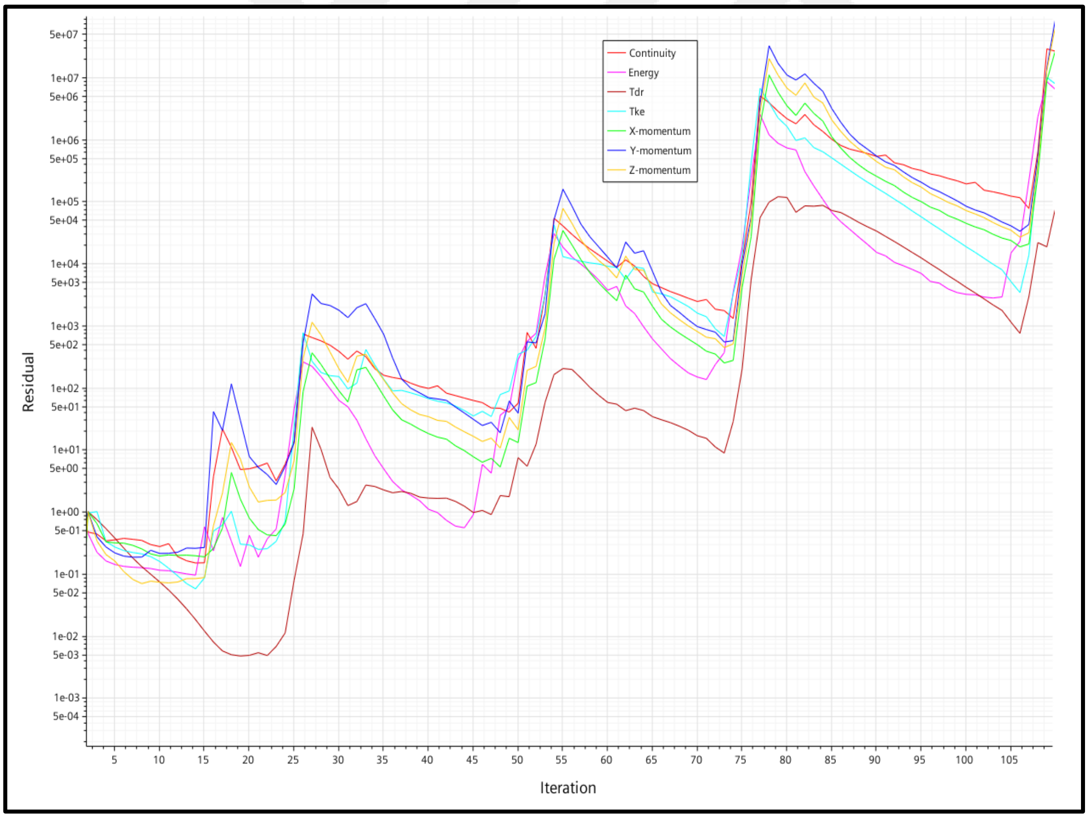

Figure A-4. Screenshot of the residual graph for the analysis with 0.4-time step

B. Pressure Drop and Outlet Temperature Values for 54 Configurations

Table B-1. Pressure drop and outlet temperature values for 54 configurations

Configurations	**Pressure Drop (Pa)**	**Outlet Temperature (˚C)**
MM2020	159.3	8.79
MM2035	139.5	8.95
MM2050	136.0	9.19
MM3520	152.3	8.77
MM3535	136.1	8.88
MM3550	131.8	9.10
MM5020	146.9	8.76
MM5035	130.3	8.87
MM5050	126.0	9.10
MD2020	150.6	9.41
MD2035	137.6	9.39
MD2050	134.3	9.37
MD3520	142.6	9.21
MD3535	129.2	9.20
MD3550	127.0	9.19
MD5020	138.4	9.16
MD5035	124.6	9.15
MD5050	122.6	9.14
DM2020	146.3	9.13
DM2035	132.2	9.17
DM2050	127.7	9.21
DM3520	141.2	8.81
DM3535	125.3	8.87
DM3550	118.2	8.87
DM5020	138.1	8.86
DM5035	119.3	8.98
DM5050	114.5	8.99

Configurations	Pressure Drop (Pa)	Outlet Temperature (˚C)
DD2020	135.1	8.96
DD2035	120.9	9.03
DD2050	121.6	8.98
DD3520	136.5	8.98
DD3535	120.4	8.98
DD3550	116.8	9.02
DD5020	136.2	8.99
DD5035	118.1	9.00
DD5050	114.4	8.83
TM2020	143.1	9.42
TM2035	129.0	9.30
TM2050	125.4	9.28
TM3520	143.0	9.03
TM3535	127.4	9.06
TM3550	122.0	9.04
TM5020	141.3	9.10
TM5035	131.9	9.04
TM5050	119.1	8.86
TD2020	135.7	9.13
TD2035	131.9	9.03
TD2050	123.5	8.91
TD3520	130.7	9.01
TD3535	123.4	8.91
TD3550	120.0	8.83
TD5020	133.2	8.81
TD5035	120.9	8.75
TD5050	118.7	8.76

C. Location of The Temperature Recording Points and Thermocouples

Table C-1. Location of the temperature recording points and thermocouples

Naming	Location
S1	Side surface of the multi-purpose box
S2	Top surface of the multi-purpose box
S3	Side surface of the multi-purpose box
S4	Bottom surface of the multi-purpose box
S5	The air in the multi-purpose box
S6	Side surface of the multi-purpose box
S7	Top surface of the multi-purpose box
S8	Side surface of the multi-purpose box
S9	Side surface of the multi-purpose box
S10	Top surface of the multi-purpose box
S11	Side surface of the multi-purpose box
S12	The air in the multi-purpose box
S13	Side surface of the multi-purpose box
S14	Top surface of the multi-purpose box
S15	Side surface of the multi-purpose box
S16	Side surface of the multi-purpose box
S17	Top surface of the multi-purpose box
S18	Side surface of the multi-purpose box
S19	Bottom surface of the multi-purpose box
S20	The air in the multi-purpose box
S21	The inlet channel
S22	The outlet channel

D. Temperature Variation for Different Baffle Configurations

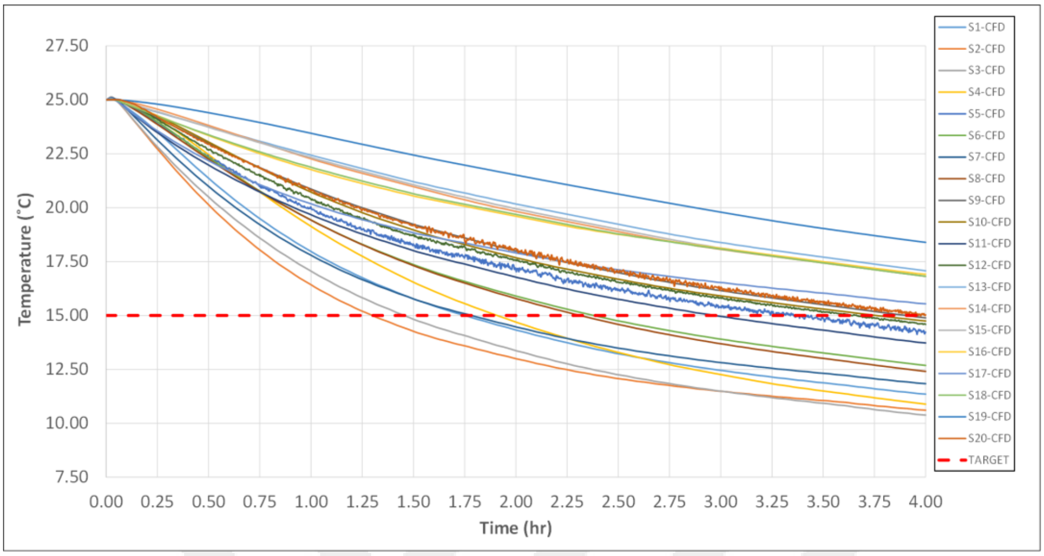

Figure D-1. Temperature variation for B-10-125 configuration

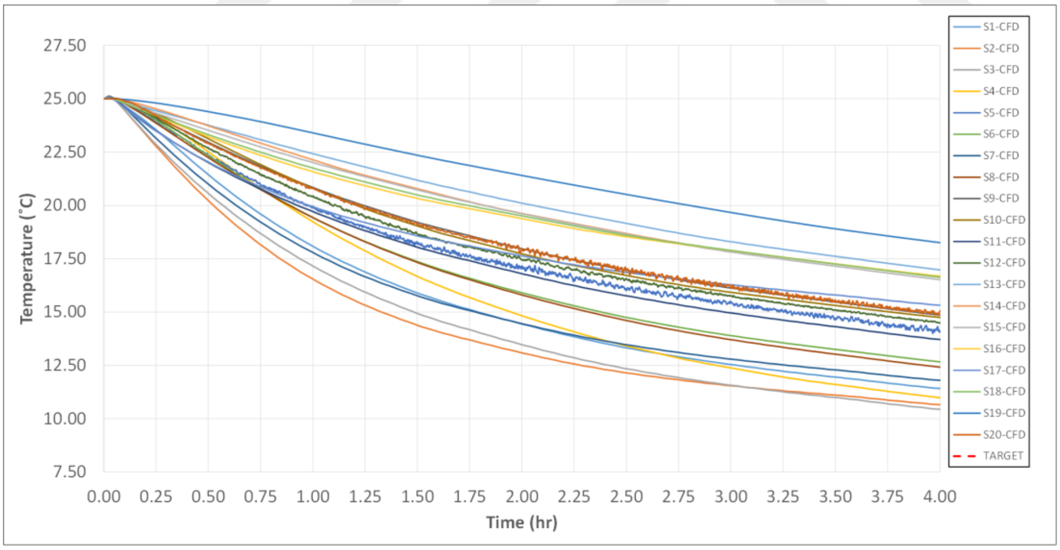

Figure D-2. Temperature variation for B-10-250 configuration

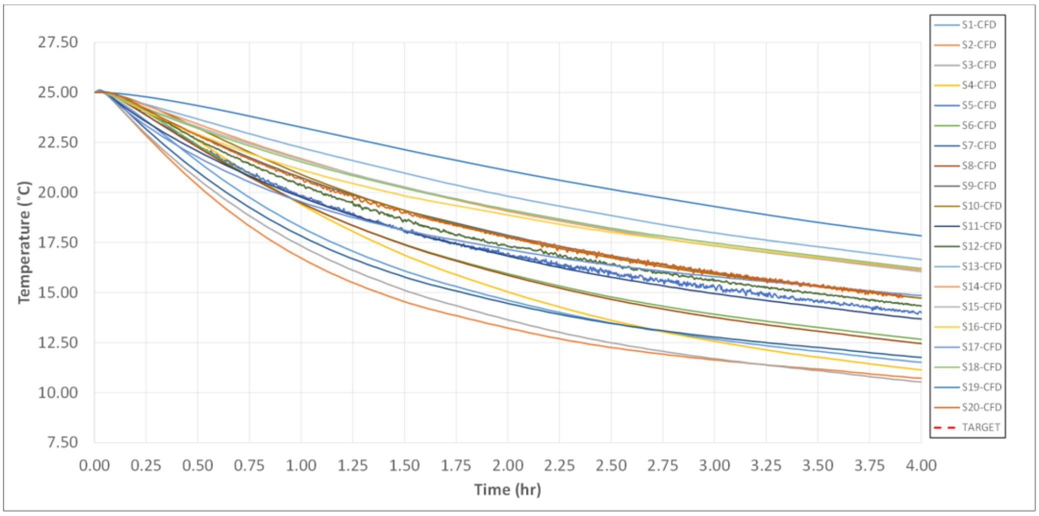

Figure D-3. Temperature variation for B-10-375 configuration

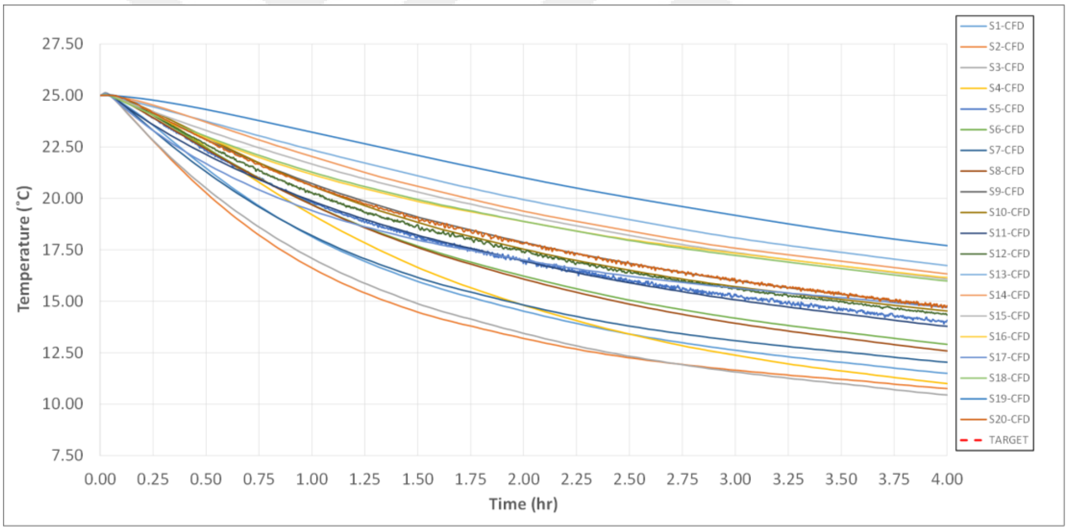

Figure D-4. Temperature variation for B-25-125 configuration

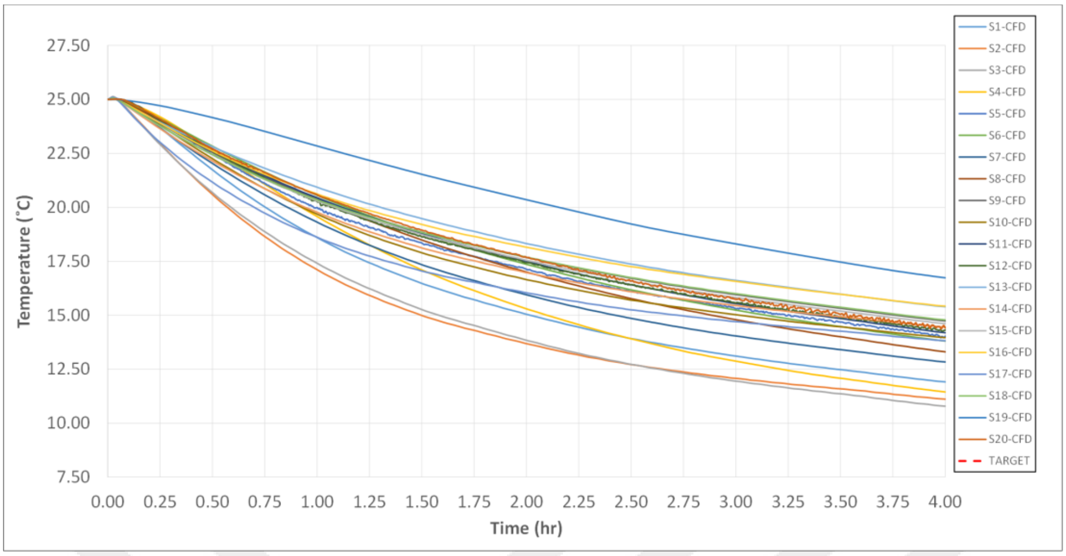

Figure D-5. Temperature variation for B-25-250 configuration

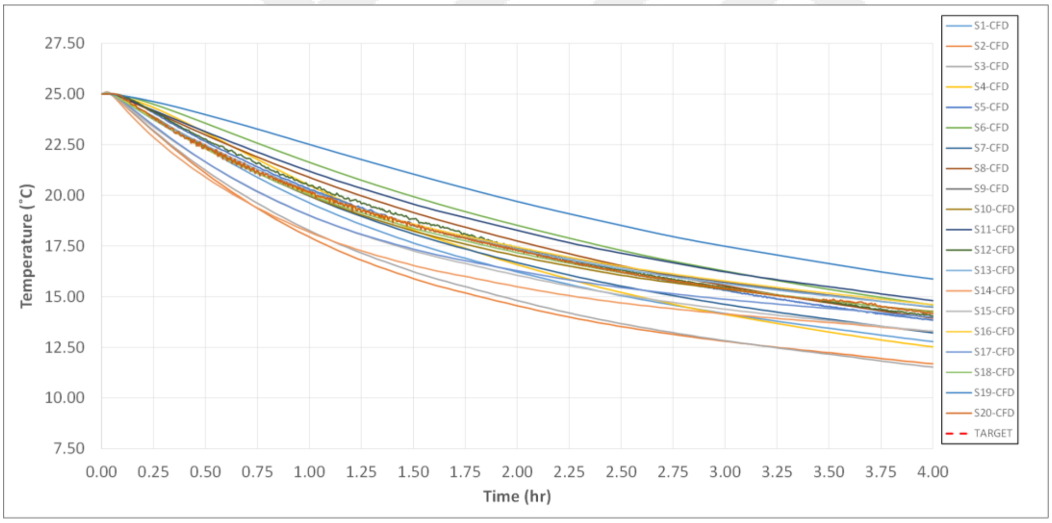

Figure D-6. Temperature variation for B-25-375 configuration

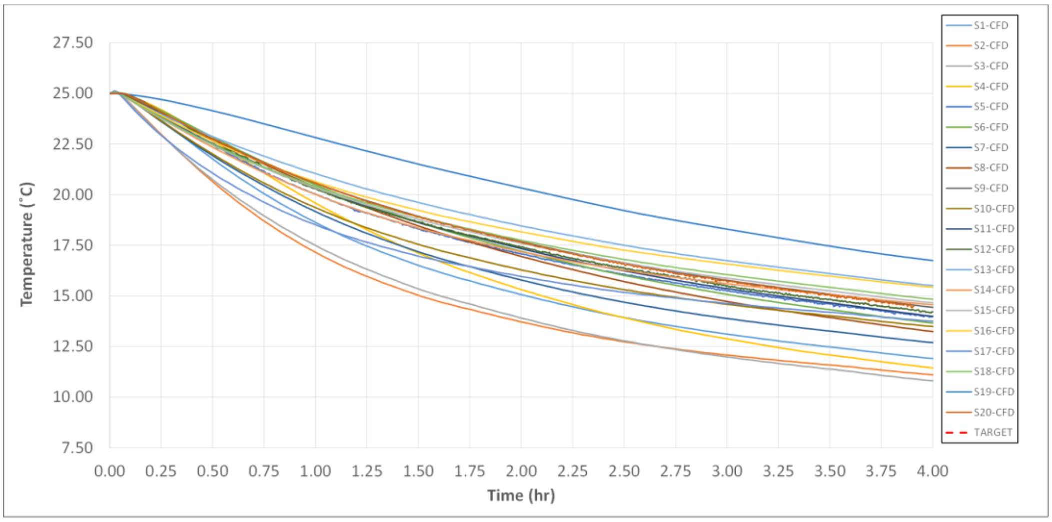

Figure D-7. Temperature variation for B-45-125 configuration

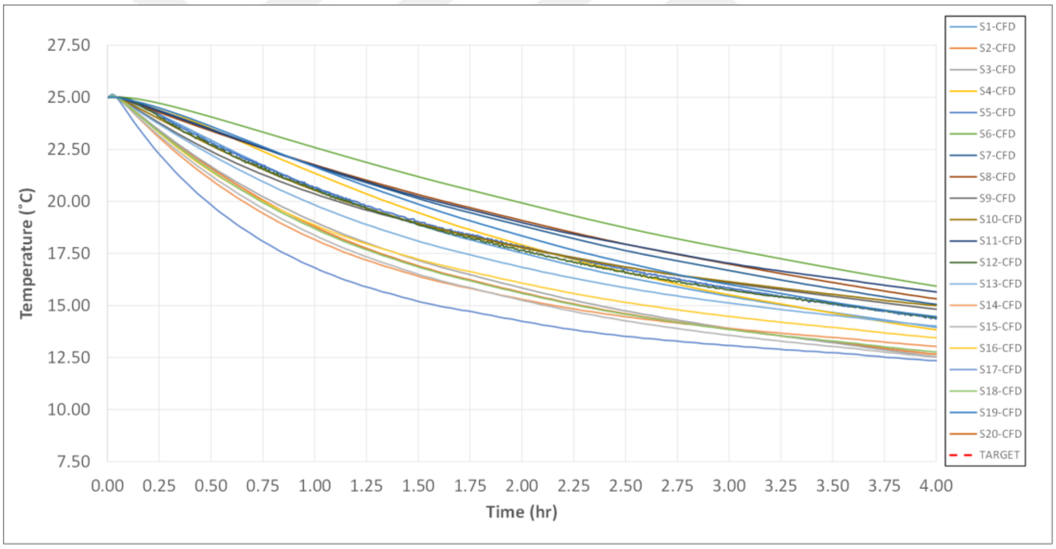

Figure D-8. Temperature variation for B-45-250 configuration

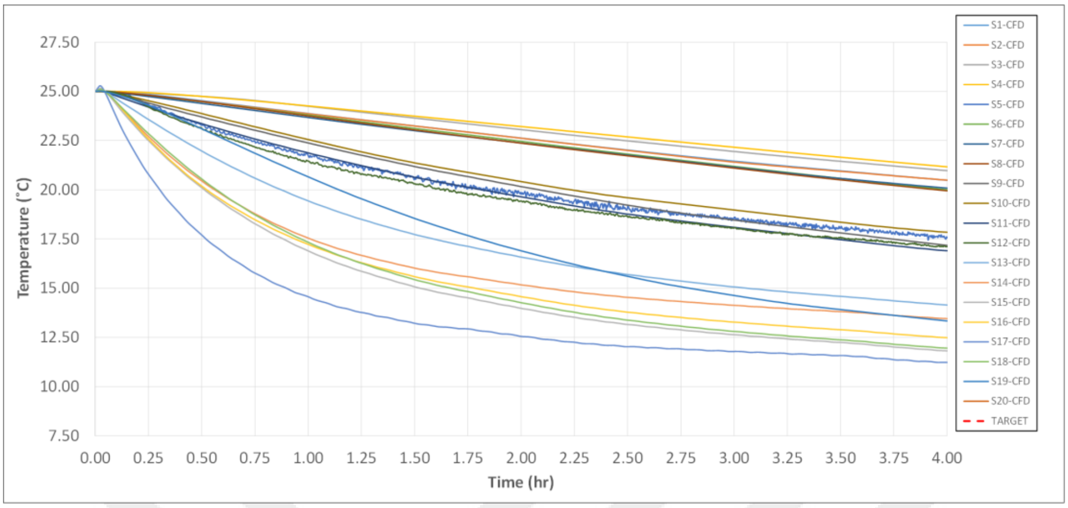

Figure D-9. Temperature variation for B-45-375 configuration